Oxide materials for hosting minor actinides: Investigation of phase relations and thermo-physical properties

By

CHIRANJIT NANDI

CHEM01201304018

Bhabha Atomic Research Centre, Mumbai

A thesis submitted to the
Board of Studies in Chemical Sciences

In partial fulfillment of requirements
for the Degree of

DOCTOR OF PHILOSOPHY

of

HOMI BHABHA NATIONAL INSTITUTE

July, 2018

Homi Bhabha National Institute[1]

Recommendations of the Viva Voce Committee

As members of the Viva Voce Committee, we certify that we have read the dissertation prepared by **Mr. Chiranjit Nandi** entitled **"Oxide materials for hosting minor actinides: Investigation of phase relations and thermo-physical properties"** and recommend that it may be accepted as fulfilling the thesis requirement for the award of Degree of Doctor of Philosophy.

Chairman : **Prof. S. Kannan** Date: 17.9.18

Guide / Convener: **Prof. A. K. Tyagi** AKTyagi Date: 17.09.2018

Co-guide - (if any) Date:

Examiner : **Prof. Nand Kishore** Date: 17.09.2018

Member : **Prof. S. K. Mukerjee** Date: 17/09/2018

Member : **Prof. S. C. Parida** Date: 17/9/18

Invitee : **Dr. Amrit Prakash** Amrit Prakash Date: 17.7.18

Final approval and acceptance of this thesis is contingent upon the candidate's submission of the final copies of the thesis to HBNI.

I/We hereby certify that I/we have read this thesis prepared under my/our direction and recommend that it may be accepted as fulfilling the thesis requirement.

Date: 17.09.2018

Place: BARC

AKTyagi
(Signature)
Guide

डॉ. ए. के. त्यागी/Dr. A. K. Tyagi
अध्यक्ष, नाभिकीय एवं ऊर्जा पदार्थ अनुभाग
Head, Nuclear & Energy Material Section
रसायनिकी प्रभाग/Chemistry Division
भा.प.अ.कें./B.A.R.C.
ट्रॉम्बे, मुंबई-४०००८५./Trombay, Mumbai-400085.

---

[1] This page is to be included only for final submission after successful completion of viva voce.

Version approved during the meeting of Standing Committee of Deans held during 29-30 Nov 2013

STATEMENT BY AUTHOR

This dissertation has been submitted in partial fulfillment of requirements for an advanced degree at Homi Bhabha National Institute (HBNI) and is deposited in the Library to be made available to borrowers under rules of the HBNI.

Brief quotations from this dissertation are allowable without special permission, provided that accurate acknowledgement of source is made. Requests for permission for extended quotation from or reproduction of this manuscript in whole or in part may be granted by the Competent Authority of HBNI when in his or her judgment the proposed use of the material is in the interests of scholarship. In all other instances, however, permission must be obtained from the author.

Chiranjit Nandi
20/07/2018

Chiranjit Nandi

DECLARATION

I, hereby declare that the investigation presented in the thesis has been carried out by me. The work is original and has not been submitted earlier as a whole or in part for a degree / diploma at this or any other Institution / University.

Chiranjit Nandi
20/07/2018

Chiranjit Nandi

List of Publications arising from the thesis

Journals

[1] Nd^{3+}-substituted $(Zr_{1-x}Ce_x)O_2$ $(0.0 \leq x \leq 1.0)$ system: Synthesis, structural and thermophysical investigations, **C. Nandi**, V. Grover, M. Sahu, K. Krishnan, A. Guleria, S. Kaity, A. Prakash, A.K. Tyagi, J. Nucl. Mater. **2016,** 479, 152-161.

[2] ZrO_2-$NdO_{1.5}$ system: Investigations of phase relation and thermophysical properties, **C. Nandi**, D. Jain, V. Grover, K. Krishnan, J. Banerjee, A. Prakash, K.B. Khan, A.K. Tyagi, Mater. Des. **2017**, 121, 101-108.

[3] Structural response of Nd-stabilized zirconia and its composite under extreme conditions of swift heavy ion irradiation, **C. Nandi**, V. Grover, P.K. Kulriya, A.K. Poswal, A. Prakash, K.B. Khan, D.K. Avasthi, A.K. Tyagi, J. Nucl. Mater. **2018**, 499, 216-224.

[4] Exploring YSZ/ZrO_2-PuO_2 systems: Candidates for inert matrix fuel, **C. Nandi**, V. Grover, K. Bhandari, S. Bhattacharya, S. Mishra, J. Banerjee, A. Prakash and A.K. Tyagi**,** J. Nucl. Mater. **2018**, 508, 82-91.

[5] $Zr_{0.70}[Y_{1-x}Nd_x]_{0.30}O_{1.85}$ as a potential candidate for inert matrix fuel: Structural and thermo-physical investigations, **C. Nandi**, D. Jain, V. Grover, R. Dawar, S. Kaity, A. Prakash, A.K. Tyagi, J. Nucl. Mater. **2018**, 510, 178-186.

Conferences

[1] YSZ-PuO_2 system: Inert matrix fuel candidate, **C. Nandi**, K. Bhandari, S. Bhattacharya, A. Prakash and V. Bhasin, Indian Analytical Science Congress 2018 (IASC-2018); Feb 08-10, 2018, Kerala, pp. 39-40.

[2] Synthesis and Characterisation of $Zr_{0.70}[Y_{1-x}Nd_x]_{0.30}O_{1.85}$ ($0.0 \leq x \leq 1.0$) Inert Matrix Fuel Materials, **C. Nandi**, S. Bhattacharya, M. Choudhary, A. Prakash, K.B. Khan, V. Bhasin, Nuclear and Radiochemistry Symposium (NUCAR-2017); Feb 06-10, 2017, Odisha, pp. 122-123.

Chiranjit Nandi
20/07/2018

Chiranjit Nandi

Dedicated to

my parents

(Shri Sailendra Nath Nandi & Smt. Rina Nandi)

&

my wife

(Smt. Shilpi Nandi)

ACKNOWLEDGEMENTS

First and foremost, I would like to thank my supervisor, **Prof. A.K. Tyagi**, for accepting me as his Ph.D. student. I wish to express my sincere gratitude towards him for his invaluable guidance, suggestions and continuous encouragement during the progress of my research work.

Further, I take immense pleasure in expressing my heartfelt gratitude to **Dr. Vinita Grover** for her valuable suggestions, guidance, direction and continuous assistance throughout the course of this work. She has motivated me constantly and specially at my hard time during this journey. She has taught me how to analyze the experimental data and to write a technical document out of it. I appreciate all her contributions for making my Ph.D. experience interesting.

I would also like to thank members of the doctoral committee: **Prof. S. Kannan**, **Dr. S.K. Mukerjee**, **Dr. S.C. Parida** and **Dr. Amrit Prakash** for spending their valuable time with me and offering their valuable suggestions and comments during the progress of my research work.

I sincerely acknowledge the contributions of my collaborators: **Mr. Dheeraj Jain**, **Mr. Santu Kaity** and **Dr. K. Krishnan** in this thesis.

I am thankful to **Dr. P.K. Kulriya** and **Dr. D.K. Avasthi** of IUAC, New Delhi for helping me in carrying out swift heavy ion irradiation studies.

I would like to thank **Dr. Rakesh Shukla**, **Dr. K. Bhattacharyya, Mr. Mohsin Jafar**, **Dr. S.N. Achary**, **Dr. B.P. Mandal**, **Dr. J. Banerjee**, **Mr. Sudhir Mishra**, **Dr. M. Roy**, **Dr. R. Phatak**, **Dr. Vats Bal Govind**, **Dr. F.N. Sayed**, **Dr. P. Anithakumari**, **Dr. M. Sahu**, **Dr. A. Guleria**, **Smt. Rimpi Dawar** and **Mrs. Aruna** for their help and cooperation.

I wish to extend my sincere thanks to **Mr. Arun Kumar** (Ex-Director, NFG), **Dr. K.B. Khan** (Ex-Head, RMD), **Mr. Vivek Bhasin** (Head, RMD & AD, NFG) and **Dr. K.I. Priyadarsini** (Head, ChD) for their help and encouragement.

I would also like to thank my friends **Giri**, **Ghoshal**, **Bhandari**, **Santosh**, **Akanksha**, **Somesh** and my all **colleagues of M-41, M-42 and M-28** laboratory for their help and support during the course of the research work.

At last but not the least, I thank my **parents**, **parents-in-law**, **uncle-aunty**, **brothers** and my all **relatives** for their encouragement. I am grateful to my wife **Shilpi** and my child **Sourish** for their consistent support throughout my research work.

Chiranjit Nandi
20/07/2018

Chiranjit Nandi

CONTENTS

SYNOPSIS

Nuclear power is being considered as an important source of energy because of its potential to offer a reliable energy source in a sustainable manner. The major concern in the way of large scale implementation of nuclear energy is nuclear waste which contributes to environmental burden and at the same time is an excellent source of unique wealth (radioisotopes for health care and agriculture related applications). Plutonium (Pu) and minor actinides (MAs), although present in nuclear waste at relatively low concentrations, are associated with long term radiotoxicity and are hazardous if released into the biosphere. Thus, conversion of these species into short-lived products may be the most effective solution to reduce the time scale of waste management from millions of years to several hundreds of years. This could be achieved by separating Pu and MAs from nuclear waste and fissioning/transmuting them in fission reactor and/or in accelerator driven sub critical systems (ADSS). The separation and incineration of Pu and MAs is known as partition and transmutation [1]. Several matrices (fissile, fertile and inert) have been investigated to act as host matrix for transmutation of Pu and MAs. To achieve high transmutation rate, it is required to eliminate further production of these nuclides in the host matrix during irradiation in the reactor. This could be accomplished by the substitution of conventional UO_2 matrix by a neutron transparent matrix. This is known as Inert Matrix Fuel (IMF) concept [2]. The inert matrix may be in the form of oxide, carbide, nitride or metallic. The present thesis investigates oxide-based materials for inert matrix fuel. Materials like Al_2O_3, MgO, CeO_2, $MgAl_2O_4$, $Y_3Al_5O_{12}$ and yttria stabilized zirconia (YSZ) are being investigated as oxide based host matrices for the incineration of Pu and MAs either in solid solution form or in dispersion form worldwide [3]. The literature survey indicates that YSZ and CeO_2 could be the better choice among the oxide based materials as host matrices for this purpose. On the contrary, pure zirconia has not been employed as matrix component for transmutation of Pu and MAs in literature. In the present investigation, ZrO_2 has been investigated as matrix component extensively. YSZ and CeO_2 have also been employed in some cases. The fissile phases are oxides of Pu and MAs which are highly radioactive and radiotoxic. Consequently, they are handled in glove boxes with special care. In order to carry out research in this area, it is very important to employ non-radioactive surrogates in place of these radioactive materials before carrying out actual experiment to avoid radiological hazards. Cerium oxide (CeO_2) is used as a surrogate material for plutonium oxide [4] while neodymium oxide (Nd_2O_3) has been widely employed as a non-radioactive surrogate for two minor actinides namely, americium (III) oxide (Am_2O_3) and curium (III) oxide (Cm_2O_3) for various studies [5]. The reason is attributed to their almost similar sizes and crystal structure which manifest in similar solid state chemistry.

In the present thesis, it is aimed to establish phase relations between matrix component and fissile phase. Information on phase relations would be useful to estimate Pu and MA loading capacity in the host matrix of interest. Thermo-physical properties like thermal expansion, heat capacity and thermal conductivity of selected compositions have also been measured. Accurate assessment of thermal expansion of nuclear materials is important to estimate the extent of swelling under thermal stress. Thermal conductivity is an important parameter to understand the performance of the fuels under irradiation. The lower thermal conductivity of fuel results in large temperature gradient in the radial direction of the fuel pellet and is the driving force for fuel restructuring. It also results in high centerline temperature of the fuel which control fission gas release. The thermal conductivity of nuclear fuel determines the linear power. Hence, determinations of these properties are essential requirements for fuel pin design and for predicting in-pile fuel performance. The systems which have been investigated in the present thesis for phase relation and thermo-physical properties as potential inert matrix system are (a) $Zr_{1-x}Nd_xO_{2-x/2}$ $(0.0 \leq x \leq 1.0)$,

(b) $Zr_{0.70}[Y_{1-x}Nd_x]_{0.30}O_{1.85}$ ($0.0 \le x \le 1.0$), (c) $Nd_{0.20}[Zr_{1-x}Ce_x]_{0.80}O_{1.90}$ ($0.0 \le x \le 1.0$) and (d) YSZ/ZrO_2-PuO_2. In addition to the above mentioned properties, the structural response of the material during irradiation by neutrons, fission fragments (FF), α-particles and α-recoils produced in the reactor environment is of paramount importance. As a part of this study, radiation stability of $Zr_{0.80}Nd_{0.20}O_{1.90}$, $Zr_{0.80}Nd_{0.20}O_{1.90}$–MgO (50 wt. %) composites and $Zr_{0.80}Nd_{0.10}Y_{0.10}O_{1.90}$ nominal compositions has been investigated using 120 MeV Au ions as swift heavy ions in order to investigate the effect of fission fragments. All these aspects are discussed in this thesis in eight chapters. The contents of each chapter are briefly described here.

Chapter 1: Introduction

Chapter 1 describes the need for deployment of nuclear energy and its importance to meet the growing energy demand. It has been stated that nuclear waste is the major challenges in the way of successful deployment of nuclear energy. As a solution to long term radiotoxicity of nuclear waste, concept of partition and transmutation has been introduced and explained. It is emphasized that Inert Matrix Fuel (IMF) concept should be invoked for the efficient transmutation of Pu and MAs. The reactor physics problem (reactivity issues) associated with these matrices is also discussed. Thermal reactors, fast reactors and ADSS are discussed in the context of transmutation of minor actinides. It has been emphasized that ADSS may be the best system for the transmutation of Pu and MAs. Different types of matrices as host for transmutation purpose have been described. The literature on IMF concept has been discussed. The neutron irradiation experiences of some oxide based inert matrix have been described. Finally, zirconia based matrices have been chosen as potential matrix component for the present study. The production of Pu and MAs in reactors is explained. Different oxides of plutonium and minor actinides and their crystal structure have been discussed. Use of surrogate materials for these highly radiotoxic plutonium and MA has been explained. The reasons for choosing CeO_2 as surrogate of PuO_2 and Nd_2O_3 as surrogate of minor actinides (Am_2O_3 and Cm_2O_3) is discussed. Lastly, research goals and objectives have been discussed.

Chapter 2: Experimental techniques

This chapter provides an overview of methods for synthesis of materials and the techniques employed for their characterization and thermo-physical property evaluation. The conventional solid state synthesis method and gel combustion method have been used for the preparation of the materials in this research work and discussed in this chapter. The materials synthesized have been thoroughly characterized by various techniques such as X-ray Diffraction (XRD), Raman Spectroscopy, Scanning Electron Microscopy (SEM) and Energy Dispersive Spectroscopy (EDS). The thermo-physical properties like lattice and bulk thermal expansion have been measured by employing high temperature X-ray Diffraction (HT-XRD) and Dilatometry, respectively. Heat capacity of few samples has been measured by Differential Scanning Calorimeter (DSC). Thermal conductivity of selected composition has been calculated from thermal diffusivity values which were obtained by Laser Flash Apparatus (LFA). The working principles of the various techniques along with brief description have been discussed in this chapter.

Chapter 3: Synthesis, characterization and thermo-physical properties in $Zr_{1-x}Nd_xO_{2-x/2}$ ($0.0 \leq x \leq 1.0$) system

ZrO_2-$NdO_{1.5}$ binary system as a potential inert matrix has been investigated. $NdO_{1.5}$ has been employed as surrogate for americium (III) oxide and curium (III) oxide and zirconia as the matrix component. Phase relations have been studied in ZrO_2-$NdO_{1.5}$ system using high temperature sintered samples prepared by gel combustion route. Phase characterization of $Zr_{1-x}Nd_xO_{2-x/2}$ ($0.0 \leq x \leq 1.0$) series has been carried out using XRD, Raman spectroscopy, SEM and EDS. It has been observed that with increasing $NdO_{1.5}$ content, the system evolves in a sequence of (a) monoclininc zirconia (b) mixture of monoclinic + cubic stabilized zirconia, (c) cubic stabilized zirconia (d) mixture of stabilized zirconia + pyrochlore (e) pyrochlore (f) mixture of pyrochlore + hexagonal Nd_2O_3 and (g) pure hexagonal Nd_2O_3. Around 20 mol% $NdO_{1.5}$ has been identified as minimum substitution required for stabilizing monoclinic zirconia in cubic phase. A maximum of 50 mol% $NdO_{1.5}$ could be incorporated in ZrO_2 maintaining single phase cubic structure. This information would be useful for incorporation of minor actinides in ZrO_2-based matrices to develop novel transmutation matrices. Lattice and bulk thermal expansion of few selected compositions have been determined using high temperature XRD (298-1273 K) as well as dilatomety (323-1673 K). It has been observed that successive introduction of $NdO_{1.5}$ in $Zr_{1-x}Nd_xO_{2-x/2}$ system (x = 0.2, 0.3, 0.4, 0.5) solid solutions decreases the thermal expansion coefficient. This has been attributed to increasing order in the cation sub-lattice resulting into overall increase in lattice stability. Thermal conductivity has been reported for a representative composition $Zr_{0.80}Nd_{0.20}O_{1.90.}$ Thermal conductivity (normalized to 100% dense sample) remains nearly constant (1.65-1.80 W/m-K) over the temperature range RT-1373 K. This value is found to be low as compared to typical oxide fuel such as UO_2.

Chapter 4: Investigation of phase relations and thermal properties in $Zr_{0.70}[Y_{1-x}Nd_x]_{0.30}O_{1.85}$ (0.0 ≤ x ≤ 1.0) system

Phase relations in ZrO_2-$NdO_{1.5}$ system as described in chapter 3 show that incorporation of 10 mol% $NdO_{1.5}$ in ZrO_2 leads to a biphasic mixture consisting of monoclinic zirconia (m-ZrO_2) and Nd-stabilized cubic zirconia. Thus, to investigate the expansion of single phasic phase-field, a neutron transparent trivalent cation (Y^{3+}) has been co-doped with Nd^{3+} in appropriate mole fractions and studied in this work. In this context, the system $Zr_{0.70}[Y_{1-x}Nd_x]_{0.30}O_{1.85}$ ($0.0 \leq x \leq 1.0$) has been investigated for phase relation and thermo-physical properties. All the compositions in this series were synthesized by solid state route and characterized by X-ray diffraction (XRD) and Raman spectroscopy. Interestingly, the entire system appeared single-phasic fluorite-type by XRD. However, Raman spectroscopy could reveal the existence of tetragonal domains for the Nd-rich composition, $Zr_{0.70}Nd_{0.30}O_{1.85}$ (x = 1.0). The study exemplifies the use of local structural techniques to reveal the structural changes in much shorter range as compared to diffraction techniques. Bulk thermal expansion coefficient has been found to increase with increasing $NdO_{1.5}$ content in this series in the temperature range 298–1473 K. The heat capacity of sintered samples has been measured by heat flux-type differential scanning calorimeter over the temperature range 313–713 K. Specific heat capacity of the solid solutions has been found to decrease with increasing Nd^{3+}- content. The thermal diffusivity values have been determined for the end members, yttria- and neodymia-stabilized zirconia. The thermal conductivity values have then been calculated from measured thermal diffusivity, temperature dependent density and specific heat capacity values. Thermal conductivity of Nd^{3+} stabilized zirconia has been found to be low as compared to that of Y^{3+} stabilized zirconia and this has been attributed to the large difference of mass and ionic size between Zr^{4+} and Nd^{3+} relative to Zr^{4+} and Y^{3+}.

Chapter 5: Studies in $Nd_{0.20}[Zr_{1-x}Ce_x]_{0.80}O_{1.90}$ $(0.0 \leq x \leq 1.0)$ system for hosting plutonium and minor actinides

The previous two chapters were concerned with variation of MA surrogate, whereas this chapter reports the variation of host lattice. In this chapter, $Nd_{0.20}[Zr_{1-x}Ce_x]_{0.80}O_{1.90}$ $(0.0 \leq x \leq 1.0)$ system has been investigated in terms of phase relation and thermo-physical properties as the representative candidate for transmutation of both plutonium (CeO_2 as surrogate of PuO_2) and MA (Nd_2O_3 as a MA surrogate). In addition, CeO_2 itself is also proposed as one of the candidate materials for inert matrices. The Nd^{3+} content has been fixed at 20 mol% with the dual objective. Approximately, 20 mol% minor actinides could be loaded in transmutation targets [6] and also, as obtained previously, minimum 20 mol% Nd^{3+}

is required to stabilize zirconia in cubic phase completely [7, 8]. The entire system has been synthesized by solid state route and thoroughly characterized by X-ray diffraction (XRD) and Raman spectroscopy. It has been observed that substitution of a trivalent ion like Nd^{3+} could stabilize the otherwise multi-phasic CeO_2-ZrO_2 system and the entire phase relation revealed to be single-phasic F-type throughout the composition range. However, Raman spectroscopy revealed difference in local structure of fluorite-type phases with variation in Ce^{4+}-content (or Zr^{4+}-content). They could be broadly classified as two kinds of fluorite-type lattices: cubic stabilized zirconia-type and cubic defect ceria-type. The heat capacity of representative compositions has been measured by heat flux-type differential scanning calorimeter in the temperature range of 300–870 K. Specific heat capacity of the solid solutions has been found to increase with decreasing CeO_2 content. HT-XRD has been employed to determine the lattice thermal expansion coefficients which have been observed to increase with increase in CeO_2 content in Nd^{3+}-stabilized cubic zirconia. The observed solubility of 20 mol% Nd^{3+} in CeO_2-ZrO_2 system adopting a single-phasic cubic structure is a significant result in the context of potential candidates for minor actinide transmutation and inert matrix fuel.

Chapter 6: Phase relation in YSZ/ZrO_2-PuO_2 system

Chapter 3-5 dealt with the loading of minor actinides (MA) and PuO_2 in zirconia based matrix and their thermo-physical properties using the non-radioactive surrogate materials Nd_2O_3 and CeO_2, respectively. In this chapter, radioactive PuO_2 material itself, instead of surrogate materials has been employed as the fissile phase in the investigation of phase relation and thermo-physical properties in YSZ–PuO_2 and ZrO_2–PuO_2 system. In addition, the results are also expected to validate the use of CeO_2 as the surrogate for PuO_2. In YSZ-PuO_2 system, $(YSZ)_{1-x}(PuO_2)_x$ ($0.0 \le x \le 0.5$) compositions have been prepared by solid state route under vacuum heating conditions and characterized by XRD. The fluorite structure has been exhibited for products with low PuO_2 content (up to 20 mol %) in this series while the pyrochlore structure has been observed for the samples with 30-50 mol% PuO_2 content. Annealing under oxidizing conditions do not alter the F-type phases but decreases the ordering in pyrochlore phases. The shrinkage studies on YSZ-PuO_2 samples indicate 1773 K may be good sintering temperature in YSZ-PuO_2 system. Linear thermal expansion on two compositions has been measured in a vertical dilatometer over the temperature range from RT to 1673 K in argon atmosphere. Though the coefficients of linear thermal expansion of 0.6YSZ-0.4PuO_2 (40 mol% PuO_2 containing YSZ) is low compared to that of YSZ ($x = 0.0$) at lower temperature it becomes higher beyond 1473 K. In ZrO_2-PuO_2 system, only two compositions $Zr_{0.8}Pu_{0.2}O_2$ and $Zr_{0.5}Pu_{0.5}O_2$ have been prepared by solid state route in Ar-8% H_2 atmosphere and characterized by XRD. The composition $Zr_{0.8}Pu_{0.2}O_{2-x}$ has been found to adopt fluorite type lattice while $Zr_{0.5}Pu_{0.5}O_{2-x}$ exists in pyrchlore structure. The F-type phase, upon oxidation, transforms to tetragonal phase while the pyrochlore phase retains its identity with concomitant decrease in intensity of superstructure reflections indicating the ensuing pyrochlore to fluorite phase transition. Phase behaviour of PuO_2 during heat treatment under different atmosphere has also been discussed in this chapter.

Chapter 7: Investigation of radiation tolerance of stabilized zirconia and its composite under swift heavy ion irradiation

The structural response during irradiation by fission fragments (FF) is a very important parameter of any inert matrix for its qualification as nuclear fuel. The effect of FF on the matrices can be simulated by irradiating them with swift heavy ions (SHI) with masses and energies similar to that of FF. This chapter describes the radiation response of $Zr_{0.80}Nd_{0.20}O_{1.90}$, $Zr_{0.80}Nd_{0.20}O_{1.90}$-MgO (50 wt %) composites and $Zr_{0.80}Nd_{0.10}Y_{0.10}O_{1.9}$ nominal compositions when irradiated with 120 MeV Au ions. The composition $Zr_{0.80}Nd_{0.20}O_{1.90}$ represents 20 mol% minor actinide (Nd_2O_3 as a MA surrogate) loaded zirconia. MgO was added to $Zr_{0.80}Nd_{0.20}O_{1.90}$ to form a composite to enhance the thermal conductivity because of superior thermal conductivity of MgO. $Zr_{0.80}Nd_{0.10}Y_{0.10}O_{1.90}$ represents 10 mol% minor actinide (Nd_2O_3 as a MA surrogate) and 10 mol% Y^{3+} co-doped ZrO_2. The compositions have been synthesized by gel combustion followed by high temperature sintering and characterized by XRD, SEM and EDS. All the compositions crystallize in FCC structure. Irradiation was carried out by 120 MeV Au ions at various fluences and irradiation induced structural changes have been probed by *in situ* X-ray diffraction (XRD). The XRD results confirm that the fluorite structure is retained under swift heavy ion irradiation for all the compositions explaining their exceptional radiation stability. The results indicated better irradiation behaviour of $Zr_{0.80}Nd_{0.20}O_{1.90}$ (defect fluorite structure) over $Zr_{0.5}Nd_{0.5}O_{1.75}$ (pyrochlore) thus showing that the radiation damage depends considerably on composition and structure. These results might have implications on the minor actinide loading in zirconia in context of their radiation tolerance. Formation of a ceramic-ceramic (CERCER) composite of MgO with Nd-stabilised zirconia further enhanced the radiation tolerance behaviour of $Zr_{0.80}Nd_{0.20}O_{1.90}$ against swift heavy ion irradiation. The substitution of 10 mol% Y in the composition $Zr_{0.80}Nd_{0.20}O_{1.90}$ to get $Zr_{0.80}Nd_{0.10}Y_{0.10}O_{1.90}$ increases the covalent character and thus led to decrease in radiation stability of the lattice. Investigation of these compositions by XANES spectroscopy, before and after irradiation, however, did not show any change in local electronic structure of constituent ions.

Chapter 8: Summary and future scope

This chapter provides a summary of the work carried out during the course of this thesis. It also compares and correlates the results obtained from different studies to develop novel transmutation targets. Particularly, the phase relation studies demonstrate the structural feasibility of loading minor actinides in zirconia-based targets. However, investigation of thermo-physical properties indicated the need for enhancement in thermal conductivity of these matrices for this particular application. Synthesis viability with minor actinides has been demonstrated using radioactive PuO_2 material. Swift heavy ion irradiation results of few representative compositions indicate excellent radiation stability which would be significant in terms of their application as transmutation target.

The future scope of this work has been discussed in this chapter. It involves improvement in matrix design to have reasonably high thermal conductivity. Also, investigation in phase relation and thermo-physical properties in ZrO_2-$AmO_{1.5}$ may be carried out.

References:

[1] A. Stanculescu, Ann. Nucl. Energy 62 (2013) 607-612.

[2] C. Degueldre, J. Paratte, J. Nucl. Mater. 274 (1999) 1-6.

[3] H. Kleykamp, J. Nucl. Mater. 275 (1999) 1-11.

[4] A.K. Tyagi, B. Ambekar, M. Mathews, J. Alloys Compd. 337 (2002) 277-281.

[5] H. Williams, H. Ning, M. Reece, R. Ambrosi, N. Bannister, K. Stephenson, J. Nucl. Mater. 433 (2013) 116-123.

[6] M. Osaka, H. Serizawa, M. Kato, K. Nakajima, Y. Tachi, R. Kitamura, S. Miwa, T. Iwai, K. Tanaka, M. Inoue, J. Nucl. Sci. Technol. 44 (2007) 309-316.

[7] C. Nandi, D. Jain, V. Grover, K. Krishnan, J. Banerjee, A. Prakash, K. Khan, A. Tyagi, Mater. Des. 121 (2017) 101-108.

[8] Z.-G. Liu, J.-H. Ouyang, B.-H. Wang, Y. Zhou, J. Li, J. Alloys Compd. 466 (2008) 39-44.

LIST OF FIGURES

LIST OF TABLES

CHAPTER 1

Introduction

1.1. Nuclear energy

Energy is the crucial component to improve the living standards in the modern society. It is also required for the industrial and economic growth of any country. At present, a major fraction of energy is obtained from the fossil fuels (coal, oil and gas). Though there is a good reserve of the fossil fuels but it is bound to exhaust with time. It pollutes the atmosphere significantly and also contributes to the greenhouse effect and acid rain. Thus, with the aim of conserving our limited natural resources for the future generation, to limit the climate change and to switch over from carbon based fuel to carbon free fuel, renewable energies like hydro, wind and solar energies may be the alternative energy sources [1]. However, with present infrastructure of renewable energies, it will not be possible to replace coal by renewable energies satisfying the needs of our industrial civilization and the aspirations of the developing nations [2, 3]. Consequently, nuclear energy was deployed to address this situation in India and abroad considering its huge potential [3]. Today, nuclear energy provides a significant contribution towards the total electricity generation in the world. Approximately, 11% of the world’s total electricity is from nuclear power plants [4]. France is generating 72% of its total electricity from nuclear power plants [4]. Thirteen countries in the world are dependent on nuclear energy to supply at least 25% of their total electricity [4]. However, India is generating ~ 2% of the total electricity from nuclear power plants [5]. Nuclear energy is clean, safe, reliable, competitive and practically inexhaustible [3, 6]. The basic raw materials for nuclear energy are uranium and thorium which are found in the earth’s crust. The total conventional resource of uranium (15.9 million tons) is large enough to fuel the existing 449 reactors in the world for more than 450 years on once through basis [7]. The implementation of fast reactor with close fuel cycle and recycling options may increase the uranium utilization by a factor of 60 [7] and consequently may provide electricity for few thousands of years with this uranium reserve. The other raw material, thorium is more abundant than uranium [8]. In the context of Indian nuclear power program, thorium is more important for its large deposits and limited uranium reserves in India [9]. Hence, as a matter of fact, nuclear energy has a potential to offer a reliable source of energy in a sustainable manner. However, the nuclear energy is associated with a well-known paradox [10]. According to Cottrell et al. [10], the development and exploitation of nuclear energy has the potential both to enhance and endanger national and global security. The nuclear power may be an important source of energy as well as it may lead to increased possibility of misuse. Nuclear energy may be a green solution to climate change but at the same time the nuclear waste contributes to environmental burden. Therefore, there is a basic need to resolve the major issue of nuclear waste.

1.2. Nuclear waste and radiotoxicity

The fuel for the major commercial nuclear power reactors operated all over the world is either natural UO_2 or enriched UO_2. In both cases, the fissile species ^{235}U (^{235}U is 0.7% in natural UO_2 and 2-5% in enriched UO_2) contains majority of fertile isotope ^{238}U which produces ^{239}Pu in reactor absorbing a neutron followed by two β decay. The minor actinides (americium and curium) are produced in the reactor following the successive neutron captures by plutonium isotopes followed by beta decay. Production of isotopes of plutonium and minor actinides (MAs) has been pictorially presented in Fig. 1.1 [11]. Thus, the irradiated fuel which is generally termed as spent nuclear fuel contains (1) uranium, (2) plutonium, (3) fission products resulting from fission and (4) minor actinides. The spent fuel from commercial light water reactor (LWR) is composed of 98.5 wt% uranium and short lived fission products, 0.4 wt% long lived fission products (cesium, strontium, technetium, and iodine), 1 wt% plutonium and minor actinide isotopes [12].

These spent fuels after removal from reactor are either sent for reprocessing (closed fuel cycle option) or else transferred to long term wet or dry storage facility until geological repositories become available (once-through fuel cycle option). As per IAEA report [12], spent fuel contains approximately 110 tons of minor actinides while an additional 40 tons are contained in high level waste from reprocessing facility worldwide as of the year 2006. The quantity may be doubled by the year 2020. Plutonium, minor actinides and long lived fission products (iodine and technetium) although present in the spent fuel at relatively low concentrations are very long-lived and associated with long term radiotoxicity, heat load issues, proliferation risk and are hazardous to life when released into the environment. Some general features of the radiotoxicity of spent fuel (LWR fuel at a burn up of 33 GWd/tHM) are shown in Fig. 1.2 [13, 14]. The radiotoxicity curves for the components of spent fuel are also shown in the figure, in which the cross-over point indicates the time at which the radiotoxicity of the waste reaches the reference level. The reference radiotoxicity level is contributed by uranium ore and its daughter products. The radiotoxicity of the fission products reaches the reference level after about 300 years. The long-term radiotoxicity of this waste is mainly contributed by plutonium and minor actinides. This figure also shows that the spent fuel directly discharged from reactor will take 1,30,000 years before the radiotoxicity reaches the reference level. Therefore, their disposal requires isolation in suitable geological repositories which would guarantee the retention of radioactive materials for more than 1,30,000 years. Moreover, the enormous energy content of the actinides remains unutilized. However, in closed fuel cycle mode, the spent fuel discharged from the reactor is reprocessed and the products are partitioned into uranium (U) and plutonium (Pu). The separated plutonium can be used for the fabrication of mixed oxide fuel for light water reactors as well as fast reactors. The rest of the spent fuel which mainly consists of radioactive fission products and transuranic isotopes (Np, Am, Cm) is designated as high-level waste (HLW).

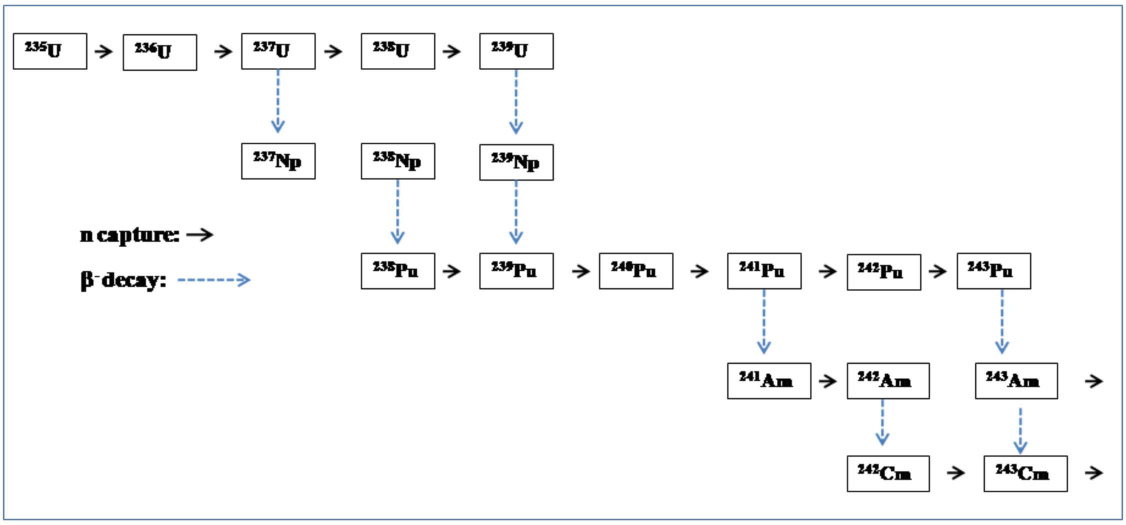

Fig. 1.1: Schematic of transmutation chain for production of plutonium and minor actinides [11]

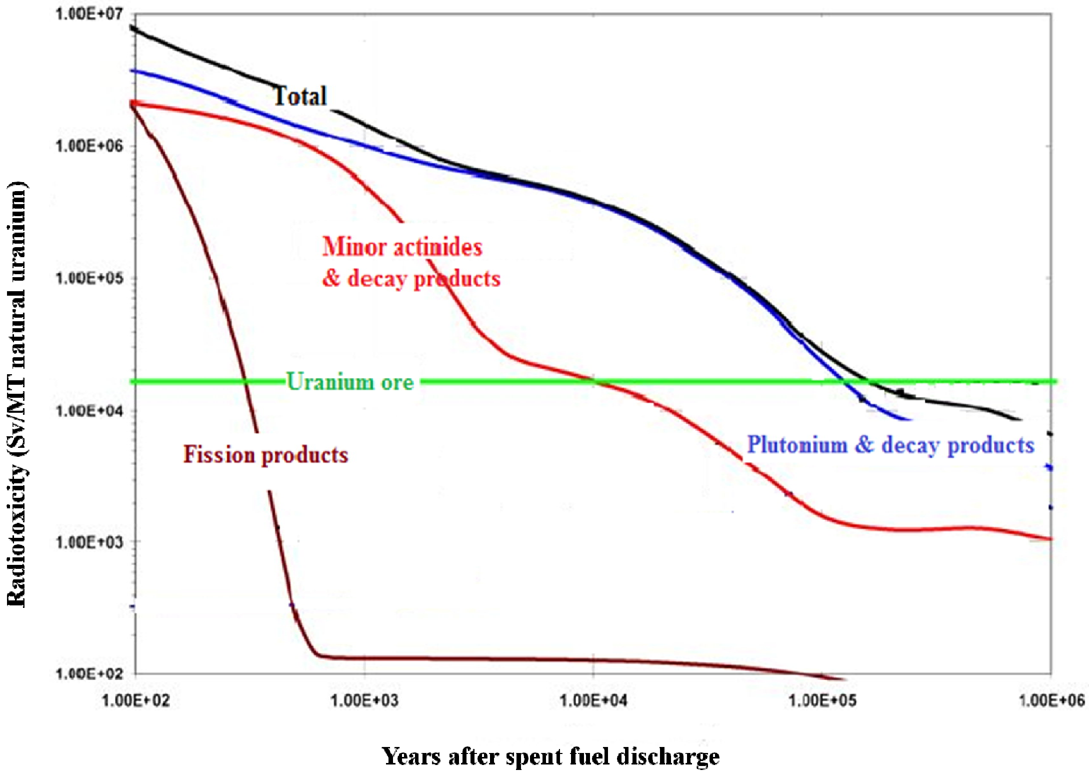

Fig. 1.2: Radiotoxicity of the different components of spent nuclear fuel (adopted from ref [14])

Though, the radiotoxicity of the fission products will reach the reference level after about 300 years still the HLW will require isolation of 10,000 years in the vitrified form as it contains minor actinides.

1.3. Partition and transmutation

The separation and incineration of plutonium and minor actinides (MAs) from spent fuel will reduce the radiotoxicity of the high level wastes significantly. Also, the time scale of waste management will be reduced from several thousands of years to a few hundreds of years. The process of the separation and incineration of these Pu and MA is known as partition and transmutation [15-20]. Both aqueous and non-aqueous partitioning techniques have been used on industrial scale and laboratory scale for separation of minor actinides and fission products. On the other hand, transmutation is defined as change of one nuclide into another as a result of nuclear reaction aiming to produce shorter-lived or more stable nuclides. Successful implementation of this scheme will lead to significant reduction of the inventory of plutonium and minor actinides with simultaneous reduction of the time scale of waste management. Separation of major constituent (uranium) will decrease the spent fuel volume thereby enabling more efficient and compact storage of nuclear waste. In other words, it would result in an increase of the effective capacity of final repository. Separation and removal of Cs and Sr will reduce heat issues of the repository [21]. Some of the fission products can be used effectively as resources for many applications.

1.4. Reactor systems for transmutation

As discussed earlier, in radioactive waste management, the objective of transmutation is to produce shorter-lived or more stable nuclides from long lived radioactive isotopes by means of nuclear reaction. This process may be achieved by fission reaction or by neutron capture reaction. In case of a fission reaction, the nucleus is transformed mainly into short-lived fission products (< 50 years). In case of capture reaction, the nucleus is transformed into another radionuclide which does not result significant reduction of radiotoxicity. Thus, for efficient transmutation, fission reactions are of course a better option over capture reactions [15]. The main nuclides of interest for transmutation are Pu and minor actinides (Am, Np, Cm) which can be most effectively transmuted by nuclear fission. In a nuclear reactor, the fission to capture cross section is more for the minor actinides in the fast spectrum of neutrons compared to thermal spectrum [22]. Also, all isotopes become fissionable in fast neutron spectrum. Moreover, both the neutron production and neutron flux is more in the fast spectrum. These two factors make the fast reactor a better candidate over thermal reactor for transmutation of minor actinides [15, 22, 23]. There are two concepts for transmutation of MA in fast reactor viz. homogeneous and heterogeneous recycling [15]. In case of homogeneous recycling, the MA is generally homogeneously mixed with the standard fast reactor fuel. However, introduction of minor actinides in the fuel may pose serious safety problems due to very small fraction of delayed neutrons generation per fission of MA [15, 24]. Moreover, presence of MAs decrease the fuel temperature coefficients (Doppler effect) and increase coolant void reactivity effect [15, 24]. Consequently, in order to reduce the harmful effects of MAs on the core physics (reactivity coefficient), the content of MAs in the fuel generally remain relatively low (typically < 2–5% of heavy atoms depending on the size of the core). In heterogeneous recycling mode, MA is separated from uranium and plutonium and is concentrated in special fuel pins known as targets, if the support of MAs is an inert matrix (neutron transparent). These targets are preferably located at the periphery of reactor to limit the neutron impact on the core physics. It must be noted that the fast spectrum can be provided by the sodium-cooled or gas-cooled fast reactors (respectively SFRs and GFRs) as well as the subcritical reactors driven by an accelerator (ADSS: accelerator-driven subcritical system) cooled with lead or lead-bismuth. The ADS system needs an external source of neutrons to sustain the chain reaction. These neutrons are provided by spallation reaction of high Z target (Pb, Bi) with high energy protons produced by the accelerator. Such a sub-critical system is easier to control compared to the conventional critical reactor. Therefore, Accelerator-Driven Subcritical System (ADSS) which is basically a subcritical fast neutron system may be the most promising alternative for the transmutation of MAs [15, 22].

1.5. The Inert Matrix Fuel (IMF) concept

From the above discussion, it is clear that there is a basic need to minimize the volume, quantity and radiotoxicity of minor actinides in an efficient manner. To achieve this, it is required to eliminate the source of production of these nuclides in the host matrix during irradiation in the reactor. This has been done by the substitution of UO_2 by a neutron transparent matrix. This is known as inert matrix fuel (IMF) concept [25-28]. In these fuels, an inert matrix serves as a support for the actinide phases either in solid solution or composite form. The inert matrix does not lead to the formation of any fissile material after irradiation. Several national and international research organizations have been pursuing R & D work aiming to eliminate the current stockpile of plutonium and minor actinides in thermal reactors and advanced systems. There are two different approaches that are being followed in this context [29]. The first option is deep incineration of plutonium and minor actinides using a once through fuel cycle approach followed by geological disposal. The second option is based on using a uranium free fuel amenable for reprocessing following a multi-recycling strategy. In both the cases, energy is produced during consumption of plutonium or minor actinides. In once through cycle, the transmutation efficiency must be maximized (> 90%).

1.6. Literature survey and materials selection

In order to select suitable inert matrix component for the hosting of minor actinides, the following factors are generally considered:

1. The matrix material should be transparent to neutrons which means that the neutron capture cross section of the material must be as small as possible. It results in low

neutron activation product thereby saving as many neutrons as possible. These neutrons are made available for fission of minor actinides.

2. It should be compatible with coolant and structural materials.
3. The material should have high melting point and phase transition should not occur in the operating temperature range of the fuel.
4. It should have good thermal conductivity which will ensure lower thermal gradient in the fuel. Therefore, there will be less restructuring of the fuel matrix. High thermal conductivity will also lead to high linear heat rating.
5. It should have good radiation stability. It should be stable under four irradiation damage sources viz. thermal or fast neutrons, α decay (5–6 MeV He ions, 100 KeV daughter recoil atoms), fission fragment impact (70–100 MeV heavy ions of elements between Ga and Dy) and intense β, γ radiation.
6. The matrix must meet acceptance criteria for direct disposal in case of once through cycle or reprocessing in case of multiple recycling.

A list of candidate materials that could act as the inert matrix for the burning of MA in the nuclear reactors is given in Table 1.1 [28, 30]. The inert matrix may be in the form of oxide, carbide, nitride or metallic. Carbides and nitrides matrices may be preferred candidate for fast reactors because of their better thermal conductivity and compatibility with sodium coolant. However, they are not considered for water cooled reactor because of their chemical reaction with water. The oxide based inert matrix fuel has been investigated extensively because of the wide international experience of oxide fuel fabrication and their use in the present nuclear reactors. Moreover, oxide compounds are chemically more stable and also satisfy the criteria for long term storage (adequate immobilization of radioactivity in geological disposal) particularly in case of once-through irradiation prior to geological disposal.

For inert matrix fuels, two configurations are generally considered: (a) a solid solution of the inert matrix material and the fissile material (b) a dispersion-type composite of fissile particles in an inert matrix phase. The composite may be of the following types:

1. CERCER (ceramic-ceramic): It is one kind of dispersion fuel where the fissile in form of ceramic is dispersed in a ceramic host matrix. The dispersion may be either macro or micro depending on the size of fissile phase.
2. CERMET (ceramic-metal): The ceramic fuel particles are dispersed in the metallic matrix.
3. METMET (metal-metal): The metal particles are dispersed in the metallic matrix in this type of fuel.

Materials like Al_2O_3, MgO, ZrO_2, CeO_2, $MgAl_2O_4$, $Y_3Al_5O_{12}$ and stabilized zirconia are being investigated as oxide based host matrices for the incineration of MA either in solid solution form or in dispersion form.

Table 1.1: Examples of probable inert matrix candidates [28, 30]

Inert matrix components	**Inert matrix formula**
Elements	C, Mg, Al, Si, Cr,V, Zr, Nb, Mo, W
Carbides	SiC, TiC, ZrC
Nitrides	AlN, TiN, ZrN,
Binary oxides	MgO, ZrO_2, CeO_2
Ternary oxides	$MgAl_2O_4$, $Y_3Al_5O_{12}$
Oxide solid solutions	$Ca_xZr_{1-x}O_{2-x}$, $Y_yZr_{1-y}O_{2-y/2}$

1.7. Irradiation experience of oxide inert matrix

The following section presents a brief overview of the applicability of the oxide materials listed here as suitable inert matrix and their irradiation experience.

$Y_3Al_5O_{12}$ as inert matrix

Yttrium aluminium garnet ($Y_3Al_5O_{12}$ or YAG) was selected as an inert matrix component in EFTTRA (Experimental Feasibility of Targets for Transmutation) programme for the development of targets for transmutation. Polycrystalline pellets of YAG were irradiated by neutron in the high flux reactor (HFR) at Petten to a neutron fluence of 1.7 x 10^{26} n/m^2 (E > 0.1 MeV) [31, 32]. The post irradiation examination of irradiated YAG showed good neutron irradiation stability and high dimensional stability (< 1 vol. %) of the matrix. The experiment pointed towards its suitability as inert matrix candidate for actinide transmutation. However, UO_2 dispersed in YAG when tested as inert matrix fuel in the EFTTRA-T3 experiment, a large diametrical swelling along with pellet fracturing was observed after irradiation for 198.87 full power days in the HFR, Petten [33, 34]. The experiment demonstrated that YAG may be less suitable for its use as an inert matrix candidate. This is in contrary to the results obtained with YAG matrix without fissile phase (UO_2), which showed good dimensional stability and was resistant to neutron irradiation as indicated above.

Al_2O_3 as inert matrix

Al_2O_3 was tested as inert matrix component in the EFTTRA experiment [31, 32] as well as MATINA and SANTENAY experiment [35]. A relatively large volume change of 4.2% and a high density of dislocation loops in the grains of Al_2O_3 pellets was observed after irradiation at neutron fluences of 0.46 x 10^{26} and 1.7 x 10^{26} n/m^2 [31, 32]. A large swelling of 28% was observed for Al_2O_3 for a fast neutron fluence of 1.7 x 10^{26} n/m^2 in SANTENAY experiment. In MATINA experiment, Al_2O_3 showed volume swelling of the order of 4% at fast neutron fluence (E > 0.1 MeV) of 1.95 x 10^{26} n/m^2 [35]. These experimental evidences explain poor interest in Al_2O_3 as transmutation matrix at least in fast neutron spectrum.

CeO_2 as inert matrix

CeO_2 was tested as an inert matrix component in EFTTRA experiment [31]. CeO_2 showed good dimensional stability during neutron irradiation. However, interaction of CeO_2 with the stainless steel cladding was observed in this experiment. Later on, CeO_2 containing UO_2 was used as inert matrix component in the EFTTRA-T3 experiment [33, 34]. A swelling of less than 1 vol. % and a fission-gas release of less than 10% were observed for UO_2 containing CeO_2 matrix upon irradiation. The overall irradiation behaviour was found to be quite good and it was suggested that the matrix might be suitable for transmutation purposes.

$MgAl_2O_4$ as inert matrix

Spinel ($MgAl_2O_4$) has been considered as transmutation matrix in EFTTRA experiment [31, 32] because of its high thermal conductivity, small neutron capture cross section (< 2.7 barn) and high melting point (2408 K) [36]. The post irradiation examination of neutron irradiated spinel showed good neutron irradiation stability and high dimensional stability (< 1 vol. %). The superior behaviour of spinel under neutron irradiation identified it as a promising inert matrix candidate. Consequently, like CeO_2 and $Y_3Al_5O_{12}$, $MgAl_2O_4$–UO_2 composite was tested as inert matrix component in the EFTTRA-T3 experiment [33, 34]. The irradiation behaviour was not much satisfactory because of the high fission-gas release, pellet fracturing and axial swelling. A chemical interaction layer between the matrix and the fissile phase was observed in the composite of $MgAl_2O_4$–UO_2. The composites of $MgAl_2O_4$ and UO_2 in macro and micro dispersed form were tested in THERMHET (thermal behaviour of heterogeneous fuel) irradiation in the SILOE reactor [37]. The micro dispersed composite showed amorphization and a major swelling in the fuel. $MgAl_2O_4$ was selected as inert matrix target for the transmutation of ^{241}Am in EFTTRA-T4 experiment [38]. The inert matrix itself showed poor behaviour under irradiation like large swelling. It also underwent severe structural modifications such as amorphization due to the radiation damage from the fission products and alpha-decay. This quite unsatisfactory behaviour had not been observed in the case of macro dispersed composite. Thus, it was suggested that $MgAl_2O_4$ could be used as transmutation target only in the case of macro dispersed composite fuel concept. However, $MgAl_2O_4$ was found to behave satisfactorily under fast neutron fluence ($E > 0.1$ MeV) in the MATrices for INcineration of Actinides (MATINA) experiment [35].

MgO as inert matrix

The low neutron absorption cross section, easy manufacturability, chemical stability, high melting point, high thermal conductivity and high radiation tolerance of MgO justify its use as inert matrix in many irradiation programs [35, 39]. It was irradiated in MATINA experiment [35]. The irradiation behaviour was satisfactory both for MgO and MgO-UO_2 composite. It was chosen as inert matrix component in the EFTTRA-T3 experiment [33]. The irradiation behaviour was quite good. These studies pointed that magnesium oxide could be used as an inert matrix for nuclear applications. The main advantage of MgO is its superior thermal conductivity and hence it can be used as a second phase to improve the thermal conductivity of the composite. This concept was exploited in the case of MgO and $Nd_2Zr_2O_7$ pyrochlore as a dual phase inert matrix fuel [40]. MgO is hydrolyzed to magnesium hydroxide in presence of water. Hence MgO alone cannot be used in water cooled reactor. To improve the corrosion resistance of the magnesium oxide a highly durable secondary phase such as zirconia has been used to retard the dissolution of the magnesia phase [41]. However, MgO is compatible with liquid sodium making it possible its use in fast reactors.

Zirconia based materials as inert matrix

Zirconia based materials like cubic stabilized zirconia is one of the most widely studied candidate inert matrix materials. Yttria stabilized zirconia (YSZ) has good chemical stability, low neutron absorption cross section, high melting point (~ 3000 K), good compatibility with the cladding and low solubility even in hot water [42]. YSZ also behaves like other fluorite type structures (e.g., CeO_2, ThO_2 and UO_2). ZrO_2 in either the pure monoclinic form or the stabilized cubic form is highly resistant to amorphization by neutrons [43] or fission tracks [44]. Yttria stabilized zirconia (YSZ) matrix is three times less soluble in water than UO_2 fuel under reducing conditions and about six times less under oxidizing conditions [45]. It is about 10^9 times less soluble than glass [45]. This low solubility makes the zirconia material very attractive candidate for deep geological disposal. The disadvantage of YSZ is its low thermal conductivity. The low thermal conductivity has a negative impact on the in-reactor performance of the material. It causes high centerline temperature, large temperature gradients, thermal stresses and high fission gas release, etc. [46]. The problem of low thermal conductivity can be circumvented by optimum addition of a secondary phase with higher thermal conductivity. Magnesium oxide and $MgAl_2O_4$ have been proposed as a secondary phase to improve thermal conductivity. On the other hand, pure zirconia exists in three polymorphs namely, monoclinic ($P2_1/c$ space group), tetragonal ($P4_2/nmc$ space group) and cubic (Fm-3m space group) [47]. At atmospheric pressure, monoclinic ZrO_2 (ambient temperature phase) transforms to tetragonal phase (t-ZrO_2) around 1443 K, which finally converts to cubic phase (c-ZrO_2) around 2643 K. Both high temperature polymorphs can however be stabilized at room temperature by incorporation of suitable dopants like Y^{3+} [48, 49]. Burnup calculations with zirconia as the inert matrix showed that more than 95% of the ^{239}Pu and more than 77% of the total plutonium could be burnt in zirconia matrix [36]. In addition to plutonium, americium and neptunium could also be fissioned to reduce their quantities by 75% and 85%, respectively [36]. The idea of burning minor actinides in addition to plutonium by a zirconia inert matrix fuel has also been investigated by other researchers and it was shown as a promising solution on a longer time scale [36]. Plutonia admixed with yttria stabilized zirconia (YSZ) in the form of solid solution and Pu containing YSZ–$MgAl_2O_4$ composite were tested in the frame of the 'once-through-then-out' (OTTO) irradiations program carried out by JAERI, PSI and NRG in the high flux reactor (HFR) in Petten, Netherlands [50]. The total plutonium depletion was approximately 35% for a burnup of 200 GWd/m^3. The axial swelling was almost 2%. The fission gas release was around 10%. Overall, the fuel performance was reported to be satisfactory. In case of YSZ–$MgAl_2O_4$ composite, the fission gas release was still low because of lower centerline temperature of the composite due to better thermal conductivity of $MgAl_2O_4$. The irradiation experiment IFA-651 with IMF based on yttria stabilised zirconia was carried out at OECD Halden Material Test Reactor to determine the general thermal behaviour of YSZ-based IMF under irradiation conditions similar to those in current light water reactors [51]. The centerline temperature was higher due to lower thermal conductivity of YSZ. However, it was in the expected range. The higher fuel temperature caused higher fission gas release. Thus, a solid solution of fissile phase (PuO_2 and oxides of MA) and YSZ dispersed in a second phase of higher thermal conductivity (MgO or spinel) will be the most appropriate configuration for an inert matrix fuel. In fact, this concept was used in the CAMIX–COCHIX experiment. A homogeneous target (solid solution) of americium oxide in yttria-stabilized $(Am,Y,Zr)O_{2-x}$ and two composite targets of $(Am,Y,Zr)O_{2-x}$ particles in MgO (micro and macro-dispersed) were selected for irradiation in PHENIX reactor [52].

1.8. Plutonium, minor actinides and their surrogates

The following section presents a brief description of plutonium and minor actinides. Production of these Pu and MAs in the reactor has already been discussed.

Several oxides of plutonium are found to exist in plutonium-oxygen phase diagram [53-56]. Plutonium dioxide (PuO_2) which is the highest oxide in the system exists in face-centered cubic type lattice while plutonium sesquioxide (Pu_2O_3) is found to exist with hexagonal crystal structure. Two intermediate oxide phases, $PuO_{1.52}$ (bcc phase) with a composition very close to sesquioxide (Pu_2O_3) phase and $PuO_{1.61}$ (bcc) which is stable only above 600 K, are found to exist in the phase diagram . The hexagonal Pu_2O_3 and bcc $PuO_{1.52}$ exists with a small composition range while PuO_2 with fluorite type structure can exist with oxygen vacancies down to $PuO_{1.61}$ at elevated temperature. However, bcc $PuO_{1.61}$ exists with the composition range from $PuO_{1.61}$ to $PuO_{1.71.}$

Few oxides of americium are found to exist in americium-oxygen phase diagram [57-59]. These are one dioxide (AmO_2), one intermediate cubic phase, and three sesquioxides (hexagonal-Am_2O_3, monoclinic-Am_2O_3 and cubic-Am_2O_3). Both stoichiometric AmO_2 and substoichiometric americium oxides with compositions AmO_{2-x} ($0 \leq x \leq 0.34$) exist in fluorite type cubic structure. Sesquioxide (Am_2O_3) exists in C-type cubic structure whereas monoclinic and hexagonal phases are the high temperature phase of americium sesquioxide. AmO_2 is known to be thermally less stable than PuO_2 and it begins to lose oxygen at temperature as low as 1175 K and eventually its sesquioxide Am_2O_3 is formed at elevated temperature (1475 K).

The data on phase diagram of Cm-O system is very limited [60-62]. The highest oxide of curium is curium dioxide (CmO_2) which has fluorite type structure at room temperature. CmO_2 is stable up to 653 K. Above this temperature it decomposes via two intermediate compositions to sesquioxide (Cm_2O_3) phase. The sesquioxide exists in c-type bcc structure which upon heating in the range 1073 to 1573 K transforms to monoclinic Cm_2O_3 which in turn transforms to hexagonal Cm_2O_3 at 1873 K.

Table 1.2: Comparison of few important properties of PuO_2 and CeO_2 [63, 64]

Property	**CeO_2**	**PuO_2**
Ionic size (Å)	$Ce^{4+}{}_6 = 0.87$ $Ce^{4+}{}_8 = 0.97$	$Pu^{4+}{}_6 = 0.86$ $Pu^{4+}{}_8 = 0.96$
Structure	Fluorite	Fluorite
Melting point (K)	2673	3017
Density (g/cc)	7.30	11.44
α x 10^6 (K^{-1})	11.83	11.61

Table 1.3: Comparison of few important properties of Am_2O_3, Cm_2O_3 and Nd_2O_3 [60, 64, 69, 70]

Property	**Am_2O_3**	**Cm_2O_3**	**Nd_2O_3**
Structure	Cubic (C type) Monoclinic (B type) Hexagonal (A type)	Cubic (C type) Monoclinic (B type) Hexagonal (A type)	Cubic (C type) Hexagonal (A type)
Ionic size (Å)	$Am^{3+}_6 = 0.975$ $Am^{3+}_8 = 1.09$	$Cm^{3+}_6 = 0.97$	$Nd^{3+}_6 = 0.983$ $Nd^{3+}_8 = 1.109$
Phase transition temperature (K)	C to B: 733-923 B to A: 1073-1173	C to B: 1073-1573 B to A: 1873	A to C: 873-1123
Melting point (K)	2475	2538	2545

Plutonium and minor actinides are highly radioactive and radiotoxic. Hence they are to be handled in glove boxes with special care. In order to carry out research in this area, it is very common to employ non-radioactive surrogates in place of these radioactive materials before carrying out the actual experiment to avoid radiological issues. Surrogate materials enable to carry out many studies for better understanding which is not possible with radioactive materials because of limited infrastructure. Cerium oxide (CeO_2) is used as a surrogate material for plutonium oxide because both of these possess similar physical properties like structures, ionic radii for Ce^{4+} and Pu^{4+}, melting points, thermal expansion etc. [63, 64]. The structural properties (e.g. solid solution formation) are greatly governed by their structures and the ionic radii of Ce^{4+} and Pu^{4+} in CeO_2 and PuO_2, respectively (Ce^{4+}: 0.97 Å, Pu^{4+}: 0.96 Å, in eight fold coordination) and this is the motivation behind employing CeO_2 as the surrogate for PuO_2 in the present thesis. Kim et al. [65] have studied the applicability of cerium oxide, as a surrogate for plutonium oxide, for the fabrication of MOX (mixed oxide) fuel pellet. There are many other works as well which report the use of CeO_2 as the surrogate for PuO_2 [66, 67]. It must be stated that some reports express reservations about the use of CeO_2 as surrogate for PuO_2 for determining the thermo-physical behaviour such as heat capacity and thermal conductivity [68]. Table 1.2 lists few important properties of these oxides, which supports the use of CeO_2 as surrogate for PuO_2 [63, 64].

Neodymium oxide (Nd_2O_3) has been employed as a non-radioactive surrogate for two minor actinides namely, americium (III) oxide (Am_2O_3) and curium (III) oxide (Cm_2O_3) for various studies [69]. The major criteria for the selection of Nd_2O_3 as surrogate of Am_2O_3 and Cm_2O_3 is the similarity in their ionic radii (Nd^{3+}: 0.983 Å and 1.109 Å, Am^{3+}: 0.975 Å and 1.09 Å, in six and eight fold coordinations, respectively). Ionic radii of Cm^{3+} is 0.97 Å in six fold coordination [64]. Table 1.3 lists few important properties of these oxides, which supports the use of Nd_2O_3 as surrogate for Am_2O_3 and Cm_2O_3 [60, 64, 69, 70].

1.9. Research goals and objectives of the present work

From the earlier studies and literature survey, it is evident that zirconia, cubic stabilized zirconia and ceria based matrix could be the better choice among the oxide based materials as host matrix for transmutation of plutonium and MA in fast reactor and/or ADS system. Thus, considering the significance of Nd_2O_3 as minor actinide surrogate and zirconia as the matrix component, ZrO_2–$NdO_{1.5}$ binary system has been investigated and discussed in chapter 3 for phase relations and thermo-physical properties. Information on phase relations with varying $NdO_{1.5}$ loading would be useful to determine MA loading capacity in zirconia matrix while the thermo-physical properties are the essential pre-requisites for development and performance assessment of any materials for nuclear applications. In order to mimic loading of minor actinide (Nd_2O_3 as non-radioactive surrogate for minor actinides) in Y^{3+} doped ZrO_2 matrix, $Zr_{0.70}[Y_{1-x}Nd_x]_{0.30}O_{1.85}$ ($0.0 \leq x \leq 1.0$) system has been investigated for phase relation and thermal properties and discussed in chapter 4. In the chapter 5, the system $Nd_{0.20}[Zr_{1-x}Ce_x]_{0.80}O_{1.90}$ ($0.0 \leq x \leq 1.0$) has been discussed for phase relation and thermo-physical properties as the representative candidate for transmutation of both plutonium and MA. This system is expected to mimic the co-loading of Pu and minor actinides in ZrO_2 matrix. It is aimed to use radioactive PuO_2 directly instead of surrogate to investigate phase relation in YSZ/ZrO_2–PuO_2 system in chapter 6 in context of PuO_2 annihilation using IMF concept. In the chapter 7, the radiation tolerance of $Zr_{0.80}Nd_{0.20}O_{1.90}$, $Zr_{0.80}Nd_{0.20}O_{1.90}$–MgO (50 wt.%) composites and $Zr_{0.80}Nd_{0.10}Y_{0.10}O_{1.90}$ matrices has been described by employing 120 MeV Au ions as swift heavy ions (SHI) produced in accelerator. Finally all the findings are summarized in chapter 8.

CHAPTER 2

Experimental techniques

2.1. Introduction

A brief description on the preparative methods of materials and the techniques employed for their characterization and thermo-physical property evaluation is provided in this chapter. The conventional solid state method and gel combustion method have been used for the preparation of the materials and discussed in this chapter. The prepared materials have mostly been characterized by X-ray Diffraction (XRD), Raman spectroscopy, Scanning Electron Microscopy (SEM) and Energy Dispersive X-ray Spectroscopy (EDS). The thermo-physical properties like lattice and bulk thermal expansion have been measured by high temperature X-ray diffraction (HT-XRD) and dilatometry, respectively. Heat capacity of few samples has been measured by Differential Scanning Calorimeter (DSC). Thermal conductivity of few selected samples has been calculated from thermal diffusivity values measured by Laser Flash Apparatus (LFA). The swift heavy ion irradiation experiment was carried out at Inter University Accelerator Centre (IUAC), New Delhi, India using the 15 UD Pelletron Accelerator. The working principle of these techniques is also briefly discussed in this chapter.

2.2. Preparative methods

2.2.1. Solid state method

The solid-state synthesis method is the most conventional and widely used method to prepare polycrystalline materials [71, 72]. In this method, stoichiometric amount of constituent oxides (reactants) are mixed together to get a homogeneous mixture using mortar and pestle or ball mill. The mixture is then compacted into pellets and subjected to multiple stages heat treatment at elevated temperature in the range 1273 to 1873 K. All the heating steps are interspersed with grinding and mixing in order to obtain better homogeneity in the reaction products. The grinding process also produces smaller sized particles with higher surface area. It is one of the essential criteria required for increasing the rate of solid state reaction which is basically a diffusion controlled process [73]. With the progress of the reaction, thickness of product layer at the interfaces of reactants increases which in turn acts as diffusion barrier for ions of reactants. To break the diffusion barrier and to provide intimate contact between the reactants, intermittent grindings between two heating cycle is required. The feasibility of a reaction is dictated by thermodynamic considerations taking into account the change in Gibbs free energy for the formation of the product from constituent reactants, while rate of the reaction is determined by kinetic factors (Arrhenius equation) [72, 74]. The rate of solid state reaction is slow at lower temperature because much higher energy is required for displacement of ions from its lattice site and for diffusion through the crystal [74]. The temperature at which solid state reaction is performed mainly depends upon the melting point of the reactants and it is generally at least $T_M/2$ where T_M is the melting point of lowest melting components among the reactants and the products. Periodic X-ray diffraction analysis is generally carried out to monitor the progress of solid-state reaction and establish the appropriate reaction conditions for the completion of the reaction. Although the desired phase and composition can be achieved by solid state reaction, sometimes it is difficult to obtain a compositionally homogeneous product by this route, even when the reaction proceeds almost to completion [71]. However, there may be ingress of impurities during grinding and mixing in solid state reaction. It is also time consuming and energy intensive process. Still solid-state method has been widely used for the synthesis of solid materials.

2.2.2. Gel combustion method

The probability of in-homogeneity in products prepared by solid state method can be minimized by any chemical (solution based) methods, as prefect homogeneity at atomic level is achieved in solution state. Gel combustion [75, 76] is one such chemical method which can produce homogeneous and phase pure materials with improved powder characteristics like sub-micron and nano-sized particles with higher surface area, narrow size distribution and better sinterabilty etc. In gel-combustion synthesis, the metals of interest are taken in stochiometric ratio and are brought to nitrate form by dissolving in nitric acid. The nitrates are mixed together in an aqueous medium to produce a transparent mixed metal-nitrate solution. Appropriate amount of fuel (glycine, citric acid or urea) is then added to this mixed metal nitrate solution. The mixture is then dehydrated on a hot plate (at about 353–373 K) which transformed to a viscous liquid (hereafter termed as gel). The gel is further heated at a higher temperature (473–523 K) where the combustion reaction is initiated or triggered. The synthesis proceeds through a self-propagating exothermic reaction between the oxidant (metal nitrate of reactants) and fuel such as glycine with characteristics flame or fire and is termed as auto-ignition. The very high exothermic reaction makes the process self-propagating. Nitrates present in the reaction medium fulfill the requirement of oxidant by providing the oxygen for combustion of the fuel during the combustion reaction. The fuel also complexes with the different metal ions present in the solution, which prevents their selective precipitation and consequently brings homogeneity in the product. During the auto-ignition, gaseous products are evolved which dissipate the heat and fragment the product particle. Hence, the product of the reaction is obtained as ultra-fine powders of very large volume containing carbonaceous residue. The combustion synthesis may be influenced by fuel type, the fuel-to-oxidizer ratio (F/O) and the ignition temperature etc. The oxidant to fuel ratio is an important parameter for gel combustion process as it governs the exothermicity of the combustion reaction and hence the flame temperature which in turn governs the powder properties of final product. The gel combustion synthesis yields more homogeneous product compared to solid sate synthesis in absence of any precipitation during solvent evaporation and gel formation during combustion synthesis. However, it must be noted that during combustion synthesis huge volume of gaseous products along with large amount of heat is released in a very short duration. Hence, the experiment must be carried out in wide mouthed apparatus in a fume hood for easy liberation and safe ventilation of the gaseous products.

2.3. Characterization techniques

The brief overview of the techniques used in the present investigation for the characterization of materials and their thermo-physical property measurements is discussed in the following section.

2.3.1 Powder X-ray Diffraction (XRD)

X-ray diffraction is the most important characterization tool used in material science to obtain information about the structure of crystalline materials and the unit cell dimensions [72, 77]. The technique helps in the identification and characterization of materials based on their diffraction pattern. Diffraction occurs from the planes of crystalline materials when the wavelength of the X-ray beam is of the same order as that of the inter-planar spacing in crystals. The d spacing between various planes in the unit cell of a crystal is of the order of angstroms to few angstroms. Hence, the wavelengths of x-rays commonly applied for x-ray diffraction are between 0.7 and 2.3 Å to determine the atomic arrangement or structure of the crystalline materials. When an incident beam of monochromatic X-rays is made to fall on a sample material, it interacts primarily with electrons of atoms in sample resulting in scattered X-rays. The scattered x-rays interfere with each other resulting in constructive and destructive interference. This is known as diffraction. If the atoms have a periodic arrangement, the scattering produces a diffraction pattern with sharp maxima (peaks) at certain angles. The peaks in the X-ray diffraction pattern are directly related to the inter-planar spacing and are described by Bragg's law.

$$n\lambda = 2d_{hkl}\,\mathrm{Sin}\theta \qquad (2.1)$$

In this equation, θ is the Bragg angle, which is half of the scattering angle; n is an integer representing the order of the diffraction, λ is the wavelength of the x-ray and d is the inter-planar spacing for the plane (h k l). Thus, the directions of possible diffractions depend on inter-planer spacing which in turn depends on the size and shape of the unit cell of the material. The intensities of the diffracted beams depend on the kind and arrangement of atoms in the crystal. However, commonly used forms of materials are not single crystals but polycrystalline which is composed of many tiny crystallites oriented in all possible directions. When a polycrystalline material with randomly oriented crystallites is placed in an X-ray beam, the beam will interact with all possible inter-atomic planes. Now, if the scattering angle is systematically changed, all possible diffraction peaks from the sample will be detected. This is generally achieved in an X-ray diffractometer which consists of a source of monochromatic X-rays and a detector for the detection of diffracted X-rays. The angles and intensities of diffractions are recorded electronically in an X-ray diffractometer resulting in a plot of 2θ (horizontal axis) vs. intensity (vertical axis) for the sample known as diffraction pattern. The X-ray diffraction pattern of a pure substance is like a fingerprint of the substance. The powder diffraction method is thus being used for characterization and identification of polycrystalline phases. The diffraction pattern of an unknown mixture is usually compared with a powder diffraction file (PDF) collected and maintained by Joint Committee of Powder Diffraction Standards (JCPDS) for identification of phases present in the mixture. This is generally done using a search/match program. The other useful information like stress and strain on crystallites and solid solution formation may also be obtained from powder diffraction patterns. The high temperature XRD is useful to detect the phase changes (phase transition) occurring at elevated temperatures and to measure the thermal expansion of the crystalline materials.

In the present work, the formation of compounds were confirmed using a STOE theta-theta X-ray diffractometer employing Cu K_α radiation (λ = 1.54060 Å) and graphite monochromator. The graphite monochromator is used to eliminate K_β component of Cu X-ray radiation. NaI (Tl) was used as detector. The sample for analysis was ground and spread on a glass slide for phase analysis at room temperature. The samples were scanned in the range 10°–80° with an interval of 0.02° and counting time of 1 s. The recorded 2θ values were used for phase identification and calculation of lattice parameters using POWDERX software [78].

2.3.2. Raman spectroscopy

Raman spectroscopy is extensively utilised as an important complementary technique to X-ray diffraction. This is because Raman spectroscopy is sensitive to the oxygen sublattice of crystalline oxides, unlike XRD, which is mainly sensitive to the cation sublattice. As a result, the variations in lattice arrangements in anionic sublattice, which are difficult to detect with a lab X-ray source, can be studied using Raman spectroscopy. It basically probes the vibrational mode of the molecules. When the monochromatic radiation interacts with molecule or crystal, most of the photons are scattered off with the same energy (same wavelength or frequency) as the incident photons. The process is known as elastic scattering or Rayleigh scattering. However, a small fraction of light (approximately 1 in 10^7 photons) is scattered at frequencies different from the frequency of the incident photons. The scattering process is inelastic in nature and is termed as the Raman scattering. The scattering process is explained below with the help of simplified energy level diagram [79] as shown in Fig. 2.1. Any molecule at rest resides in the ground vibrational and electronic states. The electric field of the laser raises the energy of the system for an instant by inducing a polarization in the molecule. The polarized condition is not a true energy state and is widely referred to as a virtual state. Relaxation from the virtual state occurs almost instantaneously and predominately to the initial ground state. This process results in Rayleigh scattering. Relaxation to the first excited vibrational level results in a Stokes-Raman line.

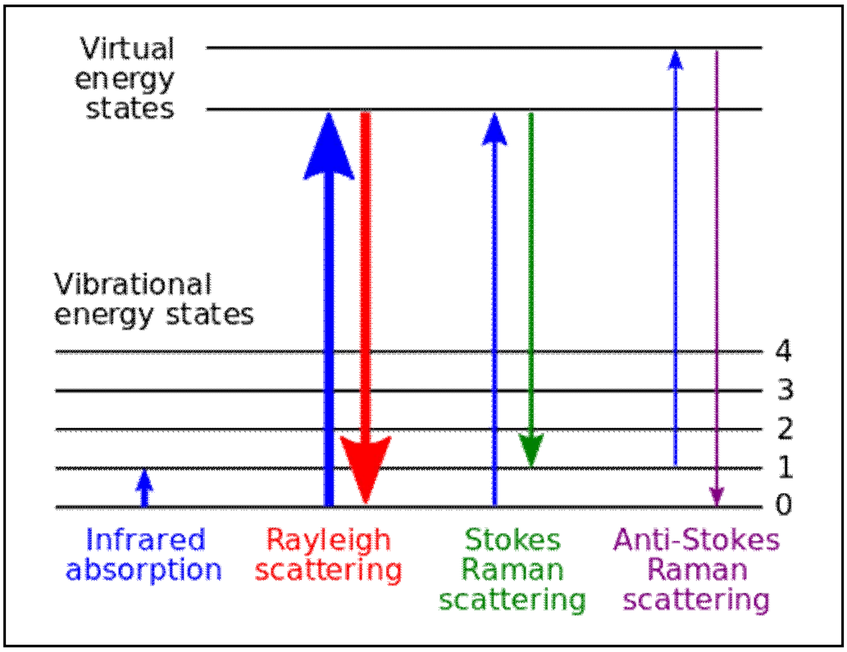

Fig. 2.1: Schematic representation of Raman scattering by energy-level diagram (adopted from Ref [79])

Stokes-Raman line appears at lower energy (longer wavelength) than that of the laser light. Most systems have at least a small population initially in an excited vibrational state. Thus, when the Raman process initiates from the excited vibrational level, relaxation may take place to the ground state which produces scattering of higher energy (shorter wavelength) than that of the laser light. This type of scattering is called anti-Stokes Raman scattering. The ratio of Stokes Raman and anti-Stokes Raman scattering depends on the population of the various states of the molecule. At room temperature, the number of molecules in an excited vibrational level is smaller than that of in the ground level, thus generally the intensity of Stokes Raman light is higher than anti-Stokes Raman light. In standard Raman spectrometer, more intense Rayleigh scattered light is rejected using a notch filter and only the Stokes Raman band is recorded. Usually, the intensity of this shifted light (Stokes line) versus frequency is plotted which results in a Raman spectrum of the sample. Generally, Raman spectra are plotted with respect to the laser frequency such that the Rayleigh band lies at 0 cm^{-1}. On this scale, the band positions will lie at frequencies that correspond to the energy levels of different vibrational modes. Raman spectra of sintered samples have been recorded on a micro/macro-Raman spectrometer (Model: LABRAM-1, Horiba Jobin-Yvon, France) using 632.8 nm line of a He-Ne laser (~ 17mW power) for excitation. The scattered Raman signal was collected in back scattering geometry using a single monochromator spectrometer equipped with a Peltier-cooled CCD detector. Specimen were prepared in the form of small pellets and the laser light was focused on flat surface of the specimen using an optical microscope (Model: Olympus BX-40, 50x objective lens) connected to the spectrometer. Each spectrum was recorded with 2 s scan duration and averaged over 50 repeated scans. Spectral resolution of the system was 2 cm^{-1}.

2.3.3. Scanning Electron Microscopy (SEM) equipped with EDS

The scanning electron microscope (SEM) provides information on topographical features, morphology and phase distribution of samples. In SEM, image of a sample is produced when its surface is scanned with a focused beam of electrons. When these electrons interact with atoms of the sample, electrons and x-rays with a wide range of energies are produced. These are secondary electrons (SE), backscattered electrons (BSE), characteristic X-rays, continuum X-rays, visible light and heat. Secondary electrons and backscattered electrons are commonly used for imaging of samples. Secondary electrons provide morphology and topography of samples while the backscattered electrons generate contrasts in composition in multiphase samples. The characteristic X-rays are used for compositional analysis. It is carried out in energy dispersive X-ray analysis system (EDS) equipped with SEM. In the present work, microstructure of the sintered pellets has been investigated using a scanning electron microscope operated at 20 kV acceleration potential. The surfaces of these pellets were sputter-coated with gold before recording the images to avoid charging interference. Images were taken using secondary electron (SE) mode (Everhart-Thornley detector) as well as back scattered electron (BSE) mode (Solid state back scattered electron detector). Energy dispersive spectroscopy (EDS, 80 mm^2, silicon drift detector) has been utilized to obtain elemental mapping of the region of interest.

2.4. Thermo-physical property measurement techniques

Information on thermo-physical properties of nuclear fuels is very essential for fuel pin design, predicting in-pile fuel performance and core accident analysis of reactor system. Knowledge of thermal expansion of nuclear materials is important to estimate the extent of swelling under thermal stress. The lower thermal conductivity of fuel results in large temperature gradient in the radial direction of the fuel pellet and is the driving force for fuel restructuring. It also results in high centreline temperature of the fuel which controls fission gas release. The thermal conductivity of nuclear fuel determines the linear power. Therefore, important thermo-physical properties such as thermal expansion, heat capacity and thermal conductivity have been measured for selected compositions and reported in this thesis.

2.4.1. Thermal expansion

The thermal expansion defines the change in dimensions of any material as a function of temperature at atmospheric pressure. This is known as bulk thermal expansion. The change in dimensions of the unit cell (cell parameters) as a function of temperature is known as lattice thermal expansion. The origin of thermal expansion is generally explained by the nature of the inter-atomic potential well of a diatomic molecule [80]. With increase in temperature, the population of higher energy vibrational levels increases. As a result, there is an increase in the average inter atomic distances with increase in temperature due to asymmetric nature (anharmonicity) of potential energy well. This increase in the average inter-atomic distance contributes to the thermal expansion. The increase in average inter-atomic distance increases with an increase in the degree of the asymmetry of the potential well. The extent of the asymmetry is dependent on the bond strength. A stronger bond results in a more symmetric potential well resulting in comparatively smaller thermal expansion. Although this model only strictly applies to very simple molecule, it still appears to be the most important mechanism for thermal expansion in solids.

The thermal expansion coefficient is generally calculated to measure the thermal expansion in solids quantitatively. In this study, lattice thermal expansion has been measured by high temperature X-ray diffraction (HT-XRD) whereas bulk thermal expansion has been measured by dilatometry.

2.4.1.1. Lattice thermal expansion by HT-XRD

In order to measure the lattice thermal expansion, the XRD patterns are recorded *in situ* at various temperatures. The unit cell parameters are then determined as a function of temperature by refining XRD patterns obtained at different temperatures. The percentage lattice thermal expansion and average lattice thermal expansion coefficient (α_a) are computed using the experimental data from the expression:

$$\%\ \text{lattice thermal expansion} = \{(a_T - a_{298})/a_{298}\} \text{ x } 100 \qquad (2.2)$$

$$\text{lattice thermal expansion coefficient } (\alpha_a) = (a_T - a_{298})/\{a_{298} \text{ x } (T\text{-}298)\} \qquad (2.3)$$

In the above expression, a_{298} and a_T represents the lattice parameter at ambient and at temperature ‘T’, respectively. The most important advantage of X-ray diffraction technique is that the experiment requires small amount of powder sample and the presence of other phases does not affect the measurement. The data on thermal expansion obtained by high temperature XRD are also not affected by porosity or thermally generated vacancies in the solid.

The high temperature X-ray diffraction has been carried out on a STOE powder diffractometer (θ-θ geometry) fitted with HDK-2.4 high temperature attachment and a high vacuum heating stage. Powdered samples were spread over the platinum heating stage and diffraction patterns were recorded (2θ = 20–65°) over the temperature range from RT to 1273 K at 100 K interval using Cu Kα radiation (1.5406 Å). Sample temperature was measured using a S-type thermocouple and controlled within ± 1 K using a PID temperature controller. Silicon and platinum stages were used for instrument calibration.

2.4.1.2. Bulk thermal expansion using dilatometry

Bulk thermal expansion of sintered samples has been measured over RT to 1673 K in an integrated thermo-mechanical analyzer (Setsys Evolution TMA 1600). The expansion of the pellet under zero load condition was measured as a function of temperature when subjected to the controlled temperature program. The change in length of the sample due to heating resulted in the movement in the pushrod which was detected by the linear variable differential transformer (LVDT) giving rise to an electrical signal and transmitted to the analog to digital converter. TMA system was calibrated by recording the linear thermal expansion of NIST sapphire standard reference material (SRM) and results were found within ± 1% of the recommended values. A uniform heating/cooling rate (10 K/min.) was used and experiments were carried out under flowing helium atmosphere (~ 60 ml/min.). Average coefficient of bulk thermal expansion (CTE) was calculated using the expression:

$$\alpha_L = \{(L_{T2} - L_{T1})/(T_2 - T_1)\}/ L_{T1} \qquad (2.4)$$

where, 'L_{T2}' and 'L_{T1}' represents length at temperature 'T_2' and temperature 'T_1', respectively.

2.4.2. Heat capacity

Specific heat capacity is defined as the amount of energy required to raise the temperature by one Kelvin per unit mass of a material.

The heat capacity could be measured either at constant pressure (P) or at constant volume (V) and is expressed as:

$$C_i = 1/m\ (\Delta Q/\Delta T)_i \qquad (2.5)$$

where ΔQ is the energy input to the system, and ΔT is the change in temperature, m is mass, C is specific heat capacity and i = pressure (P) and volume (V).

Most experiments carried out in the lab are at constant pressure and hence the measured heat capacity is basically C_P. It is very difficult to measure C_v directly. It must be mentioned that there is a very small difference between C_P and C_V for solids particularly at the pressures and temperatures at which experiments are carried out. In the present investigations, heat flux type Differential Scanning Calorimeter (DSC) [81-83] has been employed for the measurements of heat capacity.

2.4.2.1. Heat capacity measurement by DSC

For the heat capacity measurements by heat flux type DSC (model number DSC 823e/700 of M/s. Mettler Toledo GmbH, Switzerland), conventional three-step method consisting of blank run, reference run and sample run was used. The heat flow rate of blank run Φ_0 (T) was determined using empty pans both in the sample and the reference side. The heat flow rate of reference and sample run was determined by placing reference and sample of known mass in the sample pan respectively keeping other conditions unaltered. The specific heat capacity, C_p (Sample) (at a given temperature) was calculated by a simple comparison of heat flow rates of the sample and sapphire using the following equation [83]

$$C_p(\text{Sample}) = \frac{C_p(\text{ref}) \cdot (\Phi_{\text{sample}} - \Phi_o) \cdot m_{\text{ref}}}{(\Phi_{\text{ref}} - \Phi_o) \cdot m_{\text{sample}}} \qquad (2.6)$$

where C_p (Sample) and C_p (Ref) are the specific heat capacity of sample and sapphire (reference material), respectively; m_{Sample} and m_{Ref} represent corresponding mass values and $\Phi_{\text{Sample},}$ Φ_{Ref} and Φ_o are the respective heat flow rate for the sample, reference and the blank runs. Prior to measurements, temperature and heat flow calibration was performed by using respective melting point and enthalpy of fusion of highly pure In, Zn and Pb.

2.4.3. Thermal conductivity

Thermal conductivity is a measure of material’s ability to conduct heat. It appears primarily in Fourier's law for heat conduction and is given by

$$Q = - \lambda \, dT/dX \tag{2.7}$$

where Q is the heat flux (amount of thermal energy flowing through a unit area per unit time) and dT/dX is the temperature gradient and λ is thermal conductivity. There are steady-state and transient techniques for measuring the thermal conductivity in materials [84]. In the present investigation, laser flash method (transient method) was employed to measure thermal diffusivity of the samples to estimate its thermal conductivity [85]. The flash method for measuring the thermal diffusivity of solid materials was first proposed by Parker et al. in 1961 [86]. Later on, Deem et al. [87] utilized a ruby laser instead of flash lamp and demonstrated its suitability as energy source. In this method, the sample is usually a solid planar-shaped material. The laser source is used to heat the sample’s front side uniformly and a detector is used to measure the time-dependent temperature rise at the rear side. Heat conduction is assumed to be one-dimensional (i.e. no lateral heat loss). The sample is usually prepared by spraying a layer of graphite on its both sides to act as an absorber on the front side and as an emitter on the rear side for temperature sensing. In the present case, cylindrical disc-shaped samples of 10.0 mm diameter and approximately 1 mm thickness were used for diffusivity measurement. Diffusivity measurements were carried out over the temperature range from 298–1473 K with 100 K interval under dynamic vacuum atmosphere ($P < 2 \times 10^{-5}$ mbar). The rear surface time-temperature profile of the samples was monitored by liquid nitrogen cooled In-Sb IR detector and plotted online with the help of Proteus® software. Temperature stability was maintained within ± 0.1 K and four laser shots were given at each temperature. Diffusivity values were calculated from the half time of the maximum rise in detector signal ($t_{1/2}$) and employing ‘Radiation + pulse correction’ method, which is recommended for low diffusivity ceramic substances. The following expression was used for calculation of diffusivity [86]:

$$D = WL^2/t_{1/2} \tag{2.8}$$

where 'D' is thermal diffusivity, 'W' is heat loss parameter (0.1388), 'L' = sample thickness and '$t_{1/2}$' = time taken to reach the 50% of the maximum rise in rear surface temperature. The mean of all shots on a given temperature were taken as average diffusivity value. Performance of laser flash apparatus was checked using Pyroceram 9606 standard and diffusivity values were found to match with recommended values over a range of ± 4% (at RT) to ± 2% (at 1100 K).

Thermal conductivity '$\lambda(T)$'was calculated using the following relation:

$$\lambda(T)= D(T)\times C_p(T)\times\rho(T) \tag{2.9}$$

where 'D(T)' is measured thermal diffusivitiy, '$C_P(T)$' is specific heat capacity and '$\rho(T)$' is the sample density at temperature 'T'. Since the sintered specimen was not fully (100%) dense, the evaluated thermal conductivity data 'λ_m' were corrected for porosity to estimate the thermal conductivity of fully dense material 'λ_{100}' by using the following relation [88]:

$$\lambda_m/\lambda_{100} = 1 - 4*P/3 \tag{2.10}$$

Where, 'P' is fractional porosity; calculated from the theoretical density '(ρ_t') and measured density 'ρ_m' as:

$$P = (\rho_t - \rho_m)/\rho_t \tag{2.11}$$

2.4.4. Density measurement

The geometric density of the sample was calculated from mass to volume ratio. Volume was calculated from the geometry and dimensions of the sample (for regularly shaped sample). The temperature dependent density '$\rho(T)$' was evaluated from bulk thermal expansion data and room temperature density value.

2.5. Ion irradiation

The effect of fission fragments (FF) on the fuel matrices can be simulated by irradiating them with swift heavy ions (SHI) with masses and energies similar to that of FF. The heavy ion irradiation experiment was carried out using 15 UD Pelletron Accelerator [89, 90]. The accelerator is installed in vertical orientation in an insulating tank filled with SF_6 gas. A schematic diagram of the 15UD Pelletron is shown in Fig. 2.2 [91]. The ion source which is located at the top of the accelerator produces negative ions. The negative ions of interest are produced by cesium sputtering of that particular substrate. The MCSNICS (Multi Cathode Source of Negative Ions by Cesium Sputtering) is mostly used for the negative ion production. The negative ions are pre-accelerated to ~ 300 KeV and then injected into a strong electrical field inside the accelerator tank using injector magnet. A very high voltage positive terminal which is generally maintained at ~ 15 MV is located at the center of the vertical accelerating tank. Thus, a potential gradient is maintained through the tank from the top of the tank to the terminal and from terminal to the bottom. The negative ions when travelling from the top of the accelerating tank to the positive terminal get accelerated. On reaching the terminal, they are forced to pass through a stripper, which removes some electrons from the negative ions thereby transforming the negative ions into positive ions. The stripper may be a very thin carbon foil or a small volume of gas. N_2 has been used as stripper for this experiment. These positive ions are then repelled away from the positively charged terminal and are accelerated to ground potential to the bottom of the tank. In this manner, same terminal potential is used twice to accelerate the ions. These positive ions are then guided to exit from the tank using the analyzer magnet which also helps in selecting the particular energy of the ion. The switching magnet which is placed after the analyzer magnet helps to switch over the beams to any of the beam lines in the facility.

The energy gained by the ions after emerging out of the accelerator is given by

$$E_{Final} = E_0 + V(q + 1) \qquad (2.12)$$

if only single stripper is used, where E_0 is the energy gained from the ion source, V is the terminal potential and q is the charge state of the ion.

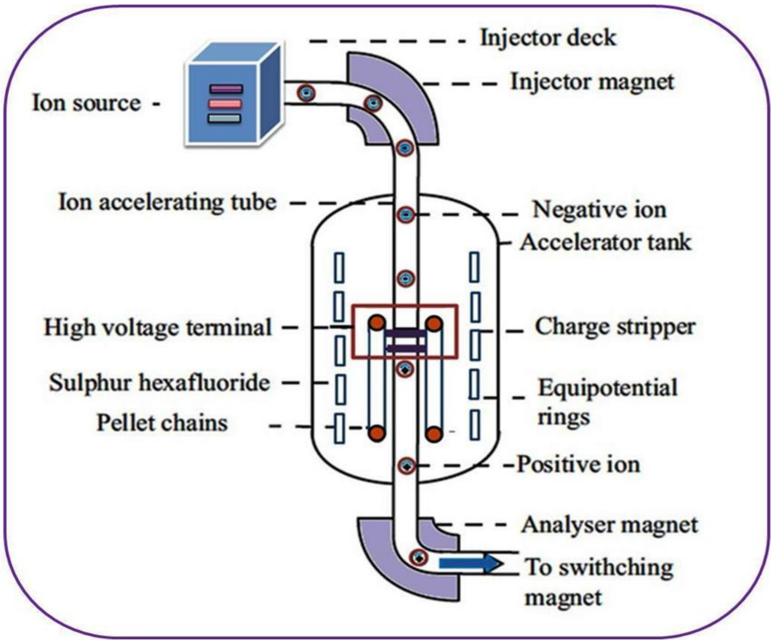

Fig.2.2: Schematic diagram of IUAC Pelletron Accelerator (adopted from ref [91])

The equation shows that the energy of ions is governed by the terminal potential and the charge state of the ion. The charge state is controlled by the stripper. The gas stripper selects lower charge state where as the carbon foil is used to select the higher charge state. The pressure in the chamber is maintained at 1 x 10^{-6} torr during the irradiation experiment. In the present study, 120 MeV Au ion produced in the accelerator was used to simulate radiation damage effects of FF in materials.

The results and data generated using these techniques will be discussed in subsequent chapters.

CHAPTER 3

Synthesis, characterization and thermo-physical properties in $Zr_{1-x}Nd_xO_{2-x/2}$ ($0.0 \le x \le 1.0$) system

---

3.1. Introduction

As already discussed, among oxide based materials, zirconia-based ceramics are the potential candidates for minor actinides (MAs) transmutation [42, 52] and conditioning [92]. On the other hand, neodymium oxide (Nd_2O_3) has been employed as a non-radioactive surrogate for minor actinides, americium (III) oxide (Am_2O_3) and curium (III) oxide (Cm_2O_3) for various studies [69]. Thus, considering the significance of Nd_2O_3 as the MA surrogate and zirconia as the matrix component, ZrO_2–$NdO_{1.5}$ binary system has been investigated and discussed in this chapter. This study aims at synthesis, characterization and thermo-physical property evaluation of the nominal compositions in $Zr_{1-x}Nd_xO_{2-x/2}$ ($0.0 \le x \le 1.0$) series. Information on phase relations with varying $NdO_{1.5}$ content would be useful for determining MA loading capacity in zirconia matrix. The thermo-physical properties of selected compositions have also been evaluated. These are essential requirements for development of any transmutation target.

3.2. Experimental

Analytical reagent (AR) grade Nd_2O_3, $ZrO(NO_3)_2.5H_2O$ and glycine have been used as starting materials. All the nominal compositions in the series have been prepared by gel combustion route which is described in detail in chapter 2. All combustion reactions have been performed in fuel-deficient (fuel:oxidant = 40:60) ratio. To remove the residual carbon, as-combusted powders have been calcined at 873 K for 1 h in static air. Calcined powders have then been finely ground, pelletized and sintered at 1723 K for 48 h in static air. The sintered samples have been thoroughly characterized by X-ray Diffraction (XRD), Raman Spectroscopy, Scanning Electron Microscopy (SEM) and Energy Dispersive Spectroscopy

(EDS). The lattice and bulk thermal expansion of few selected compositions have been measured by high temperature XRD (298–1273 K) and dilatometry (300–1673 K), respectively. Thermal conductivity has been reported for the representative composition $Zr_{0.80}Nd_{0.20}O_{1.90}$.

3.3. Results and discussion

3.3.1. Structural characterization

3.3.1.1. X-ray diffraction studies

Room temperature XRD patterns of sintered samples in $Zr_{1-x}Nd_xO_{2-x/2}$ ($0.0 \leq x \leq 0.6$) series are shown in Fig. 3.1 (a) and 3.1(b). Pure ZrO_2 (x = 0.0) crystallizes in monoclinic structure ($P2_1/n$) as confirmed from XRD pattern. On incorporation of 10 mol% $NdO_{1.5}$ (x = 0.1), diffraction pattern indicates a biphasic mixture consisting of monoclinic zirconia (m-ZrO_2) and fluorite-type Nd-stabilized cubic zirconia. Further incorporation of Nd^{3+} (x = 0.2) results into disappearance of monoclinic zirconia phase and XRD pattern shows peaks corresponding to Nd-stabilized zirconia only. It indicates that while 20 mol% Nd^{3+} incorporation stabilizes higher symmetry (cubic) zirconia phase, 10 mol% doping is insufficient for complete stabilization into single-phasic cubic zirconia and therefore monoclinic phase still appears in XRD. Interestingly, for 10 mol% $NdO_{1.5}$ doped sample, peak positions of monoclinic phase do not show any measurable shift from pure m-ZrO_2 (x = 0.0). This observation suggests that m-ZrO_2 may be present as a pure phase. A close look at diffraction patterns indicates broadening of peaks corresponding to monoclinic phase (e.g., FWHM = 0.186° for x = 0.0 and 0.234° for x = 0.1; for (111) peak at 2θ 31.48°). Crystallite size induced broadening is ruled out as the samples have been treated at high temperatures (1723 K). Thus, such broadening is indicative of lattice strain; which could possibly be due to presence of small amount of Nd^{3+} (and corresponding oxygen ion vacancies) in monoclinic lattice. Literature also indicates low solubility of Nd^{3+} in m-ZrO_2 [93].

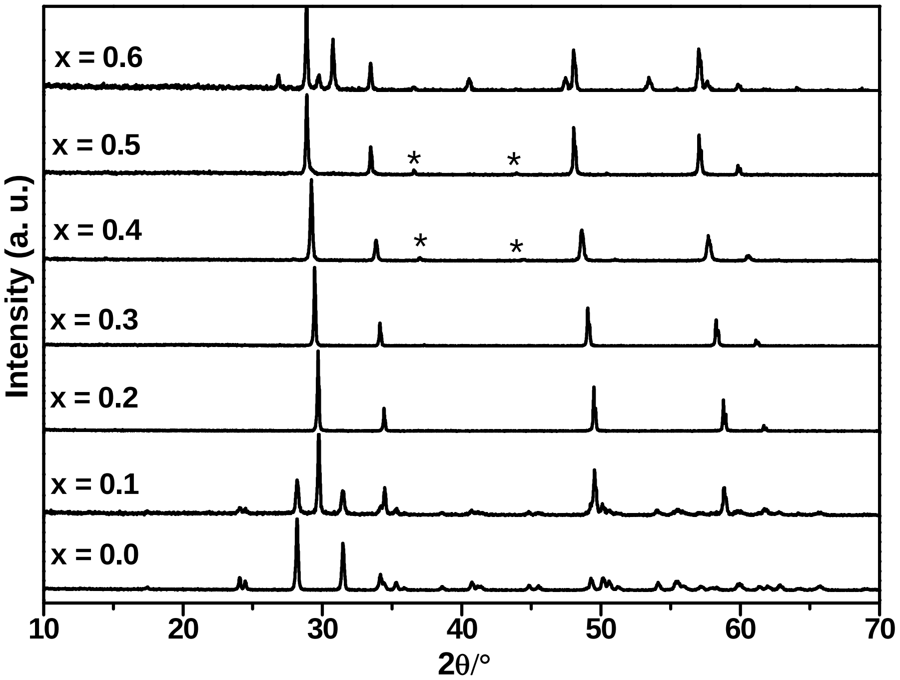

Fig. 3.1(a): XRD patterns of sintered $Zr_{1-x}Nd_xO_{2-x/2}$ ($0.0 \leq x \leq 0.6$) samples; pyrochlore superstructure peaks are marked by *

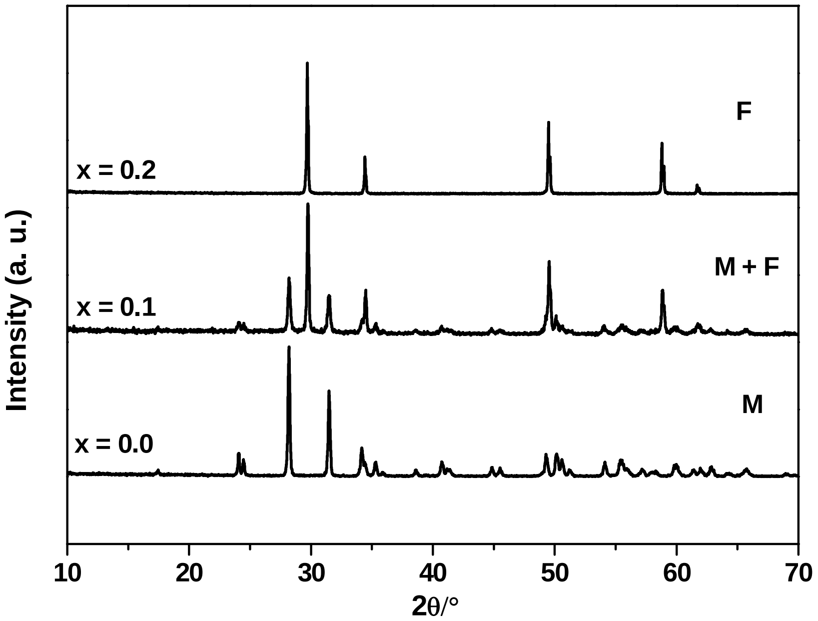

Fig. 3.1(b): Phase evolution with $NdO_{1.5}$ incorporation in ZrO_2, as revealed by XRD in $Zr_{1-x}Nd_xO_{2-x/2}$ ($0.0 \leq x \leq 0.2$) samples; M: monoclinic, F: fluorite

It is therefore suggested that composition with x = 0.1 to be a mixture of Nd-doped monoclinic zirconia and Nd-stabilized cubic zirconia.

In m-ZrO_2, Zr^{4+} ion is seven coordinated (ionic radius ~ 0.78 Å; CN = 7) [64]. Dopant Nd^{3+} is larger (ionic radius ~ 0.983Å; CN = 6 and 1.109 Å; CN = 8) [64] than Zr^{4+} and when substitutes for it, increases the effective cation size thereby enabling an increase in effective co-ordination number of Zr^{4+} to 8. This drives the resulting phase transition from monoclinic to higher symmetry (cubic) form. Also, substitution of Zr^{4+} by Nd^{3+} introduces additional oxygen vacancies in the lattice to maintain electro-neutrality, which relaxes the crystal structure and promotes the formation of cubic defect fluorite structure, attributed to increased configurational entropy.

XRD patterns with further $NdO_{1.5}$ incorporation (x = 0.2, 0.3, 0.4, 0.5 and 0.6) are shown in Fig. 3.1(a) and 3.1(c). With higher substitution ($x \geq 0.2$), monoclinic phase disappears and stabilized zirconia phase field dominates. The pyrochlore phase; characterized by superstructure reflections in XRD patterns marked by asterisk (*) due to long-range ordering of the cations, appear at 2θ 37° (3 3 1) and 45° (5 1 1) for the compositions $x \geq 0.4$ in Fig. 3.1(a). However, upon close observation, as shown in Fig. 3.1(c) with superstructure peaks marked by asterisk (*), it is evident that ordered pyrochlore phase domains exist from lower Nd^{3+} doping level (x = 0.3 onwards) also and is prominent with x = 0.5; the perfect pyrochlore stoichiometry. Hence, it can be inferred that micro domains of pyrochlore start to appear in macro domains of defect fluorite right from the composition x = 0.3 and it becomes dominant phase at composition x = 0.5. It may be noted that there is a general consensus among various groups that a hybrid region consisting of fluorite-type and pyrochlore-type micro-domains exist on both side of stoichiometic pyrochlore $Nd_2Zr_2O_7$ (Nd:Zr = 1:1), the composition from which (hybrid region) starts differ widely in literature [94, 95] plausibly attributed to different synthetic route and heat treatment.

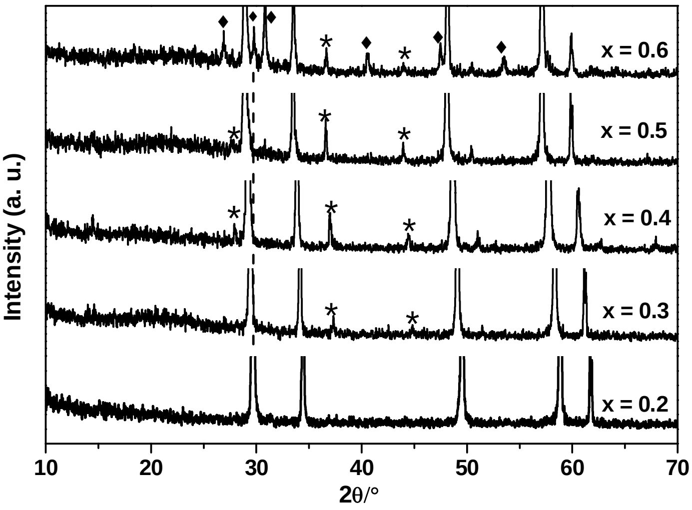

Fig. 3.1(c): Expanded view of XRD patterns of $Zr_{1-x}Nd_xO_{2-x/2}$ (0.0 ≤ x ≤ 0.6) showing existence of pyrochlore type ordering, pyrochlore superstructure peaks are marked by * and hexagonal Nd_2O_3 phase is marked by ♦

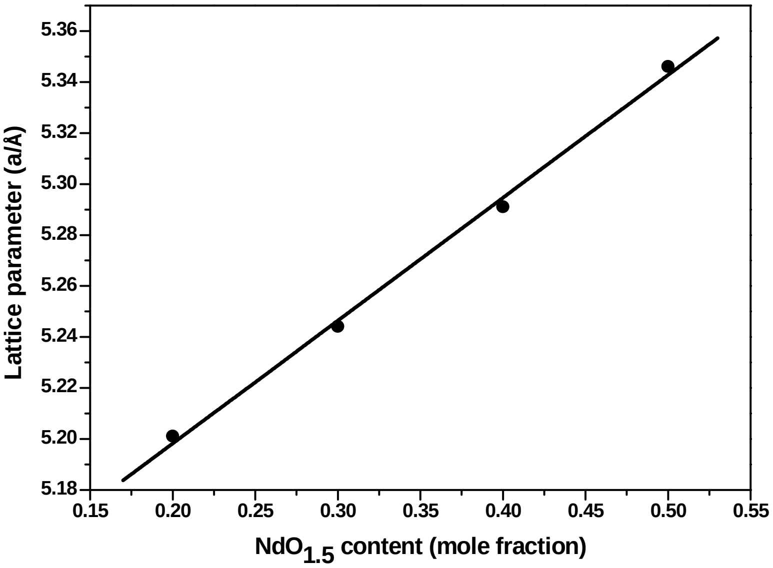

Fig. 3.2: Variation of lattice parameter as a function of $NdO_{1.5}$ mole fraction in $Zr_{1-x}Nd_xO_{2-x/2}$ (0.2 ≤ x ≤ 0.5) samples

Shlyakthina et al. [94] observed fluorite type phase for 18, 22 and 26 mol% Nd^{3+} content in ZrO_2. They also observed pyrochlore type phase in the composition range 30–50 mol% of Nd^{3+} content in ZrO_2. According to Van Dijk et al., [95] ZrO_2 with 25 mol% of Nd^{3+} was found to be fluorite-type by XRD. However, neutron diffraction pointed towards some weak pyrochlore-type ordering in this composition. In the present case, in composition range x = 0.3–0.5, the intensity of superstructure peaks increases suggesting increase in long range order in the cation and anion sublattice. It must be noted that very weak superstructure peaks in the nominal composition with x = 0.3 classifies it as largely fluorite-type with very weak ordering in contrast to the nominal composition with x = 0.4 which is largely pyrochlore. Anithakumari et al. showed the existence of fluorite type domains in the pyrochlore matrix for the composition $Zr_{0.60}Nd_{0.40}O_{1.80}$ using Selected Area Electron Diffraction (SAED) technique [96]. Thus, a continuous transition from defect fluorite structure to pyrochlore structure is observed in this composition range. The absence of superstructure reflections for lower doping levels (x = 0.2) can be attributed to relatively lower concentration of Nd^{3+} ions, which is not enough to cause cation ordering (Zr^{4+}/Nd^{3+}) in the structure and therefore only stabilized zirconia (or defect fluorite) phase field is observed. For Nd^{3+} content higher than x = 0.5, pyrochlore ordering is observed along with phase separation of hexagonal Nd_2O_3 phase [JCPDS Card No.: 43-1023]. Therefore, it is quite likely that these compositions (x > 0.5) consist of ordered pyrochlore and hexagonal Nd_2O_3 phase domains. No systematic shift is observed in the peak positions of hexagonal Nd_2O_3 phase for compositions with x = 0.6–1.0 which indicates that Zr^{4+} is not incorporated into h-Nd_2O_3 lattice. This is further accompanied by almost invariance in the pyrochlore peak positions. Since ordered pyrochlore and defect fluorite (a class of stabilized zirconia) phases essentially differ in terms of cation/anion ordering, their relative fractions would depend upon the processing conditions (sintering temperatures, sintering time, cooling rates, etc.).

All XRD patterns have been refined using POWDERX software [78] and lattice parameters for the dominant phase have been determined. Details of various phases present and the lattice parameters of dominant phase (defect fluorite/pyrochlore) for different compositions are given in Table 3.1. Variation of lattice parameter of cubic stabilized zirconia (defect fluorite) phase as a function of composition is plotted in Fig. 3.2 and is observed to follow Vegard's law. It must be noted that lattice parameters of pyrochlore-type solid solutions have been halved to compare with the defect fluorite phases. Linear increase in lattice parameter of defect fluorite phase with increasing Nd^{3+}content (for x = 0.2, 0.3) and that of the pyrochlore phase (for x = 0.4, 0.5) can be attributed to increase in average cationic radius on substitution of smaller Zr^{4+} ions by larger Nd^{3+} ions (ionic radii of Nd^{3+}= 1.109Å, Zr^{4+} = 0.84Å in eight-fold coordination) [64].

From phase analysis as discussed above, it is obvious that 10 mol% $NdO_{1.5}$ is not sufficient to stabilize the cubic phase of zirconia. Complete stabilization of ZrO_2 occurs in the composition range x = 0.2 to 0.5. It is interesting to note that the lattice parameter of cubic zirconia phase observed for the nominal composition with x = 0.1 is approximately equal to lattice parameter of fully stabilized zirconia for the composition x = 0.2. It suggests that the actual composition of cubic phase observed for $Zr_{0.90}Nd_{0.10}O_{1.95}$ could be close to $Zr_{0.80}Nd_{0.20}O_{1.90}$. This implies that approximately 20 mol% $NdO_{1.5}$ is essential to obtain stabilized zirconia phase.

3.3.1.2. Raman spectroscopic studies

It is known that Raman spectroscopy is quite sensitive to oxygen sublattice structure of crystalline oxides and complements the information obtained from XRD studies, which is mainly sensitive to cation sublattice structure. To gain further understanding of structural variation in $Zr_{1-x}Nd_xO_{2-x/2}$ (0.0 ≤ x ≤ 0.6) series with increase in Nd^{3+}-content; Raman studies have been carried out.

Table 3.1: Phases present in various $Zr_{1-x}Nd_xO_{2-x/2}$ (0.0 ≤ x ≤ 1.0) compositions and lattice parameter of dominant phases (⊕: not refined)

Composition	Phases identified by XRD patterns	Lattice parameter (Å)
ZrO_2	Monoclinic	a = 5.148(1), b = 5.203(1), c = 5.314(1), β = 99.247°
$Zr_{0.90}Nd_{0.10}O_{1.95}$	Monoclinic ZrO_2 Stabilized zirconia (Defect fluorite)	⊕ 5.201(2)
$Zr_{0.80}Nd_{0.20}O_{1.90}$	Stabilized zirconia (Defect fluorite)	5.205(1)
$Zr_{0.70}Nd_{0.30}O_{1.85}$	Stabilized zirconia (Defect fluorite)	5.248(1)
$Zr_{0.60}Nd_{0.40}O_{1.80}$	Pyrochlore	10.586(2)
$Zr_{0.50}Nd_{0.50}O_{1.75}$	Pyrochlore	10.700(1)
$Zr_{0.40}Nd_{0.60}O_{1.70}$	Pyrochlore Hexagonal Nd_2O_3	10.687(3) ⊕
$Zr_{0.30}Nd_{0.70}O_{1.65}$	Pyrochlore Hexagonal Nd_2O_3	10.704(2) ⊕
$Zr_{0.20}Nd_{0.80}O_{1.60}$	Pyrochlore Hexagonal Nd_2O_3	10.692(4) ⊕
$Zr_{0.10}Nd_{0.90}O_{1.55}$	Pyrochlore Hexagonal Nd_2O_3	10.701(5) ⊕
$NdO_{1.5}$	Hexagonal	a = 3.829(1), c = 5.991(2)

As-recorded Raman spectra of sintered samples are shown in Fig. 3.3. Undoped ZrO_2 (x = 0.0), which has monoclinic crystal structure, shows a complex spectrum with 15 distinguishable Raman bands over the range 100–800 cm^{-1}. Factor group analysis of monoclinic ZrO_2 predicts 18 Raman active modes [97], however all of these are not distinguishable in present experimental data. The Raman modes observed around 101, 176, 188, 220, 303, 331, 345, 380, 474, 501, 536, 557, 613, 635 and 754 cm^{-1} are in good agreement with the literature data reported for m-ZrO_2 [97]. Upon initial $NdO_{1.5}$ substitution (x = 0.1), overall nature of spectrum remains same as observed for undoped ZrO_2. However, close inspection reveals few variations as shown in Fig. 3.4. Upon 10 mol% $NdO_{1.5}$ doping, (i) peak intensities reduce significantly under similar measurement conditions, (ii) peak positions shift marginally towards lower wave numbers and (iii) peaks get broadened compared to undoped ZrO_2. These results suggest that while 10 mol% $NdO_{1.5}$ doping still retains m-ZrO_2 as the bulk phase, it renders more cation disorder in doped sample. A marginal red shift in peak position indicates relaxation in vibrational frequencies due to incorporation of larger Nd^{3+} ions (lattice expansion) and creation of oxygen ion vacancies. Compared to XRD results, Raman spectrum of 10 mol% $NdO_{1.5}$ doped sample does not show Raman bands due to stabilized zirconia phase. However, an interesting evidence for co-existence of stabilized zirconia is the variation in relative intensities of Raman bands at ~ 612 and ~ 635 cm^{-1}. In pure m-ZrO_2, the latter band has higher intensity, however in the composition with 10 mol% Nd^{3+}, the intensity of former increases. It must be noted that stabilized zirconia shows a broad major band at 600–610 cm^{-1} and hence this change in intensity could be attributed to appearance of stabilized zirconia phase. Additionally, a weak shoulder peak around 267 cm^{-1} (indicated by asterisk in Fig. 3.4, also shown in inset), could be observed which is the highest intensity peak for tetragonal zirconia [98]. It is therefore possible that the stabilized phase has some tetragonal domains present along with major monoclinic phase. Such an existence of mixed (monoclinic + tetragonal) phase in partially stabilized zirconia (in YSZ system) has been reported earlier as well [98]. The reason for not observing distinct Raman bands for Nd^{3+}-stabilized cubic zirconia phase could be due to its highly defective/disordered structure. With Nd^{3+} incorporation (that causes disorder in cation sublattice) and creation of additional oxygen ion vacancies in the lattice, the translational symmetry is lost and optical phonons from all over the Brillouin zone participate in first-order spontaneous Raman scattering thus exhibiting a broad spectrum which is significantly lower in intensity as compared to crystalline monoclinic phase and hence not observed. With higher $NdO_{1.5}$ substitution (x = 0.2, 0.3, 0.4 and 0.5), Raman spectra evolve differently as shown in Fig. 3.3. 20 mol% Nd^{3+}-doped composition shows two broad bands of almost equal intensity; centered around 600 and 330 cm^{-1}. Broad band around 600 cm^{-1} is characteristic of cubic stabilized zirconia (F_{2g} mode) having defect fluorite structure. Such band has been reported to appear around 610 cm^{-1} for yttria stabilized zirconia (YSZ) [99]. With 30 mol% $NdO_{1.5}$, while F_{2g} band of fully stabilized zirconia (~ 601 cm^{-1}) remains nearly invariant, the low energy band (~ 330 cm^{-1}) gains intensity and splits into two bands centred around 312 and 406 cm^{-1}. Further $NdO_{1.5}$ substitution (x = 0.4) results into four distinct Raman bands positioned at 301, 396, 521 and 587 cm^{-1}. These bands are characteristic of ordered pyrochlore zirconates arising from all the allowed Raman modes of a pyrochlore lattice [100, 101]. These results corroborate the inference taken from XRD studies. Beyond 20 mol% $NdO_{1.5}$, ordering of Nd^{3+} and Zr^{4+} ions is favoured leading to appearance of ordered pyrochlore phase domains. Both, the extent of ordering as well as distribution of ordered domains increases with Nd^{3+}content, which result into systematic evolution of Raman spectra corresponding to pyrochlores. For 50 mol% $NdO_{1.5}$ composition that exactly corresponds to $Nd_2Zr_2O_7$ pyrochlore, Raman spectrum shows intense bands (299, 395 and 503 cm^{-1}) for an ordered pyrochlore structure [100-102].

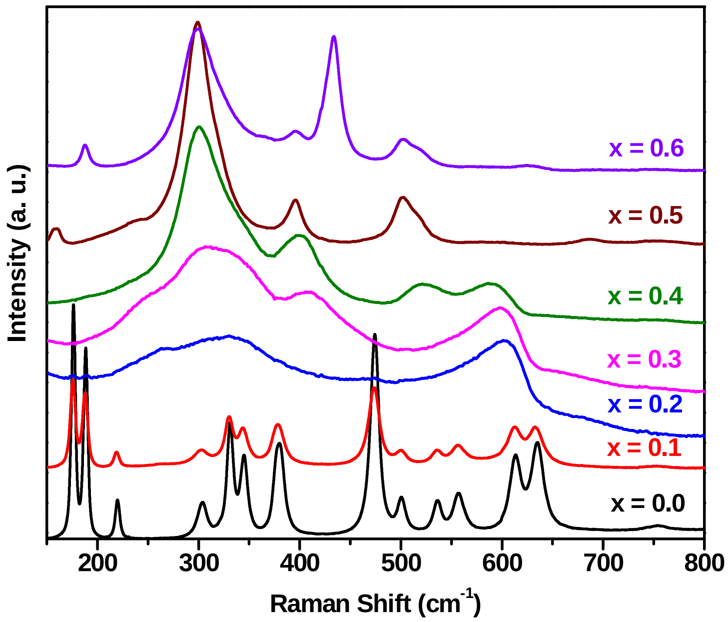

Fig. 3.3: Raman spectra of sintered $Zr_{1-x}Nd_XO_{2-x/2}$ ($0.0 \le x \le 0.6$) samples

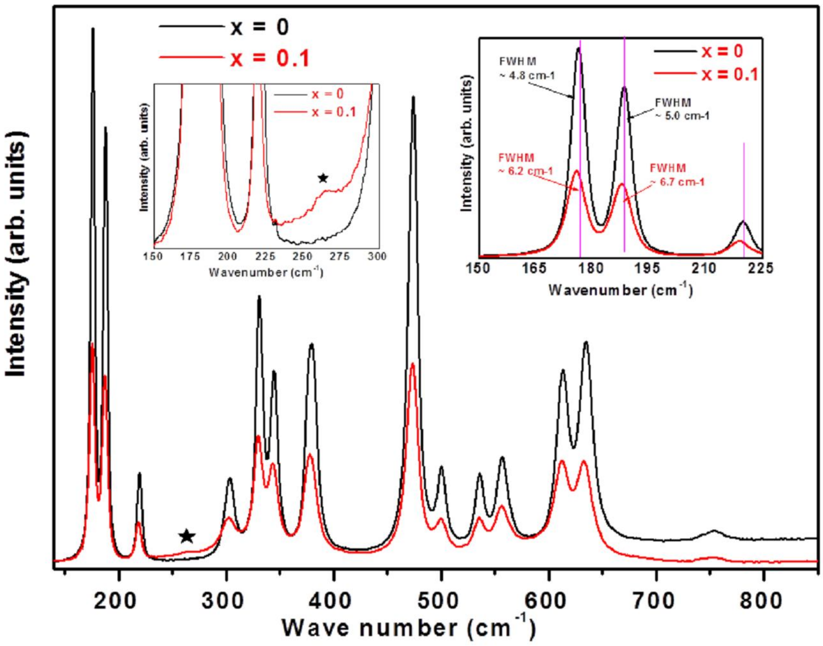

Fig. 3.4: Comparison of Raman spectra of pure m-ZrO_2 ($x = 0.0$) and 10 mol% $NdO_{1.5}$ doped ZrO_2 ($x = 0.1$)

Two additional weak bands (~ 160 cm^{-1} and ~ 700 cm^{-1}) observed in this composition are reported previously for ordered pyrochlores and attributed to combination/overtone bands [103]. Further incorporation of Nd^{3+} (x = 0.6 and higher) results into phase separation of Nd_2O_3-rich phase as revealed from Raman bands at 188 and 433 cm^{-1} (Fig. 3.3) corresponding to hexagonal Nd_2O_3 [104] in addition to pyrochlore Raman bands.

In summary, XRD and Raman studies confirm that with increasing value of ‘x’, $Zr_{1-x}Nd_xO_{2-x/2}$ system evolves swiftly from monoclinic ZrO_2 (x = 0.0) to a mixture of disordered monoclinic ZrO_2 + stabilized zirconia (x = 0.1) followed by single-phasic cubic stabilized zirconia (x = 0.2) and finally towards ordered pyrochlore phase (x = 0.3, 0.4 and 0.5). The system becomes biphasic (pyrochlore + hexagonal Nd_2O_3) for higher Nd^{3+} contents (x ≥ 0.6). These studies indicate that minor actinides in trivalent state form the cubic phase field (fluorite/pyrochlore) with ZrO_2 if present in 20-50 mol% range. It may be noted that formation of americium pyrochlore ($Am_2Zr_2O_7$) has been reported in the literature [105, 106]. It was also reported that the americium content in pure $Am_2Zr_2O_7$ is too high for either transmutation or conditioning purposes. Consequently, research has been directed to rare earth based pyrochlore (like $Nd_2Zr_2O_7$) as a host matrix wherein Pu and MA could be substituted for transmutation purposes [107].

3.3.1.3. Morphology and compositional analysis by SEM and EDS studies

Fig. 3.5(a) and (b) show representative secondary electron micrographs recorded on 10 and 20 mol% $NdO_{1.5}$ doped samples, respectively. Crystalline grain morphology with distribution of neck connected grains is amply visible in these micrographs. Morphology does not indicate any apparent multiphasic nature. 10 mol% $NdO_{1.5}$ doped sample shows distribution of smaller (sub-micron sized) grains over the bulk microstructure, which is not seen for 20 mol% $NdO_{1.5}$ doped composition. Reasonable open porosity can also be seen in these micrographs.

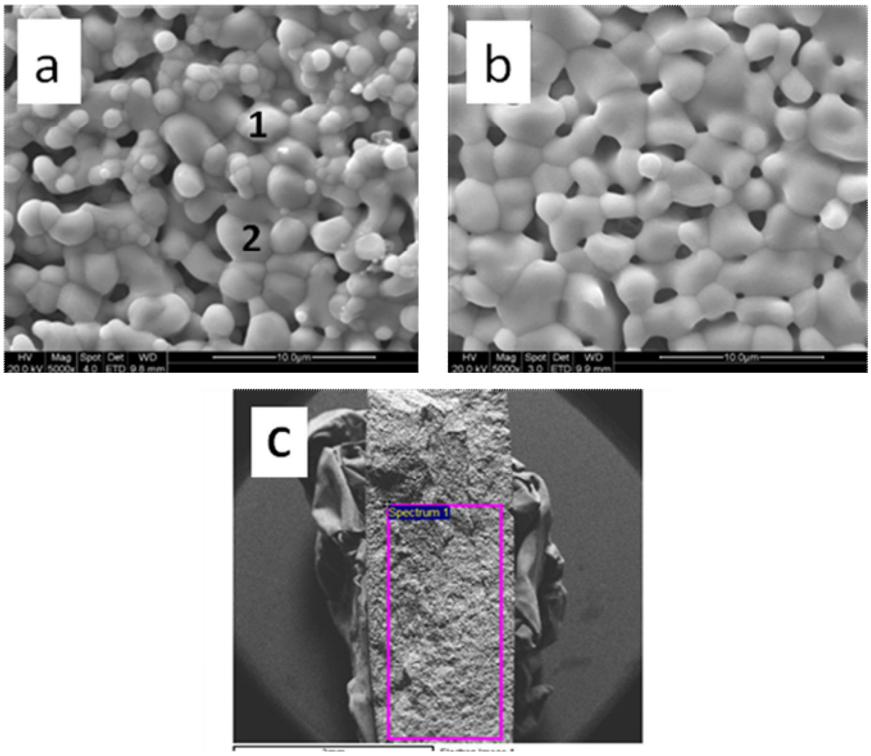

Fig. 3.5: SEM micrograph of (a) 10 mol% $NdO_{1.5}$ doped zirconia ($Zr_{0.90}Nd_{0.10}O_{1.95}$), (b) 20 mol% $NdO_{1.5}$ doped zirconia ($Zr_{0.80}Nd_{0.20}O_{1.90}$) and (c) fractured surface of $Zr_{0.80}Nd_{0.20}O_{1.90}$

Table 3.2: Composition of sintered $Zr_{1-x}Nd_xO_{2-x/2}$ samples (x = 0.1, 0.2, 0.3, 0.5)

Composition	**Zr (atom %)**	**Nd (atom %)**
$Zr_{0.90}Nd_{0.10}O_{1.95}$	98 (spot-1) 78 (spot-2) 91 (overall)	2 (spot-1) 22 (spot-2) 9 (overall)
$Zr_{0.80}Nd_{0.20}O_{1.90}$	78 (overall)	22 (overall)
$Zr_{0.70}Nd_{0.30}O_{1.85}$	67 (overall)	33 (overall)
$Zr_{0.50}Nd_{0.50}O_{1.75}$	48 (overall)	52 (overall)

Average composition of four samples (x = 0.1, 0.2, 0.3 and 0.5) have been measured by EDS technique and results are presented in Table 3.2. These results are in good agreement with the nominal compositions taken for combustion synthesis. However, in case of 10 mol% $NdO_{1.5}$ doped sample, average compositions varied from grain to grain. The composition at spot 1 and 2 in Fig. 3.5(a) were found to be Zr:Nd = 0.98:0.02 (2 mol% Nd^{3+}doped zirconia) and 0.78:0.22 (22 mol% Nd^{3+}doped zirconia). Such observation is consistent with results obtained from XRD and Raman studies which indicate biphasic behaviour of the compound consisting of stabilized zirconia and Nd^{3+}-doped m-ZrO_2 phase. In order to confirm that the composition is homogeneous throughout the bulk of pellet as well, the SEM and EDS are recorded on the cross section of fractured surface of the pellet for the composition $Zr_{0.80}Nd_{0.20}O_{1.90}$ (Fig. 3.5 (c)). The observed value is found to be in excellent agreement with the values obtained from EDS analysis on the pellet surface.

3.3.2. Thermo-physical characterization

Investigation of thermo-physical properties, such as thermal expansion and thermal conductivity are essential requirements to qualify a material for inert matrix fuel applications. With this objective, thermal expansion (lattice as well as bulk expansion) and thermal conductivity of selected compositions in $Zr_{1-x}Nd_xO_{2-x/2}$ series (0.2 ≤ x ≤ 0.5) have been studied. Results are presented in the subsequent section.

3.3.2.1. Thermal expansion studies

To measure lattice and bulk thermal expansion, both high temperature X-ray diffraction (HT-XRD) and high temperature dilatometry have been used, respectively. In HT-XRD studies, diffraction patterns are recorded at various temperatures and cell parameters of dominant phase are determined. These results are given in Table 3.3 for three $Zr_{1-x}Nd_xO_{2-x/2}$ compositions (x = 0.2, 0.3, 0.5). The first two compositions are refined with stabilized cubic zirconia as the model while the third one is refined upon ordered pyrochlore lattice.

Table 3.3: Lattice parameters at different temperatures for $Zr_{1-x}Nd_xO_{2-x/2}$ (x = 0.2, 0.3 and 0.5) samples

Temp (K)	Lattice parameter(a/Å)		
	$Zr_{0.80}Nd_{0.20}O_{1.90}$	$Zr_{0.70}Nd_{0.30}O_{1.85}$	$Zr_{0.50}Nd_{0.50}O_{1.75}$
RT	5.2018(2)	5.2447(3)	10.6938(8)
373	5.2053(6)	5.2473(8)	10.702(1)
473	5.2095(7)	5.2523(3)	10.709(1)
573	5.2142(5)	5.2567(6)	10.718(1)
673	5.2197(6)	5.2625(5)	10.727(2)
773	5.2266(4)	5.2670(8)	10.738(1)
873	5.2313(4)	5.2770(5)	10.748(1)
973	5.2375(4)	5.2787(8)	10.762(2)
1073	5.2434(7)	5.285(1)	10.774(1)
1173	5.2502(7)	5.291(1)	10.7851(9)
1273	5.260(2)	5.300(2)	10.805(3)

Table 3.4: Average lattice and bulk thermal expansion coefficients for $Zr_{1-x}Nd_xO_{2-x/2}$ (x = 0.2, 0.3, 0.5) samples

Composition	HT XRD $\alpha_a \times 10^6$ (K^{-1}) (RT–1273K)	Dilatometry $\alpha_L \times 10^6$ (K^{-1}) (RT–1273K)
$Zr_{0.80}Nd_{0.20}O_{1.90}$	11.2	11.0
$Zr_{0.70}Nd_{0.30}O_{1.85}$	10.6	10.4
$Zr_{0.50}Nd_{0.50}O_{1.75}$	10.3	10.2

Temperature dependence of lattice parameters (a_T) are evaluated as second order polynomials using least-square regression analysis. Resultant expressions are given as equation (3.1), (3.2) and (3.3).

$Zr_{0.80}Nd_{0.20}O_{1.90}$

$$a_T\ (\text{Å}) = 5.1916 + 2.9398 \times 10^{-5}\ T + 1.8350 \times 10^{-8}\ T^2 \qquad (3.1)$$

$Zr_{0.70}Nd_{0.30}O_{1.85}$

$$a_T\ (\text{Å}) = 5.2357+ 2.5212 \times 10^{-5}\ T + 1.9349 \times 10^{-8}\ T^2 \qquad (3.2)$$

$Zr_{0.50}Nd_{0.50}O_{1.75}$

$$a_T\ (\text{Å}) = 10.6786 + 4.3443 \times 10^{-5}\ T + 4.2468 \times 10^{-8}\ T^2 \qquad (3.3)$$

Percentage lattice thermal expansion is evaluated from temperature dependence of lattice parameter using the relation 2.2. These results are shown graphically in Fig. 3.6. The average coefficients of lattice thermal expansion (α_a) are calculated (RT−1273 K) using equation 2.3 and are presented in Table 3.4. On the other hand, bulk linear thermal expansion is measured over the temperature range from RT−1673 K. The percentage linear dilation (% ΔL/L) of $Zr_{1-x}Nd_xO_{2-x/2}$ (x = 0.2, 0.3, 0.5) compositions are shown in Fig. 3.7. The observed linear thermal expansions (%) are also fitted to the function of temperature using a second order polynomial regression. The results are as follows (T in K, in the range 300–1673 K).

$Zr_{0.80}Nd_{0.20}O_{1.90}$

$$\%\ \Delta L/L = -\ 0.28073 + 8.65087 \times 10^{-4}\ T + 1.54819 \times 10^{-7}\ T^2 \qquad (3.4)$$

$Zr_{0.70}Nd_{0.30}O_{1.85}$

$$\%\ \Delta L/L = -\ 0.2581 + 7.52862 \times 10^{-4}\ T + 1.94561 \times 10^{-7}\ T^2 \qquad (3.5)$$

$Zr_{0.50}Nd_{0.50}O_{1.75}$

$$\%\ \Delta L/L = -\ 0.34862 + 0.00108 \times T - 1.73946 \times 10^{-8}\ T^2 \qquad (3.6)$$

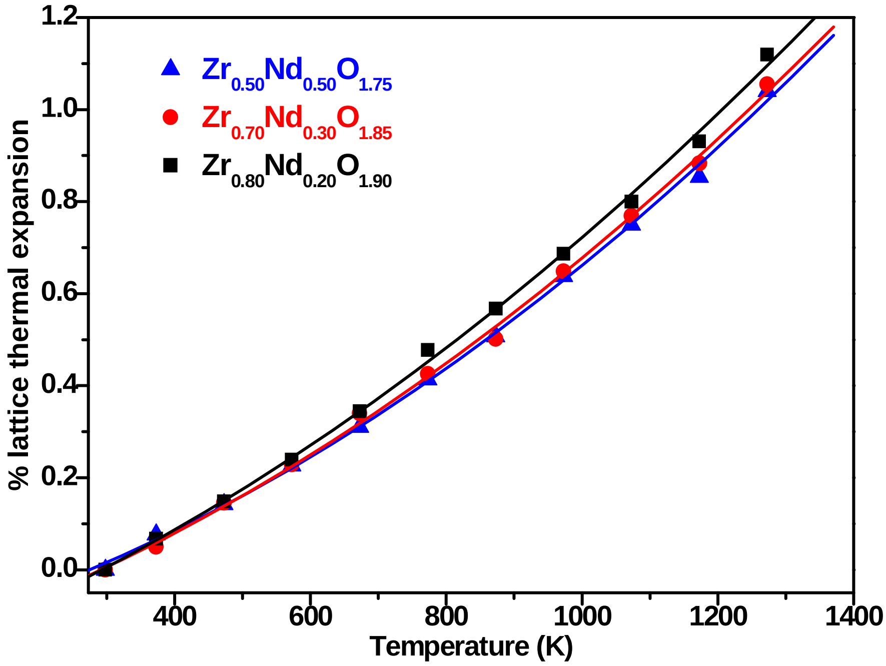

Fig. 3.6: Lattice thermal expansion (%) as a function of temperature

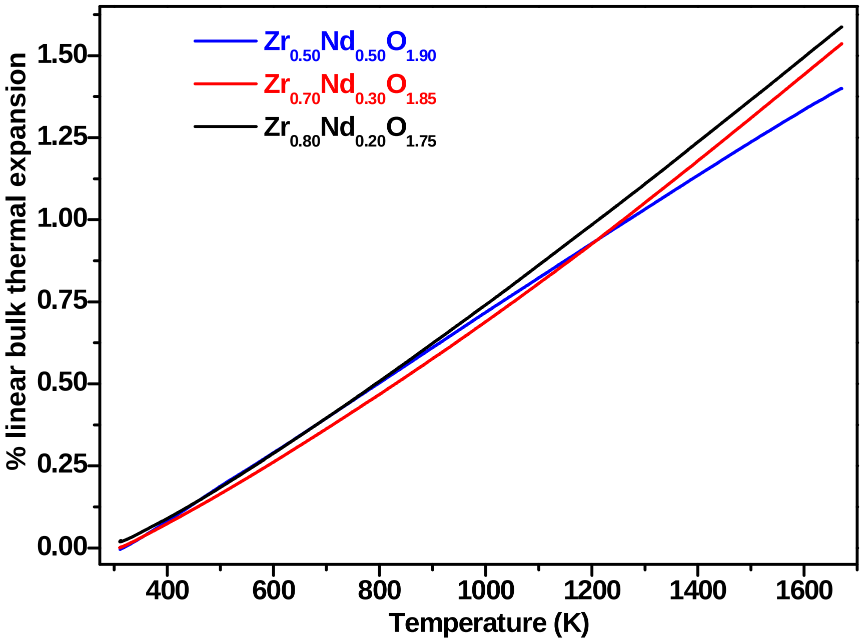

Fig. 3.7: Linear bulk thermal expansion (%) as a function of temperature

Average coefficients of bulk linear thermal expansion (α_L) are calculated (RT–1273 K) using the equation 2.4 and are tabulated along with the average lattice thermal expansion coefficients in Table 3.4. From the Table, it is obvious that both lattice CTE (α_a) and bulk linear CTE (α_L) decrease with increasing Nd^{3+} content in $Zr_{1-x}Nd_xO_{2-x/2}$ (x = 0.2, 0.3, 0.5) system. Relatively lower value of bulk CTE (α_L) as compared to lattice CTE (α_a) for any given composition could be attributed to the presence of porosity in bulk samples used for dilatometry. Samples used for dilatometry are sintered at 1723 K and has density ~ 85–88% of theoretical density. The residual porosity (~ 10–12%) therefore is expected to mask thermal expansion to some extent leading to relatively lower bulk thermal expansion coefficients. Similar effect is not seen in HT-XRD measurements as lattice thermal expansion is insensitive to specimen porosity.

The incorporation of Nd^{3+} in $Zr_{1-x}Nd_xO_{2-x/2}$ series leads to increase in order of the system. It has been reported that increase in order leads to increase in lattice energy which results in the decrease in thermal expansion coefficient [108-110]. In the present system, increase in Nd^{3+}-content leads to gradual increase in ordering and decrease in thermal expansion coefficient which is in accordance with the observation made in the above mentioned studies. Further, it may be noted that due to increase in pyrochlore-type ordering, the co-ordination number of Zr decreases from 7-8 in defect fluorite structure (z/r for Zr 4.762) to 6 in pyrochlore (z/r = 5.56). This manifests in increase in average bond strength which results in decreased thermal expansion on increasing Nd^{3+}-content. The presence of increased content of vacancies (upon Nd^{3+}-introduction) also aids in masking the thermal expansion, thus leading to decrease in thermal expansion on successive Nd^{3+}-substitution.

The thermal expansion behaviour is also influenced by the melting point of the constituent oxides [111]. It is interesting to mention that $Th_{1-x}Nd_xO_{2-x/2}$ system (where tetravalent Th^{4+} is replaced by trivalent Nd^{3+}) which is similar to the present system but the thermal expansion behaviour depicted by ThO_2-based system is opposite to that exhibited by present system [112]. It can be explained as follows. The thermal expansion behaviour of such a system is influenced by the melting points of the constituent oxide and the presence of vacancies. Increase of higher melting point component increases average bond strength which decreases thermal expansion and presence of vacancies mask the thermal expansion. In $Th_{1-x}Nd_xO_{2-x/2}$ system, melting points of ThO_2 and Nd_2O_3 are 3663 K and 2545 K, respectively. So, even though increase of Nd^{3+} introduces vacancies which should hinder thermal expansion, much lower melting point of Nd_2O_3 dominates over the vacancy effect and the thermal expansion of $Th_{1-x}Nd_xO_{2-x/2}$ series shows an increase in thermal expansion coefficient with increase in Nd-content. Even though the melting point of ZrO_2 (2950 K) is higher than Nd_2O_3, the difference is much smaller and in ZrO_2-based system, the effect of vacancies predominates over relative melting points and the system exhibits a decrease in thermal expansion coefficient with increase in Nd^{3+}-content. Further, there is no ordering observed in ThO_2 based system which also contributes to different thermal expansion trends exhibited by the two systems. Chavan et al. [113] investigated thermal expansion in $Ce_{1-x}Nd_xO_{2-x/2}$ ($0.2 \leq x \leq 0.5$) system and they also observed decrease in thermal expansion coefficient with increasing Nd^{3+} content similar to our study.

3.3.2.2. Thermal conductivity

Thermal conductivity has been measured for the representative composition $Zr_{0.80}Nd_{0.20}O_{1.90}$. Fig. 3.8 shows variation in thermal diffusivity with temperature, as measured by laser flash technique. The diffusivity values are arithmetic mean of four laser shots at each temperature. A gradual decrease in diffusivity is typical signature of dielectric oxides where heat transport is mainly governed by phonon-phonon and lattice-phonon interactions. Thermal conductivity is calculated using measured thermal diffusivity, density and specific heat with the help of equation 2.9.

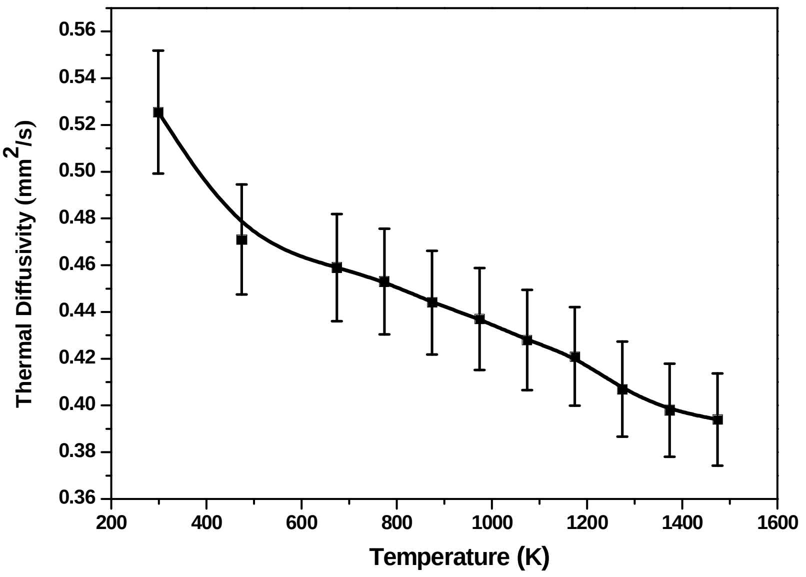

Fig. 3.8: Thermal diffusivity of $Zr_{0.80}Nd_{0.20}O_{1.90}$ as a function of temperature

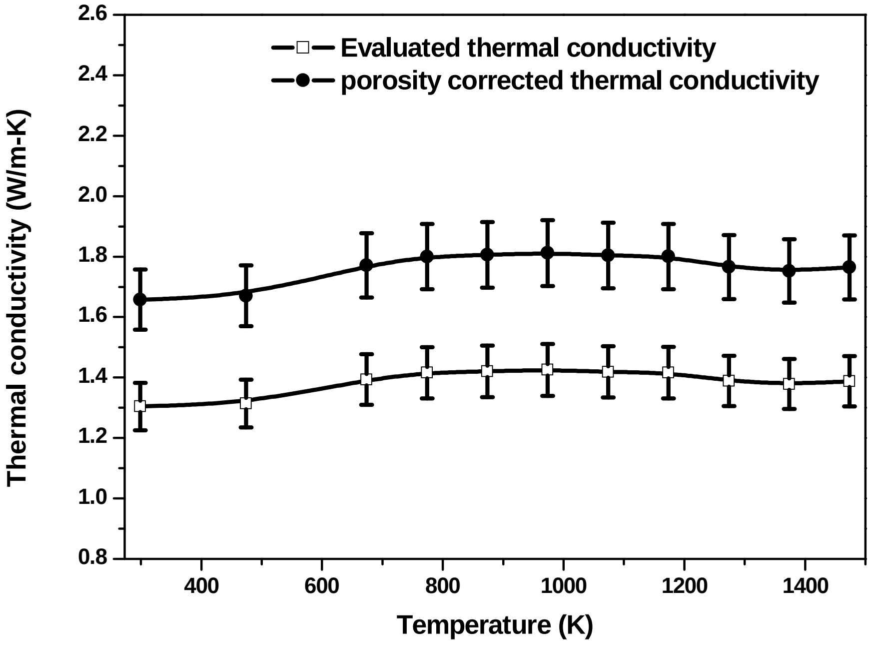

Fig. 3.9: Thermal conductivity of $Zr_{0.80}Nd_{0.20}O_{1.90}$ sample as a function of temperature; as measured conductivity and porosity corrected values are shown

Temperature dependence density is obtained from bulk thermal expansion data while specific heat is taken from literature [88]. Fig. 3.9 shows the thermal conductivity variation as a function of temperature for $Zr_{0.80}Nd_{0.20}O_{1.90}$ sample with 84% of theoretical density (TD). The thermal conductivity remains nearly constant (1.3–1.4 $Wm^{-1}K^{-1}$) over the studied temperature range. Since the sintered specimen is not fully (100% of TD) dense, the evaluated thermal conductivity data 'λ_m' has been corrected for porosity to estimate the thermal conductivity of fully dense material 'λ_{100}' by using the equation 2.10. The conductivity values estimated for nearly fully dense materials are also shown in Fig. 3.9. The thermal conductivity is found to remain nearly constant (1.6–1.80 $Wm^{-1}K^{-1}$) over the studied temperature range. The results match reasonably well with literature reported results on similar composition [88]. It must be noted that thermal conductivity of pure ZrO_2 was reported to be ~ 7.0 $Wm^{-1}K^{-1}$ at room temperature. Low thermal conductivity in this system can be attributed to large variation in ionic radius and mass of Zr^{4+} and Nd^{3+} ions, presence of extensive disorder in cation/anion sub-lattices, presence of oxygen ion vacancies, etc. All these structural features act as phonon scattering centres in these oxides and thereby lower the thermal conductivity. It can also be seen that evaluated conductivity values are quite lower as compared to typical oxide nuclear fuel such as UO_2 (~ 10 $Wm^{-1}K^{-1}$ at RT; ~ 2.5 $Wm^{-1}K^{-1}$ at 1500 K). This indicates a need in improving the thermal conductivity of such materials for their application as inert matrix fuels for MA transmutation.

3.4. Conclusion

Phase behaviour of ZrO_2-$NdO_{1.5}$ binary system has been established with the help of XRD and Raman studies. Four distinct phases, namely monoclininc ZrO_2, Nd-stabilized zirconia (defect fluorite), ordered pyrochlore, hexagonal Nd_2O_3 have been identified. Biphasic mixtures of (1) Nd-stabilized zirconia (defect fluorite) + monoclinic ZrO_2 phase, (2) pyrochlore and Nd-stabilized zirconia and (3) pyrochlore and hexagonal Nd_2O_3 phase are observed. Around 20 mol% $NdO_{1.5}$ is identified as minimum substitution required for stabilizing zirconia in cubic phase. A maximum of 50 mol% $NdO_{1.5}$ can be incorporated in ZrO_2 maintaining single phase cubic structure. This information would be useful for incorporation of minor actinides in ZrO_2-based matrices to develop novel transmutation matrices. Both high temperature XRD and dilatometry results show a marked distinction in thermal expansion behavior of $Zr_{1-x}Nd_xO_{2-x/2}$ system ($0.2 \leq x \leq 0.5$) where structural order brings in enhanced lattice stability and hence a net reduction in thermal expansivity with increasing Nd^{3+} content. Lower thermal conductivity of Nd^{3+} stabilized cubic zirconia ($Zr_{0.80}Nd_{0.20}O_{1.90}$) sample is attributed to large variation in ionic radius and mass of Zr^{4+} and Nd^{3+} ions and presence of oxygen ion vacancies. The thermal conductivity study also indicates the need for improvement in matrix design for nuclear fuel application.

CHAPTER 4

Investigation of phase relations and thermal properties in $Zr_{0.70}[Y_{1-x}Nd_x]_{0.30}O_{1.85}$ $(0.0 \leq x \leq 1.0)$ system

4.1. Introduction

Phase relations in ZrO_2–$NdO_{1.5}$ system have already been discussed in chapter 3. It is observed that approximately a minimum substitution of 20 mol% $NdO_{1.5}$ is required for stabilizing ZrO_2 in cubic phase and a maximum of 50 mol% $NdO_{1.5}$ can be incorporated in ZrO_2 maintaining single phase cubic structure. However, incorporation of 10 mol% $NdO_{1.5}$ in ZrO_2 leads to a biphasic mixture consisting of monoclinic zirconia (m-ZrO_2) and Nd-stabilized cubic zirconia. Thus, to avoid the formation of biphasic phase-field at lower Nd^{3+} (< 20 mol %) incorporation level, a neutron transparent trivalent cation (Y^{3+}) which also stabilizes ZrO_2 in cubic phase can be co-doped with Nd^{3+} in appropriate mole fraction. Consequently, $Zr_{0.70}[Y_{1-x}Nd_x]_{0.30}O_{1.85}$ $(0.0 \leq x \leq 1.0)$ system has been investigated for phase relation and thermo-physical properties and discussed in this chapter. It must be mentioned that Nd_2O_3 has been used here as non-radioactive surrogate for minor actinides and Y^{3+} doped ZrO_2 as inert matrix component.

4.2. Experimental

All samples have been prepared by conventional solid-state synthesis route. Stoichiometric amounts of the reactants (viz. ZrO_2, Y_2O_3 and Nd_2O_3) required for various nominal compositions in $Zr_{0.70}[Y_{1-x}Nd_x]_{0.30}O_{1.85}$ $(0.0 \leq x \leq 1.0)$ system have been mixed, pelletized and heated at 1673 K (48 h) and 1873 K (24 h) each. All the heatings have been performed in static air and the heating as well as cooling rates are maintained at 5 K/min. The sintered samples have been thoroughly characterized by XRD, Raman spectroscopy, SEM and EDS. The bulk thermal expansion of few selected compositions has been measured over the temperature range 298–1473 K using dilatometer.

Heat capacity of sintered samples has been measured by heat flux-type DSC over the temperature range 313–713 K. The thermal conductivity has been measured for the end members, Y^{3+} and Nd^{3+}-stabilized ZrO_2 over the temperature range 298–1373 K.

4.3. Results and discussion

4.3.1. Structural characterization

4.3.1.1. X-ray diffraction studies

The XRD patterns of the reactants and the products obtained in $Zr_{0.70}[Y_{1-x}Nd_x]_{0.30}O_{1.85}$ ($0.0 \leq x \leq 1.0$) series are recorded and analyzed. The reactant ZrO_2 is monoclinic (space group $P2_1/c$), whereas Nd_2O_3 and Y_2O_3 exhibit hexagonal (space group P-3m1) and C-type cubic crystal structures (space group Ia-3), respectively. The XRD patterns for various nominal compositions in this particular series are shown in Fig. 4.1. The XRD pattern for the composition $Zr_{0.70}Y_{030}O_{1.85}$ ($x = 0.0$) shows the presence of fluorite-type (F-type) cubic phase. The diffraction pattern remains same with increasing the x value from $x = 0.0$ to $x = 1.0$. Thus, the XRD studies imply that the entire series crystallizes in single-phasic F-type lattice. However, Hayes et al. [114] could observe monoclinic and tetragonal phase of ZrO_2 as well along with F-type cubic phase for the composition $Zr_{0.75}Nd_{0.25}O_{1.88}$ after annealing the sample at 1673 K. They have also showed that the cubic fluorite structure can be stabilized by the addition of a small amount of Y^{3+} to the $Zr_{1-x}Nd_xO_{2-x/2}$ system. The XRD pattern for the composition $Zr_{0.70}Nd_{0.30}O_{1.85}$ ($x = 1.0$) is presented separately in the Fig. 4.2 for better clarity. The diffraction pattern clearly indicates the presence of F-type Nd^{3+}-stabilized cubic ZrO_2 along with some impurity peaks marked by asterisk (*). One of the impurities could plausibly be m-Nd_2O_3 [JCPDS Card No: 28-0671]. In 3rd chapter, phase relation in ZrO_2–$NdO_{1.5}$ system [115] prepared by gel combustion route has been discussed where $Zr_{0.70}Nd_{0.30}O_{1.85}$ is observed to exist in F-type cubic lattice with weak reflections corresponding to pyrochlore phase.

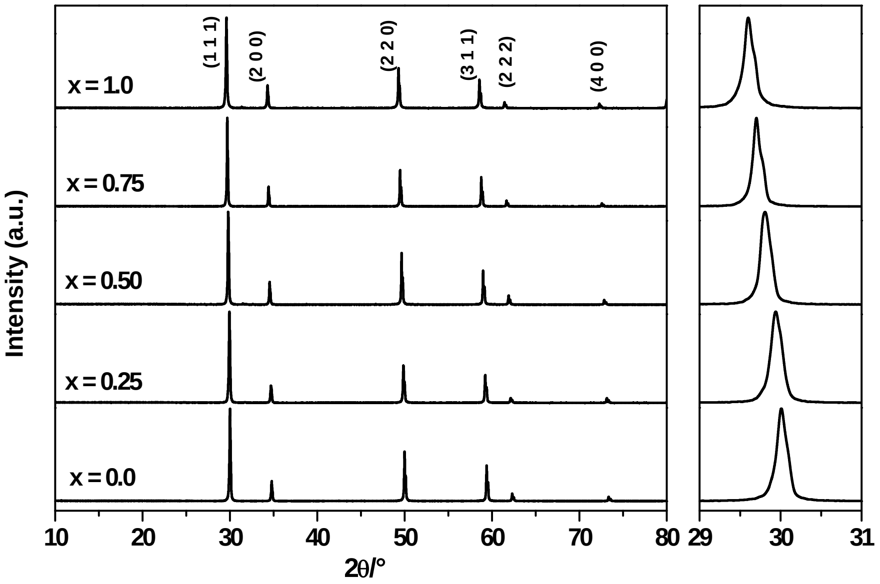

Fig. 4.1: XRD patterns of sintered $Zr_{0.70}[Y_{1-x}Nd_x]_{0.30}O_{1.85}$ (0.0 ≤ x ≤ 1.0) samples

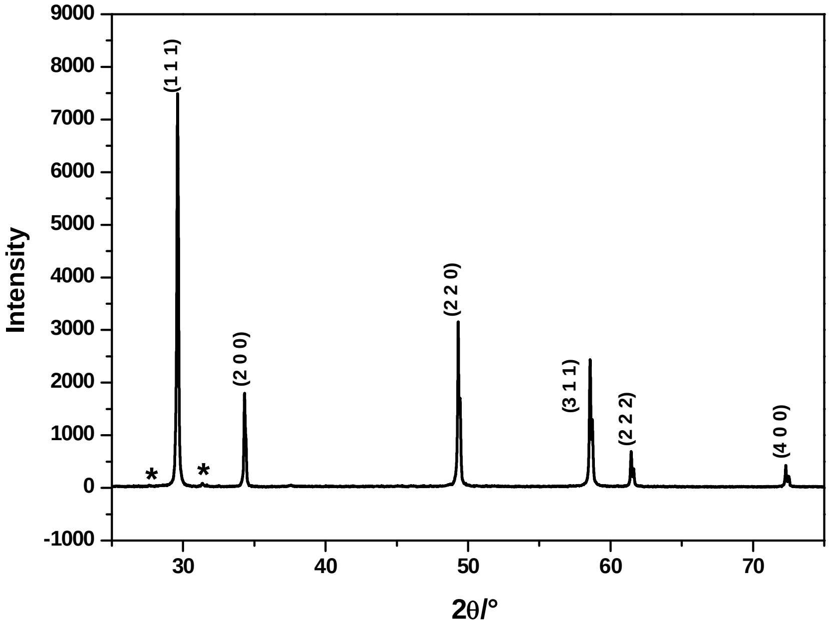

Fig. 4.2: XRD patterns of sintered $Zr_{0.70}Nd_{0.30}O_{1.85}$ (x = 1.0) sample

The same composition is prepared by solid state synthesis in the present study. This shows how the preparative method and sintering temperature may bring about subtle change in phase relation especially when closely related polymorphs are expected.

Increase in $NdO_{1.5}$-content shifts the XRD pattern in consecutive nominal composition towards lower angle indicating dilation of fluorite-type cubic phase. The substitution of smaller size Y^{3+} by relatively larger Nd^{3+} (ionic radii of Nd^{3+} and Y^{3+}, in eight-fold coordination, are 1.109 and 1.019 Å, respectively [64]) increases effective cationic size leading to increase in lattice parameter. The XRD patterns for all the phases have been refined using POWDERX and their cell parameters have been determined. Table 4.1 enlists the phases observed along with the lattice parameter values. Fig. 4.3 depicts an almost ideal Vegard's law type of behaviour for the variation of cell parameter with composition, indicating that the lattice parameters are governed primarily by relative ionic radii of the host and guest cation.

4.3.1.2. Raman spectroscopic studies

Raman studies have been carried out on sintered samples to obtain further understanding of structural variation in $Zr_{0.70}[Y_{1-x}Nd_x]_{0.30}O_{1.85}$ ($0.0 \le x \le 1.0$) system. Fig. 4.4 depicts as recorded Raman spectra of sintered samples. The Raman spectrum for the sample $Zr_{0.70}Y_{0.30}O_{1.85}$ (x = 0.0) exhibits three broad bands in the energy range 200 to 800 cm^{-1}. Similar type of Raman bands have been observed for different stabilized disordered cubic zirconia phases reported in literature [116]. Yashima et al. [117, 118] observed a similar Raman spectrum for Y^{3+} and rare-earth substituted cubic zirconia. Thus, $Zr_{0.70}Y_{0.30}O_{1.85}$ (x = 0.0) can be identified to be disordered cubic phase. It may be noted that an ideal fluorite-type cubic structure is expected to exhibit only a single Raman active mode as determined by factor group analysis [119]. The appearance of many broad Raman bands for the stabilized zirconia is attributed to its highly defective/disordered structure as discussed in Chapter 3.

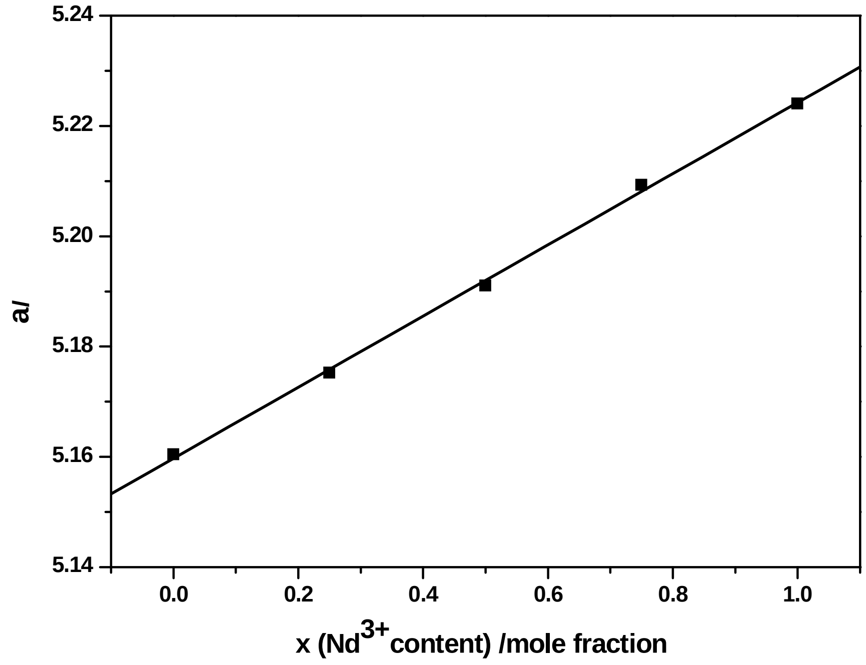

Fig. 4.3: Variation of lattice parameter as a function of $NdO_{1.5}$ mole fraction in $Zr_{0.70}[Y_{1-x}Nd_x]_{0.30}O_{1.85}$ ($0.0 \le x \le 1.0$) samples

Table 4.1: Phases present in various $Zr_{0.70}[Y_{1-x}Nd_x]_{0.30}O_{1.85}$ ($0.0 \le x \le 1.0$) compositions and their lattice parameter

Composition	**Phases identified by XRD**	**Lattice parameter (Å)**
$Zr_{0.70}Y_{0.30}O_{1.85}$	Stabilized zirconia (defect fluorite)	5.1604 (6)
$Zr_{0.70}Y_{0.225}Nd_{0.075}O_{1.85}$	Stabilized zirconia (defect fluorite)	5.1752 (8)
$Zr_{0.70}Y_{0.15}Nd_{0.15}O_{1.85}$	Stabilized zirconia (defect fluorite)	5.1910 (4)
$Zr_{0.70}Y_{0.075}Nd_{0.225}O_{1.85}$	Stabilized zirconia (defect fluorite)	5.2093 (9)
$Zr_{0.70}Nd_{0.30}O_{1.85}$	Stabilized zirconia (defect fluorite)	5.2240 (3)

The $NdO_{1.5}$ substitution into $Zr_{0.70}Y_{0.30}O_{1.85}$ yields similar Raman spectra till the composition $Zr_{0.70}Y_{0.15}Nd_{0.15}O_{1.85}$ (x = 0.50) indicating the presence of similar type of structure in these nominal compositions as well. However, an interesting observation is the relative increase in intensity of Raman band at 320 cm^{-1} with concomitant decrease in intensity of the band at 600 cm^{-1}. With still higher $NdO_{1.5}$ substitution, for the nominal composition $Zr_{0.70}Y_{0.075}Nd_{0.225}O_{1.85}$ (x = 0.75), a weak Raman band at 466 cm^{-1} (marked by asterisk in Fig. 4.4 (d)) in addition to existing Raman bands is found to appear. It has been reported [117, 118] that Raman band at around 470 cm^{-1} is characteristic of the tetragonal phase of zirconia. Thus, the presence of micro-domains of tetragonal phase in the F-type cubic phase for the

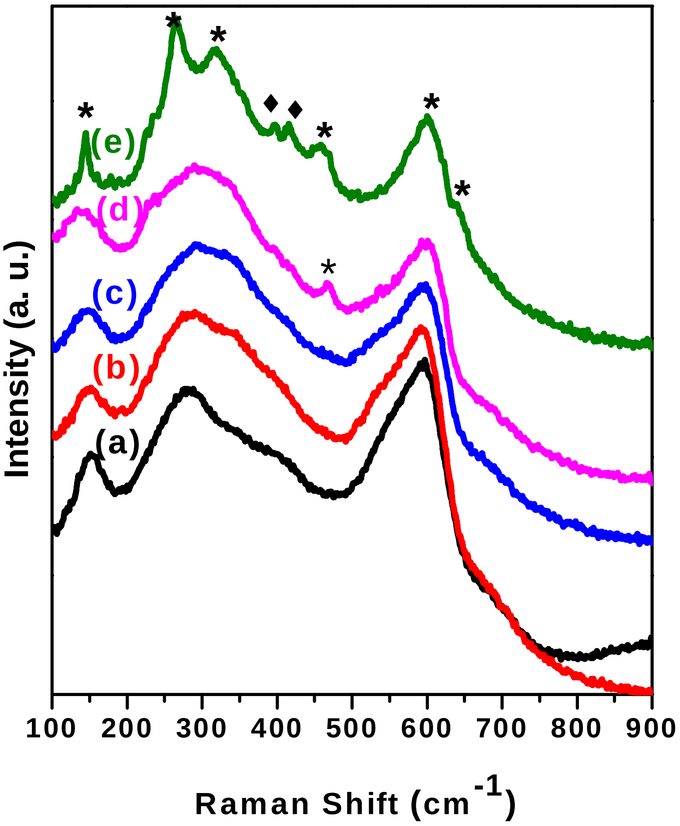

Fig. 4.4: Raman spectra of $Zr_{0.70}[Y_{1-x}Nd_x]_{0.30}O_{1.85}$ samples: (a) x = 0.0, (b) x = 0.25, (c) x = 0.50, (d) x = 0.75 and (e) x = 1.0

composition $Zr_{0.70}Y_{0.075}Nd_{0.225}O_{1.85}$ (x = 0.75) cannot be ruled out. Several distinct Raman bands are found to appear for the composition $Zr_{0.70}Nd_{0.30}O_{1.85}$ (x = 1.0). The six Raman bands (marked by asterisk) which are found to appear at 144, 266, 320, 460, 600 and 640 cm^{-1} are the characteristics of tetragonal phase [120] and the two additional bands (marked by ♦) at 398 and 417 cm^{-1} are the signature of monoclinic Nd_2O_3 phase (impurity phase) [121]. The Raman data indicates that the composition $Zr_{0.70}Nd_{0.30}O_{1.85}$ (x = 1.0) crystallizes as tetragonal phase. Since XRD results clearly dictate presence of F-type cubic phase, the nominal composition, $Zr_{0.70}Nd_{0.30}O_{1.85}$ (x = 1.0), may be treated as presence of domains of partially stabilized tetragonal zirconia in largely F-type cubic stabilized zirconia phase. It must be noted that the signature of (highly disordered) cubic zirconia could not be observed in the Raman spectrum in the presence of tetragonal phase. This is because the cubic stabilized zirconia has a highly defective structure and corresponding Raman spectrum would be broad with weak bands which are expected to be masked by bands for tetragonal zirconia. The cubic to tetragonal phase transition occurs through oxygen displacement along the c axis from the ideal fluorite site [117]. XRD is not sensitive to such an oxygen induced transition because of the small scattering factor of the oxygen atom. This could be the reason for non-corroboration of XRD and Raman results for this particular nominal composition. Thus, this highlights the necessity of complementary characterization obtained by XRD and Raman spectroscopy. The Raman spectroscopy is a simple and powerful tool to study the subtle structural change between the cubic and the tetragonal phase in stabilized zirconia systems. Also, pyrochlore micro-domains are found to exist in largely F-type lattice for the composition $Zr_{0.70}Nd_{0.30}O_{1.85}$ prepared by gel combustion route as discussed in chapter 3. The comparison of these results clearly indicates that the structure for the same nominal composition is highly dependent on the synthesis route and sintering conditions as well.

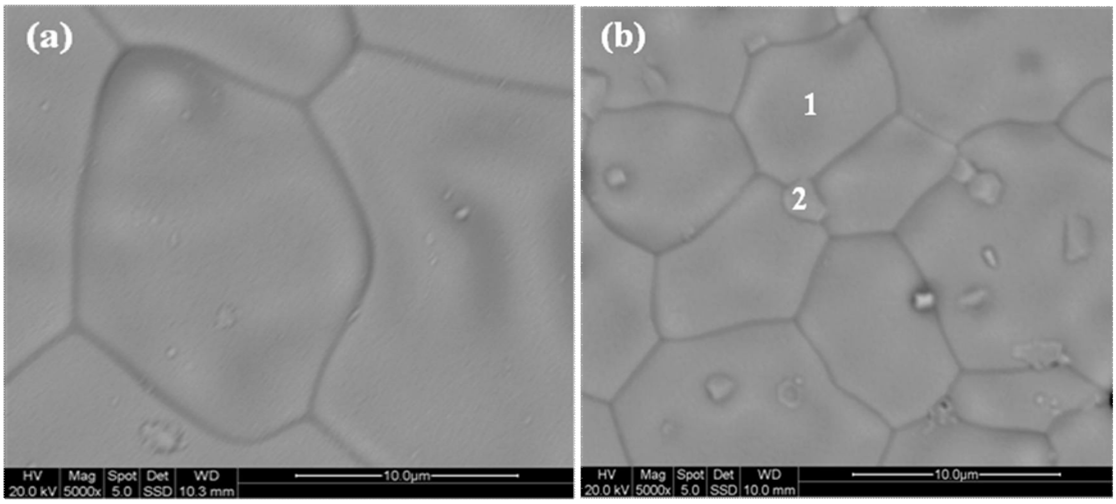

Fig. 4.5: SEM micrograph of sintered $Zr_{0.70}[Y_{1-x}Nd_x]_{0.30}O_{1.85}$ samples: (a) $x = 0.0$ and (b) $x = 1.0$

Table 4.2: Average composition of sintered $Zr_{0.70}[Y_{1-x}Nd_x]_{0.30}O_{1.85}$ samples (x = 0.0, 0.25, 0.50, 0.75 and 1.0); compositions at spot 1 and 2 (shown in Fig 4.5) were determined in EDS point acquisition mode

Composition	Zr (at. %)	Nd (at. %)	Y (at. %)
$Zr_{0.70}Y_{0.30}O_{1.85}$ (overall)	70	-	30
$Zr_{0.70}Y_{0.225}Nd_{0.075}O_{1.85}$ (overall)	70	6	24
$Zr_{0.70}Y_{0.15}Nd_{0.15}O_{1.85}$ (overall)	70	14	16
$Zr_{0.70}Y_{0.075}Nd_{0.225}O_{1.85}$ (overall)	71	9	21
$Zr_{0.70}Nd_{0.30}O_{1.85}$ (overall) (spot – 1) (spot – 2)	71 70 -	29 30 100	- - -

In summary, XRD and Raman studies confirm that the sample $Zr_{0.70}Y_{0.30}O_{1.85}$ (x = 0.0) exists as F-type cubic phase. Both the techniques also confirm that the same structure is retained up to the composition $Zr_{0.70}Y_{0.15}Nd_{0.15}O_{1.85}$ (x = 0.50) whereas $Zr_{0.70}Nd_{0.30}O_{1.85}$ (x = 1.0) consists of tetragonal zirconia-type domains in addition to fluorite-type cubic phase.

4.3.1.3. Morphology and compositional analysis by SEM and EDS studies

The secondary electron micrographs of $Zr_{0.70}[Y_{1-x}Nd_x]_{0.30}O_{1.85}$ (x= 0.0 and 1.0) samples are shown in Fig. 4.5(a) and (b), respectively. The average grain size of these materials is several micrometers. However, grain sizes differ from composition to composition. The average grain size for the sample $Zr_{0.70}Y_{0.30}O_{1.85}$ (x = 0.0) is found to be 18-25 μm while for $Zr_{0.70}Nd_{0.30}O_{1.85}$ (x = 1.0) sample it is 9-11 μm. Unreacted oxides are not found to exist in SEM micrographs of $Zr_{0.70}Y_{0.30}O_{1.85}$ (x = 0.0). However, unreacted Nd_2O_3 is found to exist in boundaries between grains for the composition $Zr_{0.70}Nd_{0.30}O_{1.85}$ (x = 1.0). Distinct open porosity can also be seen in low magnified micrographs. Average compositions have been estimated by EDS. Five compositions (x = 0.00, 0.25, 0.50, 0.75 and 1.00) have been analyzed and results are presented in Table 4.2. These results are in good agreement with the nominal compositions taken for solid state synthesis in all the cases. The composition at spot 1 and 2 in Fig. 4.5(b) were found to be Zr:Nd = 0.70:0.30 (30 mol% Nd^{3+}doped zirconia) and 0.00:1.00 (pure Nd_2O_3). The results indicate presence of unreacted Nd_2O_3 between grain boundaries for the composition $Zr_{0.70}Nd_{0.30}O_{1.85}$ (x = 1.0). The signature of the same is also detected by XRD and Raman spectroscopy.

4.3.2. Thermo-physical studies

The thermo-physical properties, namely, the bulk thermal expansion, heat capacity, and thermal conductivity of selected compositions in $Zr_{0.70}[Y_{1-x}Nd_x]_{0.30}O_{1.85}$ ($0.0 \leq x \leq 1.0$) system have been determined. The measurements have been carried out on dense samples.

Table 4.3: Density of sintered $Zr_{0.70}[Y_{1-x}Nd_x]_{0.30}O_{1.85}$ samples (x = 0.0, 0.5 and 1.0) employed for different studies

Sample	Experiment	Measured density (g/cc)	Theoretical density (g/cc)	% TD
$Zr_{0.70}Y_{0.30}O_{1.85}$	Dilatometry	5.36	5.81	92
	Thermal diffusivity	5.21	5.81	90
$Zr_{0.70}Y_{0.15}Nd_{0.15}O_{1.85}$	Dilatometry	5.43	6.10	89
$Zr_{0.70}Nd_{0.30}O_{1.85}$	Dilatometry	5.84	6.37	92
	Thermal diffusivity	5.64	6.37	89

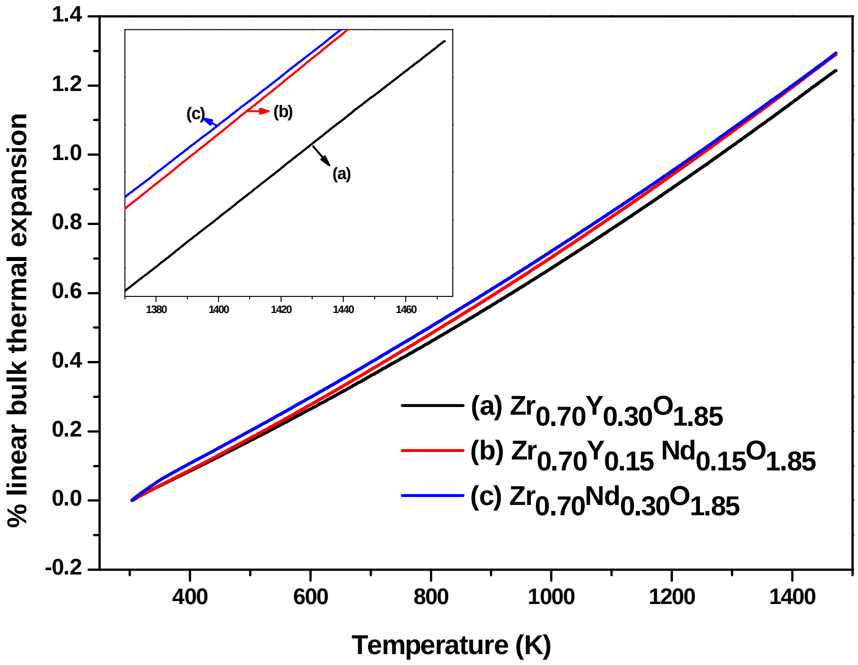

Fig. 4.6: Bulk thermal expansion (%) of $Zr_{0.70}[Y_{1-x}Nd_x]_{0.30}O_{1.85}$ samples (x = 0.0, 0.5 and 1.0) as a function of temperature

The relative densities of the $Zr_{0.70}[Y_{1-x}Nd_x]_{0.30}O_{1.85}$ ($0.0 \leq x \leq 1.0$) bulk materials are given in Table 4.3.

4.3.2.1. Thermal expansion studies

Bulk linear thermal expansion has been measured using a high temperature vertical dilatometer over the temperature range 300–1473 K. The percentage linear dilation of $Zr_{0.70}[Y_{1-x}Nd_x]_{0.30}O_{1.85}$ (x = 0.0, 0.5, 1.0) compositions are shown in Fig. 4.6. No phase transition was observed for the samples in this temperature range. The experimental percent linear thermal expansion ($100 \times \frac{\Delta L}{L}$) for each composition in the complete temperature range were best fitted to $A + BT + CT^2$ equation where, A, B, and C are the constants and T is absolute temperature. The values of these constants are given in Table 4.4. The average coefficients of linear thermal expansion (α_L) for the samples are calculated using equation 2.4 and are provided in Table 4.4. It was observed that 50 mol% substitution of Y^{3+} by Nd^{3+} in $Zr_{0.70}Y_{0.30}O_{1.85}$ to form $Zr_{0.70}Y_{0.15}Nd_{0.15}O_{1.85}$ (x = 0.50) leads to an increase in thermal expansion coefficient from 10.6×10^{-6} to 11.0×10^{-6}. However, the thermal expansion coefficient for $Zr_{0.70}Nd_{0.30}O_{1.85}$ sample matches with the thermal expansion coefficient of $Zr_{0.70}Y_{0.15}Nd_{0.15}O_{1.85}$ sample. The results have been explained as follows.

In any system, it is known that the thermal expansion is governed by two factors namely (a) the melting point of the constituents and (b) vacancies in the system. It has been stated by Uitert et al. [111] that other things being equal the melting point (M_P) is the good measure of binding energy and inverse measure of thermal expansion (α_L). Further, Uitert et al. have provided an empirical relation which states that the product $\alpha_L M_P$ is constant for a given structure. It must be noted that all the compositions in the given system exist in cubic-fluorite structure. Hence, in accordance with Uitert et al., it can be stated that in this system, solid with lower melting point will have higher thermal expansion. The incorporation of vacancies, on the other hand, is likely to mask thermal expansion.

Table 4.4: The coefficients of percent linear thermal expansion equation for the $Zr_{0.70}[Y_{1-x}Nd_x]_{0.30}O_{1.85}$ (x = 0.0, 0.5 and 1.0) compositions

Compositions	$100 \times \frac{\Delta L}{L} = A + BT + CT^2$ (RT–1473 K)			$\alpha_L \times 10^6$ (K^{-1})
	A	B x 10^4	C × 10^7	
$Zr_{0.70}Y_{0.30}O_{1.85}$	- 0.22632	6.91735	2.08131	10.6
$Zr_{0.70}Y_{0.15}Nd_{0.15}O_{1.85}$	- 0.24352	7.47397	1.99964	11.0
$Zr_{0.70}Nd_{0.30}O_{1.85}$	- 0.25813	8.39207	1.43009	11.0

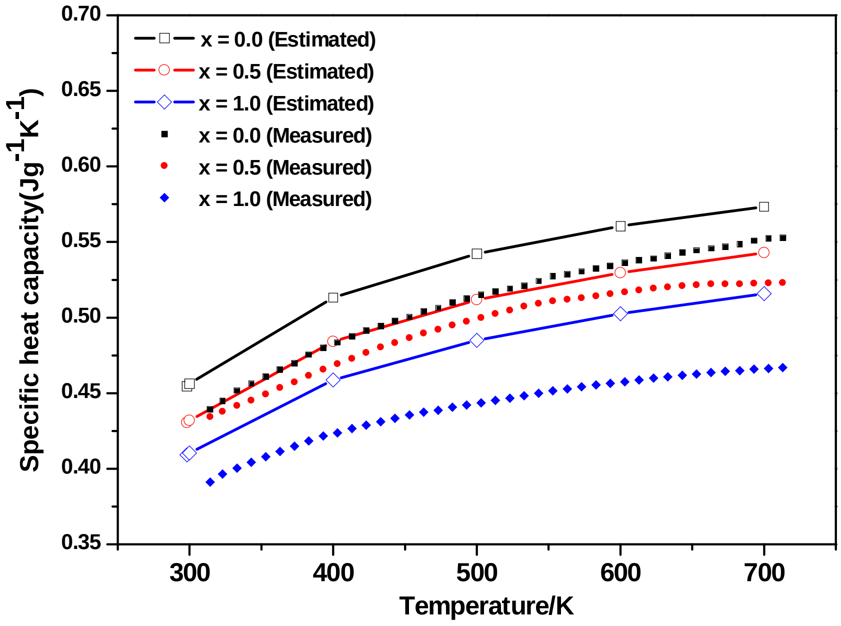

Fig. 4.7: Specific heat capacities as a function of temperature in $Zr_{0.70}[Y_{1-x}Nd_x]_{0.30}O_{1.85}$ (x = 0.0, 0.5 and 1.0) samples

In the present study, the concentration of vacancies is same in the entire composition range due to constant amount of trivalent cation content and it is expected that the melting points of the constituent oxides should govern the thermal expansion. Thus the relative melting points of yttrium oxide and neodymium oxide would decide thermal expansion as concentration of ZrO_2 is same in the entire composition range. Since melting point of yttrium oxide (2698 K) is higher than the melting point of neodymium oxide (2545 K), it is expected that thermal expansion should increase with increasing concentration of Nd^{3+}. The trend of thermal expansion coefficients for the compositions $Zr_{0.70}Y_{0.15}Nd_{0.15}O_{1.85}$ and $Zr_{0.70}Nd_{0.30}O_{1.85}$ sample could not be explained because of presence of tetragonal domains and $NdO_{1.5}$ phase in $Zr_{0.70}Nd_{0.30}O_{1.85}$ sample as this logic holds true for similar type of structures as stated by Uitert et al.

It is well known that the thermal expansion coefficient is inversely proportional to the crystal energy (U). The crystal energy (U) of an ionic compound can be expressed as

$$U = \frac{N_0 A Z^+ Z^- e^2}{r_0} \left(1 - \frac{1}{n}\right) \tag{4.1}$$

where N_0, A, z, r_0, e, and n represent Avogadro's number, the Madelung constant, the ionic charge, the inter-ionic distance, the charge of an electron, and Born exponent, respectively. The substitution of smaller size Y^{3+} (1.019 Å in eight fold coordination) by larger size Nd^{3+} (1.109 Å in eight fold coordination) results in a dilation of the unit cell, indicating an increase in the average inter-ionic distance, r_0. This would lead to a decrease in the crystal energy of the $Zr_{0.70}[Y_{1-x}Nd_x]_{0.30}O_{1.85}$ ($0.0 \le x \le 1.0$) system with increasing Nd^{3+} content which basically represents the increase of thermal expansion coefficient. The same has been observed experimentally in this work

4.3.2.2. Heat capacity

The experimentally measured specific heat capacities of $Zr_{0.70}[Y_{1-x}Nd_x]_{0.30}O_{1.85}$ (x = 0.0, 0.5 and 1.0) samples along with that estimated (from Neumann-Kopp's rule) are plotted in Fig. 4.7. For the calculation of the heat capacity using NK rule, heat capacity values for Y_2O_3, Nd_2O_3 and ZrO_2 have been taken from Barin et al. [122]. The heat capacity values increase smoothly as a function of temperature and did not show any phase transition in the experimental temperature range. In all the cases negative deviation from the computed heat capacity values is observed throughout the temperature range. The experimental specific heat capacity values for each composition in the complete temperature range were fitted to a polynomial of type $A+BT+CT^{-2}$ where A, B and C are constants and T is absolute temperature. The values of these constants are given in Table 4.5

Table 4.5: The coefficients of specific heat capacity equation for $Zr_{0.70}[Y_{1-x}Nd_x]_{0.30}O_{1.85}$ (x = 0.0, 0.5 and 1.0) compositions

Compositions	$C_P^0 (J\,g^{-1}\,K^{-1}) = A + BT + CT^{-2}$ (313–713 K)		
	A	B	C
$Zr_{0.70}Y_{0.30}O_{1.85}$	0.50146	0.0001	- 9312
$Zr_{0.70}Y_{0.15}Nd_{0.15}O_{1.85}$	0.52028	0.00004	-10290
$Zr_{0.70}Nd_{0.30}O_{1.85}$	0.44971	0.00005	-7150

4.3.2.3. Thermal conductivity studies

As discussed earlier, thermal conductivity of samples is calculated from thermal diffusivity, density and specific heat values using equation 2.9. The thermal diffusivities of $Zr_{0.70}[Y_{1-x}Nd_x]_{0.30}O_{1.85}$ (x = 0.0, and 1.0) samples measured by laser flash method are shown in Fig 4.8. The values of thermal diffusivity are the arithmetic mean of five measurements. The inverse temperature dependence behaviour of thermal diffusivities for these compositions suggests a dominant phonon conduction behaviour which is the most common conduction phenomenon in polycrystalline insulator materials. It is observed that the thermal diffusivity is higher for the composition $Zr_{0.70}Y_{0.30}O_{1.85}$ compared to $Zr_{0.70}Nd_{0.30}O_{1.85}$. The temperature dependent density '$\rho(T)$' has been evaluated from bulk thermal expansion data. The experimentally measured specific heat capacity data have been used for calculation of thermal conductivity up to 700 K and beyond this temperature extrapolated heat capacity data have been used. The thermal conductivities have been calculated using equation 2.9. Since the sintered specimen are not fully (100% theoretical density) dense, the evaluated thermal conductivity data 'λ_m' have been corrected for porosity to estimate the thermal conductivity of fully dense material 'λ_{100}' by using the equation 2.10. Thermal conductivity as a function of temperature for the $Zr_{0.70}[Y_{1-x}Nd_x]_{0.30}O_{1.85}$ (x = 0.0 and 1.0) samples is shown in Fig. 4.9. It is obvious that the thermal diffusivity of all the compounds show moderate dependence on temperature, which is the typical characteristic of zirconia-based ceramics [123]. The independence from temperature is more pronounced in case of the Nd-based system. The thermal conductivity is also affected by the presence of vacancies, however, since both nominal compositions have equal content of the trivalent ion in ZrO_2, the number of vacancies do not change from one composition to the other. $Zr_{0.70}Y_{0.30}O_{1.85}$ (x = 1.0) shows higher thermal conductivity compared to $Zr_{0.70}Nd_{0.30}O_{1.85}$. Bisson et al. [124] have reported a thermal conductivity of 2.0 $Wm^{-1}K^{-1}$ for 20 mol% $YO_{1.5}$ doped ZrO_2. They have also reported a thermal conductivity of 2.7 $Wm^{-1}K^{-1}$ for $Zr_{0.665}Y_{0.335}O_{1.832}$. The thermal conductivity reported in this work for $Zr_{0.70}Y_{0.30}O_{1.85}$ is slightly lower than the reported value of Bisson et al. [124] for the composition $Zr_{0.665}Y_{0.335}O_{1.832}$. The calculated thermal conductivity of $Zr_{0.70}Nd_{0.30}O_{1.85}$ (1.7 $Wm^{-1}K^{-1}$) is somewhat higher than that reported by Liu et al. [88] for the same composition prepared by co-precipitation method (1.5 $Wm^{-1}K^{-1}$). The results can be explained as follows:

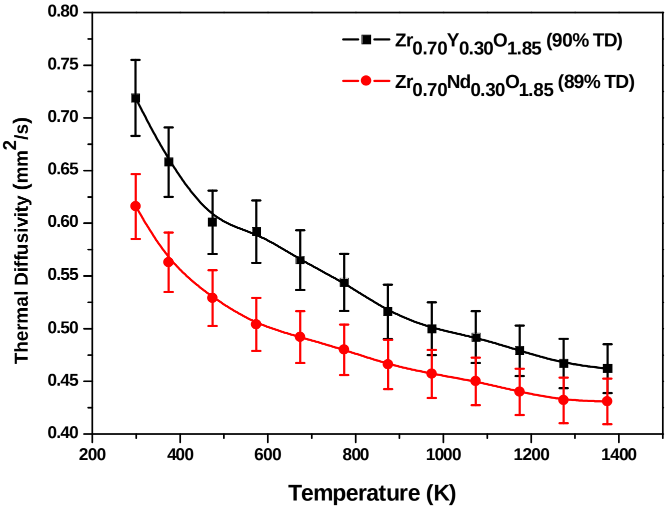

Fig. 4.8: Thermal diffusivity of $Zr_{0.70}Y_{0.30}O_{1.85}$ and $Zr_{0.70}Nd_{0.30}O_{1.85}$ as a function of temperature

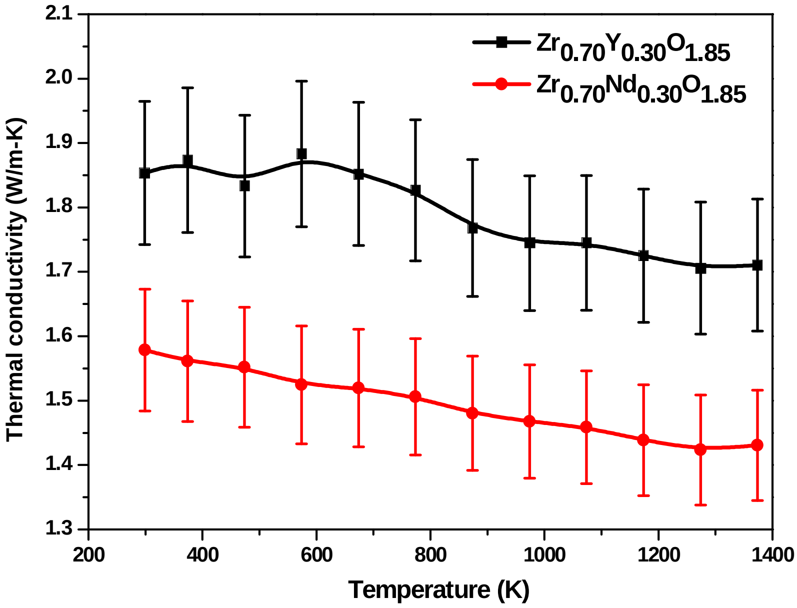

Fig. 4.9: Thermal conductivity of $Zr_{0.70}Y_{0.30}O_{1.85}$ and $Zr_{0.70}Nd_{0.30}O_{1.85}$ as a function of temperature

The phonon conduction is the only way of heat transport in these materials at least in the studied temperature range of interest. The phonon conductivity of a solid, λ_p, is given by:

$$\lambda_p = \lambda_i - \Delta\lambda_p \quad (4.2)$$

where λ_i is the intrinsic thermal conductivity (in the absence of any defects) and $\Delta\lambda_p$ is the decrease in thermal conductivity that results from phonon scattering by the defects [125, 126]. The decrease in the phonon conductivity, $\Delta\lambda_p$, is assumed to result from phonon scattering by point defects. The two types of point defects expected in these materials are substitutional solute cations (Y^{3+} and Nd^{3+}) which substitute zirconium and the corresponding oxygen vacancies created by the substitution of tetravalent zirconium by a trivalent rare-earth. Point defects decrease the phonon mean free path. The magnitude of the phonon mean free path reduction depends on (i) the point defect concentration and (ii) the scattering strength of the point defect, which is proportional to the square of the atomic weight difference and ionic radii difference between the solute and the host (Zr) cations. In this case, the concentration of oxygen vacancies is same in all the compositions and oxygen vacancies should have no role in deciding the relative thermal conductivity. The atomic weights of Zr, Y and Nd are 91, 89 and 144, respectively. The ionic radii of Zr^{4+}, Y^{3+} and $Nd^{3+}$are 0.84, 1.02 and 1.11 Å, respectively in cubic coordination [64]. The mass difference and ionic radii difference between Zr^{4+} and Nd^{3+} is much more compared to that between Zr^{4+} and Y^{3+}. This leads to a lower thermal conductivity of $Zr_{0.70}Nd_{0.30}O_{1.85}$ in comparison to $Zr_{0.70}Y_{0.30}O_{1.85}$. It has been very lucidly elucidated by Clarke [127] that thermal conductivity also depends on mean atomic weight of the compound. Higher the mean weight, lower is the thermal conductivity. By this reasoning as well, Nd-stabilised zirconia is expected to exhibit lower thermal conductivity under similar conditions. Also, presence of micro domains of tetragonal phases might act as scattering centres in the largely fluorite type matrix of $Zr_{0.70}Nd_{0.30}O_{1.8}$ and reduce the thermal conductivity further. It must be noted that pure zirconia has thermal conductivity in the range 6.6–8.2 $Wm^{-1}K^{-1}$ [126]. The lower thermal conductivity of Y^{3+} and/or Nd^{3+} doped zirconia is due to phonon scattering by particularly oxygen vacancies incorporated in the lattice as a consequence of substitution of Zr^{4+} by Y^{3+}/Nd^{3+} as the scattering strength of oxygen vacancies is larger than that of substitutional solutes because of the missing anion mass and the missing inter-atomic linkages associated with the vacancies.

4.4. Conclusion

Phase relation in $Zr_{0.70}[Y_{1-x}Nd_x]_{0.30}O_{1.85}$ ($0.0 \leq x \leq 1.0$) series has been established by using XRD and Raman spectroscopy in conjunction. Though XRD studies imply that the entire series exist as single-phasic F-type lattice, Raman studies could delineate the existence of tetragonal domains in the composition $Zr_{0.70}Nd_{0.30}O_{1.85}$. Dilatometry has been used to measure the bulk thermal expansion of selected compositions wherein the coefficient of linear thermal expansion is observed to increase with increasing content of $NdO_{1.5}$ in $Zr_{0.70}[Y_{1-x}Nd_x]_{0.30}O_{1.85}$ ($0.0 \leq x \leq 1.0$) series. Specific heat capacity of the solid solutions is found to decrease with increasing Nd_2O_3 content. Thermal conductivity of $Zr_{0.70}Nd_{0.30}O_{1.85}$ is also found to be lower compared to $Zr_{0.70}Y_{0.30}O_{1.85}$ which has been attributed to the large difference of mass and ionic size between Zr and Nd relative to Zr and Y.

CHAPTER 5

Studies in $Nd_{0.20}[Zr_{1-x}Ce_x]_{0.80}O_{1.90}$ ($0.0 \leq x \leq 1.0$) system for hosting plutonium and minor actinides

5.1. Introduction

The phase relation and thermo-physical properties in $Zr_{1-x}Nd_xO_{2-x/2}$ ($0.0 \leq x \leq 1.0$) and $Zr_{0.70}[Y_{1-x}Nd_x]_{0.30}O_{1.85}$ ($0.0 \leq x \leq 1.0$) system have been discussed in chapter 3 and 4 in the context of minor actinide (MA) transmutation (Nd_2O_3 as a MA surrogate) in zirconia matrix. In this chapter, $Nd_{0.20}[Zr_{1-x}Ce_x]_{0.80}O_{1.90}$ ($0.0 \leq x \leq 1.0$) system has been investigated in terms of phase relation and thermo-physical properties as the representative candidate for transmutation of both plutonium and MA. Cerium oxide (CeO_2) has been used as a surrogate material for plutonium oxide. In addition, CeO_2 itself is also proposed as one of the candidate materials for inert matrices. The Nd^{3+} content has been fixed at 20 mol% with the dual objective. Approximately, 20 mol% minor actinides could be loaded in transmutation targets [128] and minimum 20 mol% Nd^{3+} is required to stabilize zirconia in cubic phase completely [88, 115]. The phase relations and the solubility limits of CeO_2 may give an indication of PuO_2 loading capacity in Nd^{3+} stabilized zirconia.

5.2. Experimental

AR grade powders of ZrO_2, CeO_2 and Nd_2O_3 have been employed as the starting reagents. The stoichiometric amounts of the reactants (viz. ZrO_2, CeO_2 and Nd_2O_3) required for various nominal compositions in $Nd_{0.20}[Zr_{1-x}Ce_x]_{0.80}O_{1.90}$ ($0.0 \leq x \leq 1.0$) system have been weighed, ground, pelletized and heated at 1523 K (24 h), 1623 K (36 h) and 1723 K (48 h) each. The heatings have been performed in static air and the heating and cooling rates have been maintained at 5 K/min. All the three heating steps were interspersed with grindings in order to obtain better homogeneity in the reaction products. The sintered samples have been thoroughly characterized by X-ray diffraction (XRD) and Raman spectroscopy.

Scanning electron microscopy (SEM) and X-ray photo electron spectroscopy (XPS) have also been used. The heat capacity of representative compositions has been measured by heat flux-type DSC. Lattice thermal expansion of few selected compositions has been measured by high temperature XRD.

5.3. Results and discussion

5.3.1. Structural characterization

5.3.1.1. X-ray diffraction studies

The XRD patterns for various nominal compositions in $Nd_{0.20}[Zr_{1-x}Ce_x]_{0.80}O_{1.90}$ ($0.0 \leq x \leq 1.0$) series are shown in Fig. 5.1. The XRD pattern for the composition $Zr_{0.80}Nd_{0.20}O_{1.90}$ (x = 0.0) shows the presence of fluorite-type cubic phase along with small amount of monoclinic zirconium dioxide. It is interesting to note that gel combustion route could yield single-phasic fluorite-type phase for $Zr_{0.80}Nd_{0.20}O_{1.90}$ composition as discussed in chapter 3. Gel combustion is a chemical synthesis method and is known to achieve better atomic level mixing of the reactants leading to shorter diffusion distances and hence higher probability of obtaining single-phasic product [76]. Solid state synthesis involves larger diffusion distances and hence relatively lower solubility ranges are observed in the systems synthesized by solid state which explains appearance of small amount of m-ZrO_2 in this composition [129]. The minority m-ZrO_2 phase disappears on addition of Ce^{4+} which shows only single-phasic fluorite-type (F) phase for composition with x = 0.1. The similar trend is continued on increasing the x value from x = 0.1 to x = 1.0. This implies that the entire series exist as single-phasic F-type barring the nominal composition with x = 0.0. The XRD pattern is found to shift towards lower angle with increase in amount of CeO_2 indicating dilation of fluorite-type cubic phase upon ceria addition. The increase in lattice parameter can be explained on the basis of the relative ionic radii of Ce^{4+} and Zr^{4+} (ionic radii of Ce^{4+}= 0.97 Å, Zr^{4+} = 0.84 Å in eight-fold coordination) [64].

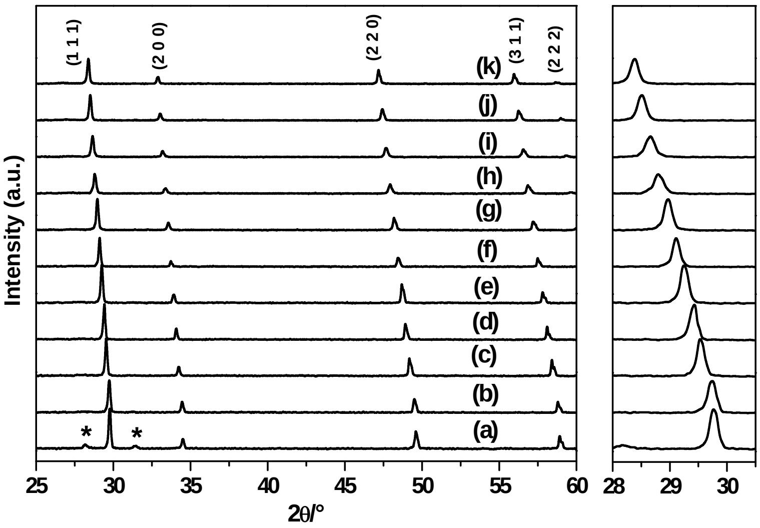

Fig. 5.1: XRD patterns in $Nd_{0.20}[Zr_{1-x}Ce_x]_{0.80}O_{1.90}$ samples: (a) x = 0.0, (b) x = 0.1, (c) x = 0.2, (d) x = 0.3, (e) x = 0.4, (f) x = 0.5, (g) x = 0.6, (h) x = 0.7, (i) x = 0.8, (j) x = 0.9 and (k) x = 1.0. * represents minor monoclinic ZrO_2 phase

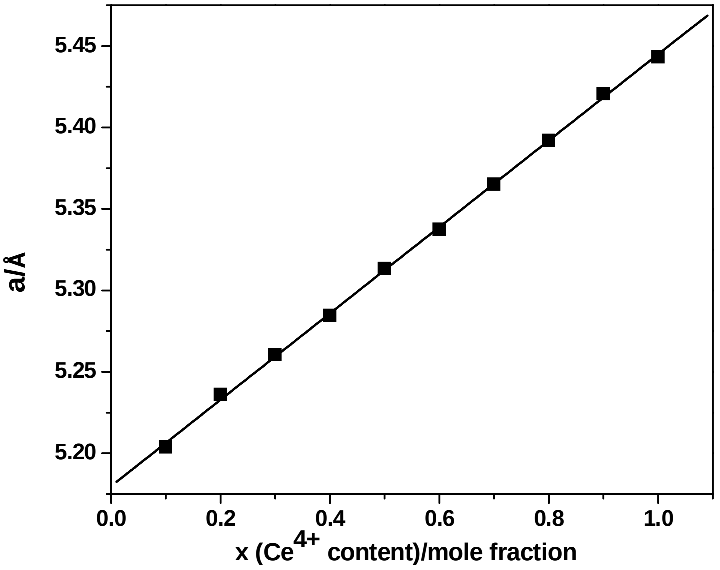

Fig. 5.2: Variation of lattice parameter in $Nd_{0.20}[Zr_{1-x}Ce_x]_{0.80}O_{1.90}$ ($0.0 \leq x \leq 1.0$) system as a function of ceria content

Since the content of Nd^{3+} is constant throughout the series, the substitution of smaller size Zr^{4+} by relatively larger Ce^{4+}, increases effective cationic size leading to increase in lattice parameter. The XRD patterns for all the phases have been refined using POWDERX and their cell parameters are determined. Table 5.1 lists the phases observed along with the lattice parameter values. An almost ideal Vegard's law type of behaviour has been observed for the variation of cell parameter with composition and is depicted in Fig. 5.2.

Table 5.1: Phases and lattice parameters in $Nd_{0.20}[Zr_{1-x}Ce_x]_{0.80}O_{1.90}$ ($0.0 \leq x \leq 1.0$) system (F: Fluorite, M: Monoclinic, #: not refined due to insignificant intensity)

Composition	Phases	Lattice parameter (Å)
$Zr_{0.80}Nd_{0.20}O_{1.90}$	F M	5.195(1) #
$Zr_{0.72}Ce_{0.08}Nd_{0.20}O_{1.90}$	F	5.204(2)
$Zr_{0.64}Ce_{0.16}Nd_{0.20}O_{1.90}$	F	5.236(1)
$Zr_{0.56}Ce_{0.24}Nd_{0.20}O_{1.90}$	F	5.260(3)
$Zr_{0.48}Ce_{0.32}Nd_{0.20}O_{1.90}$	F	5.284(2)
$Zr_{0.40}Ce_{0.40}Nd_{0.20}O_{1.90}$	F	5.313(2)
$Zr_{0.32}Ce_{0.48}Nd_{0.20}O_{1.90}$	F	5.337(1)
$Zr_{0.24}Ce_{0.56}Nd_{0.20}O_{1.90}$	F	5.365(2)
$Zr_{0.16}Ce_{0.64}Nd_{0.20}O_{1.90}$	F	5.392(2)
$Zr_{0.08}Ce_{0.72}Nd_{0.20}O_{1.90}$	F	5.421(1)
$Ce_{0.80}Nd_{0.20}O_{1.90}$	F	5.443(2)

Grover et al. have reported the phase relations in the binary system $Zr_{1-x}Ce_xO_2$ ($0.0 \leq x \leq 1.0$) system wherein single phase is obtained only for $x \geq 0.8$ [130]. Zhang et al. have also studied the ceria-zirconia binary oxide system and they could obtain single-phasic F-type phase field upto 40 mol% ZrO_2 dissolved in CeO_2 [131]. In both cases, biphasic mixture was obtained at zirconia rich region. Both the studies confirm that isovalent substitution with larger cation size is not sufficient to stabilize zirconia in cubic phase. The oxygen vacancies introduced in the lattice accompanying a lower valent larger guest cation leads to additional stabilization by increasing entropy of the system. It is therefore interesting that addition of 20 mol% Nd^{3+} makes ZrO_2–CeO_2 binary system single-phasic in the entire composition range. This may be attributed to the role of vacancies created by the presence of Nd^{3+} in stabilizing the cubic lattice in zirconia-rich region. The importance of vacancies for stabilization of cubic zirconia has also been emphasized by theoretical studies [132].

XPS studies have also been carried out on the representative nominal composition $Nd_{0.20}Zr_{0.40}Ce_{0.40}O_{1.90}$ in order to rule out any reduction of Ce^{4+} to Ce^{3+} during high temperature heating of CeO_2 containing compositions. In order to obtain the true representation of the bulk valence state of cerium, the pellet belonging to the nominal composition $Nd_{0.20}Zr_{0.40}Ce_{0.40}O_{1.90}$ has been well ground and XPS studies have been carried out on the powdered sample. Fig. 5.3 shows the XPS spectrum of $Nd_{0.20}Zr_{0.40}Ce_{0.40}O_{1.90}$. Paparazzo et al. [133] have reported that the $3d_{5/2}$ XPS peak for Ce_2O_3 (Ce^{3+}) are observed at 880.9 and 885.3 eV. Since the deconvoluted spectra do not show any peaks at these positions, the presence of Ce^{3+} can be ruled out.

There are no reports in literature on ternary system consisting of CeO_2–ZrO_2–Nd_2O_3. However, the results in present study are in good agreement with that reported in the phase relation studies on $Y_{0.2}[Zr_{1-x}Ce_x]_{0.8}O_{1.9}$ ($0.0 \leq x \leq 1.0$) system by Sakai et al. [134]. They have observed the complete solid solution formation in the whole range of compositions annealed above 1473 K. Eufinger et al. [135] have reported a comprehensive defect chemical analysis of the system $(Ce_{1-x}Zr_x)_{0.8}Y_{0.2}O_{1.9}$ and have mentioned that the fixed amount of Y^{3+} (trivalent ion) helps in retaining the cubic fluorite structure throughout.

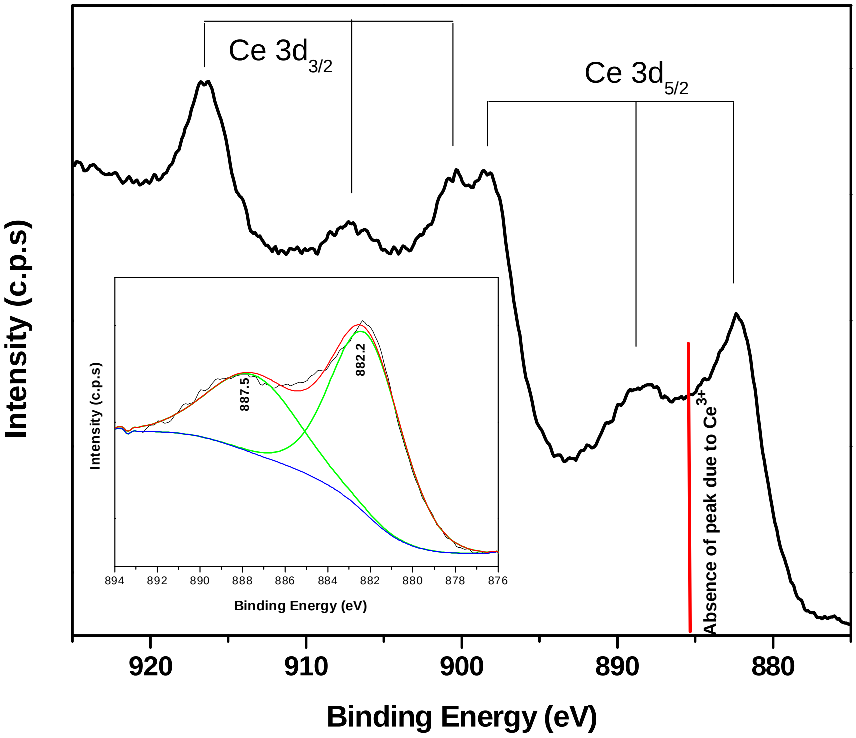

Fig. 5.3: XPS spectrum showing Ce-3d peak for $Nd_{0.20}Zr_{0.40}Ce_{0.40}O_{1.90}$. The inset shows the deconvoluted peak of Ce-$3d_{5/2}$

The significant implication of this result is that the loading of CeO_2 (surrogate for plutonia) in ZrO_2 will not yield a single-phasic product but when substituted along with Nd^{3+} (surrogate for Am^{3+}), a single-phasic composition is attainable. This is encouraging considering that single-phasic compositions are expected to possess superior and homogeneous properties. This indicates the structural feasibility of co-loading of Am^{3+} and Pu^{4+} in ZrO_2 for MA transmutation.

5.3.1.2. Raman spectroscopic studies

Though XRD demonstrates existence of single-phase crystal structure in the entire composition range, presence of small amount of monoclinic and tetragonal phase in this series could not be ruled out completely because of its resemblances with $Zr_{1-x}Ce_xO_2$ ($0.0 \leq x \leq 1.0$) system which exhibits variety of phases depending on composition [130]. In order to shed some light on all these queries, the samples have been subjected to Raman spectroscopic study which is widely used in conjunction with XRD for inspecting local structural changes.

The Raman spectra of the sintered samples in $Nd_{0.20}[Zr_{1-x}Ce_x]_{0.80}O_{1.90}$ ($0.0 \leq x \leq 1.0$) series are presented in Fig. 5.4(a). In case of $Zr_{0.80}Nd_{0.20}O_{1.90}$ ($x = 0.0$), Raman bands at 178, 189, 222, 332, 344, 379, 473, 501, 535, 557, 612 cm^{-1} in the frequency range 50–800 cm^{-1} have been observed. All the observed modes are in good agreement with the previously published literature data for the Raman modes of m-ZrO_2 [97]. This concurs with the presence of little amount of m-ZrO_2 in XRD pattern for this nominal composition. The cubic stabilized zirconia, inspite of being the majority phase, could not be clearly observed in the Raman pattern because it possesses weak and very broad Raman features which could be masked by highly crystalline m-ZrO_2 (minority phase) Raman modes. The broad Raman features of cubic stabilized ZrO_2 are due to highly defective structure of stabilized zirconia and are described in chapter 3. At 10 mol% substitution of ZrO_2 by CeO_2, (i.e. the nominal composition $Zr_{0.72}Ce_{0.08}Nd_{0.20}O_{1.90}$), major changes in Raman spectrum are observed. High intensity m-ZrO_2 bands are found to disappear and low intensity two broad bands of almost equal intensity peaking at 606 cm^{-1} and 312 cm^{-1} emerge. The broad band at around 606 cm^{-1} is the characteristic band of cubic zirconium oxide which has defect fluorite structure. The broad band at around 610 cm^{-1} is observed in the Raman spectrum of yittria stabilized zirconia [99]. When the CeO_2 content is increased to 20 mol %, (composition

$Zr_{0.64}Ce_{0.16}Nd_{0.20}O_{1.90}$), no appreciable change in Raman pattern is observed. With 30 mol% substitution of ZrO_2 by CeO_2, (composition $Zr_{0.56}Ce_{0.24}Nd_{0.20}O_{1.90}$), a broad band between two bands of cubic stabilized zirconia tend to appear. A broad band at around 489 cm^{-1} with two more bands at 295 and 600 cm^{-1} is observed when 40 mol% of ZrO_2 is replaced by CeO_2. On 50 mol% substitution of Zr^{4+} by Ce^{4+}, the Raman spectra qualitatively looks similar but the intensity of Raman band at ~ 460 cm^{-1} increases with the concomitant decrease in intensity of Raman bands at ~ 290 and ~ 600 cm^{-1} accompanied with a shift towards lower frequency region. The gradual appearance and increase in intensity of the Raman band at ~ 460 cm^{-1} is clearly depicted in Fig. 5.4(b). A shift towards lower frequency region is observed for the bands at ~ 290 and ~ 600 cm^{-1} as well. Three bands are found to appear at 289, 479 and 595 cm^{-1} for the composition $Zr_{0.40}Ce_{0.40}Nd_{0.20}O_{1.90}$ which exist till the entire Zr^{4+} is substituted by Ce^{4+} leading to $Ce_{0.80}Nd_{0.20}O_{1.90}$. In this composition Raman bands appeared at 253, 459 and 547 cm^{-1}. All these bands are found to shift to a lower frequency region with increasing CeO_2 concentration but the exact shift is difficult to determine because of asymmetric nature of the bands. It is reported in the literature that for ceria lattice, the main Raman band (F_{2g} mode) appears at around 460 cm^{-1} and if the ceria lattice contains vacancies due to the presence of trivalent ions, additional weak bands at 260, 560 and 600 cm^{-1} are observed. The main Raman band at 460 cm^{-1} is due to O-Ce-O stretch in CeO_2 fluorite lattice (Fig. 5.4(a)). It has been shown by Nakajima et al. [136] that in ceria doped with trivalent ions, defect bands at 600 cm^{-1} is due to foreign guest cations in O_h symmetry. The bands at 260 and 560 cm^{-1} are, however, due to various metal-vacancy and oxygen vacancy complexes (Fig. 5.4 (b)). A very broad band at 560 cm^{-1} is due to the superposition of two bands (560 and 600 cm^{-1}). Therefore, it is clear that observed bands for the composition $Ce_{0.80}Nd_{0.20}O_{1.90}$ are in accordance to literature data.

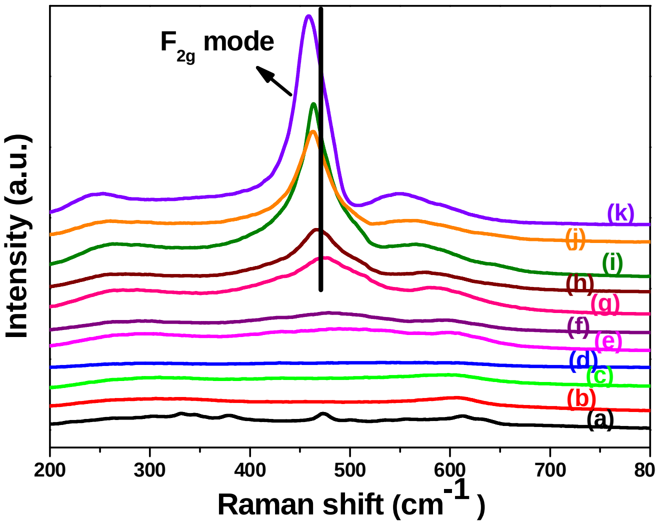

Fig. 5.4(a): Raman spectra in $Nd_{0.20}[Zr_{1-x}Ce_x]_{0.80}O_{1.90}$ samples: (a) x = 0.0 (b) x = 0.1, (c) x = 0.2, (d) x = 0.3, (e) x = 0.4, (f) x = 0.5, (g) x = 0.6, (h) x = 0.7, (i) x = 0.8, (j) x = 0.9 and (k) x = 1.0

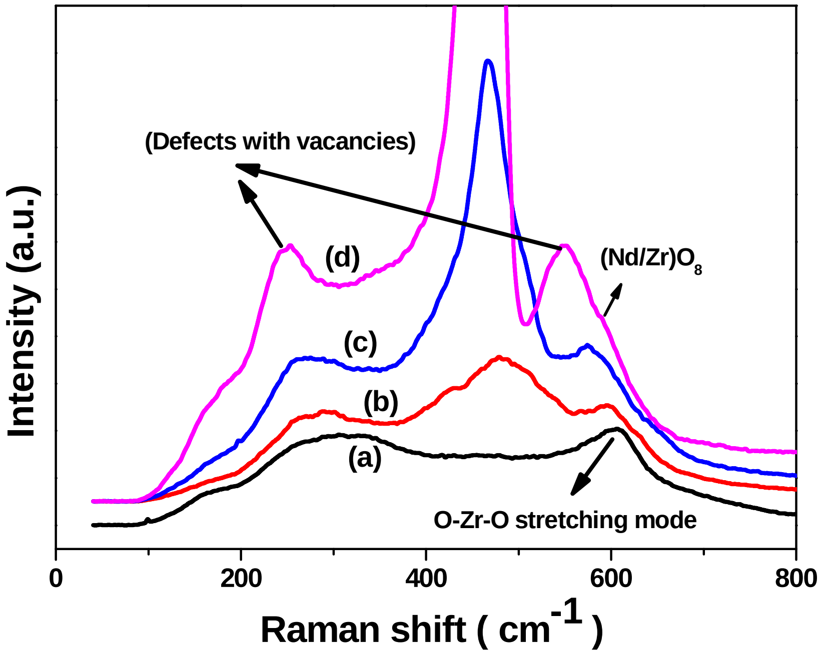

Fig. 5.4(b): Raman spectra in $Nd_{0.20}[Zr_{1-x}Ce_x]_{0.80}O_{1.90}$ samples with typical modes: (a) x = 0.1, (b) x = 0.5, (c) x = 0.7 and (d) x = 1.0

The frequency shift in the Raman bands of a material is dependent on reduced mass and bond strength. On substituting Zr^{4+} in $Ce_{0.80}Nd_{0.20}O_{1.90}$ there is a decrease in average ionic radii, since Zr^{4+} is smallest among all the three cations. The decrease in average cationic radius increases the average M-O bond length. This manifests as the blue shift of the Raman mode at 460 cm^{-1} with increase in Zr^{4+} content [137]. The same observation has been found in ZrO_2–CeO_2 series also [138].

The XRD studies shows an Fm-3m lattice for the entire region but Raman studies delineate the difference in local structure and the defects in the solid solutions possessing similar bulk symmetry. Therefore, the Raman analysis in the entire composition range shows difference in local structure of fluorite-type phases with variation in Ce^{4+}-content (or Zr^{4+}-content). They can be broadly classified as two kinds of fluorite-type lattices: cubic stabilized zirconia-type and cubic defect ceria-type.

5.3.1.3. SEM and EDS Studies

SEM image of sintered sample of the composition $Zr_{0.64}Ce_{0.16}Nd_{0.20}O_{1.90}$ is presented in Fig. 5.5. It represents the single phasic microstructure of the sample. SEM image indicates well packed and regular grains. The grain boundaries are well developed and the grain size varies roughly from ~ 10 to 20 μm. The compositional analysis has been carried out on this particular sample using Energy Dispersive Spectroscopy (EDS). It is found that the sample contains 68% Zr, 15% Ce and 17% Nd. Thus, the overall composition is observed to be in good agreement with the proposed nominal composition.

5.3.2. Thermophysical studies

An important criterion for the materials envisaged for nuclear applications is their favourable thermo-physical properties. In this section, heat capacity and thermal expansion of the representative compositions in $Nd_{0.20}[Zr_{1-x}Ce_x]_{0.80}O_{1.90}$ ($0.0 \leq x \leq 1.0$) system are described.

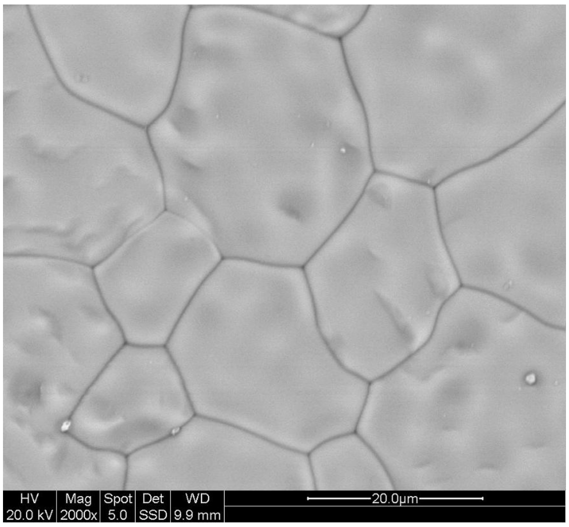

Fig. 5.5: SEM image of sintered $Zr_{0.64}Ce_{0.16}Nd_{0.20}O_{1.90}$

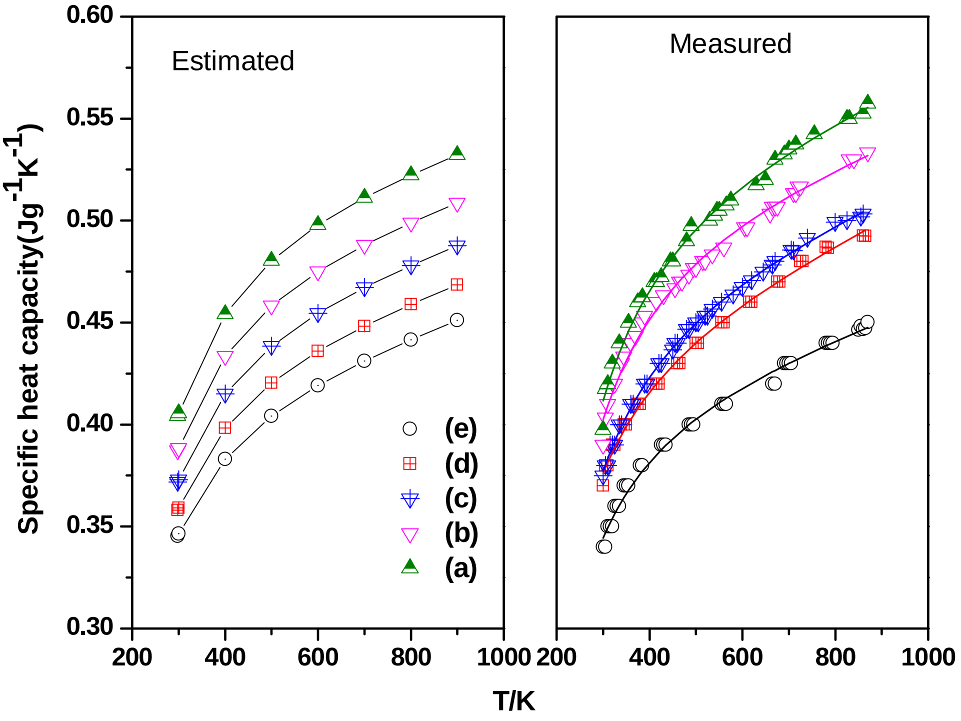

Fig. 5.6: Specific heat capacities in $Nd_{0.20}[Zr_{1-x}Ce_x]_{0.80}O_{1.90}$ samples as a function of temperature: (a) x = 0.2, (b) x = 0.4 , (c) x = 0.6 , (d) x = 0.8 and (e) x = 1.0

5.3.2.1. Heat capacity

Heat capacity has been measured for $Nd_{0.20}[Zr_{1-x}Ce_x]_{0.80}O_{1.90}$ (x = 0.2, 0.4, 0.6, 0.8, 1.0) samples in the temperature range 300–870 K. At each temperature, the measurement has been repeated four times and the mean value of the four measurements is taken as final heat capacity. The standard deviation for all the compositions is found to be within 1-2%. The experimentally measured specific heat capacities of $Nd_{0.20}[Zr_{1-x}Ce_x]_{0.80}O_{1.90}$ (x = 0.2, 0.4, 0.6, 0.8, 1.0) system along with that estimated (from Neumann-kopp’s (NK) rule) are plotted in Fig. 5.6. For the calculation of the heat capacity using NK rule, heat capacity values for Nd_2O_3 and ZrO_2 have been taken from Barin et al. [122] and for CeO_2 the values has been taken from the work of Sahu et al. [139]. It is observed that experimentally determined specific heat capacity values of $Nd_{0.20}[Zr_{1-x}Ce_x]_{0.80}O_{1.90}$ (x = 0.2, 0.4, 0.6, 0.8, 1.0) system and their additive specific heat values follow similar trend. The specific heat capacity values are found to increase with the increase in Zr^{4+} content. This can be explained on the basis of ZrO_2 possessing highest value of specific heat among the three constituent oxides. The heat capacity increases smoothly as a function of temperature and does not show any phase transition in these samples in the experimental temperature range. Though, the heat capacity for $Nd_{0.20}Ce_{0.80}O_{1.90}$ (composition with x = 1.0) does not show any deviation from the NK values but the heat capacity for all other compositions shows positive deviation in the whole temperature range with the maximum deviation of 6.5% in the case of $Nd_{0.20}[Zr_{0.16}Ce_{0.64}]O_{1.90}$ (composition with x = 0.2). The excess heat capacity values seem to indicate an excess vibrational component, which can be attributed to differences in ionic radii of host and the substituent cations. In general, the lattice heat capacity changes with change of phonon frequency as the consequence of substitution of foreign ions [140-142]. Hence, in the present study, the positive deviation from additive values (obtained from NK rule) which indicates the non ideal behaviour of heat capacity is most plausibly due to the substitution of Ce^{4+} by

Zr^{4+} in $Nd_{0.20}[Zr_{1-x}Ce_x]_{0.80}O_{1.90}$ series. The experimental specific heat capacity values for each composition, in the complete temperature range have been best fitted to $A+BT+CT^{-2}$ equation where, A, B, and C are the constants and *T* is absolute temperature. The values of these constants are given in Table 5.2.

5.3.2.2 Thermal expansion

In order to investigate the lattice thermal expansion, HT-XRD studies has been performed on representative nominal compositions by recording the XRD patterns *in situ* at various temperatures. The lattice parameters at different temperature in $Nd_{0.20}[Zr_{1-x}Ce_x]_{0.80}O_{1.90}$ (x = 0.1, 0.5 and 0.9) samples are given in Table 5.3. The lattice parameters can be fitted as function of temperature using a second order regression and the fitting equations for different compositions are given below (a in Å, T in K).

$Zr_{0.72}Ce_{0.08}Nd_{0.20}O_{1.90}$:

$$a_T = 5.18295 + (6.05754 \times 10^{-5})\,T - (8.27138 \times 10^{-9})\,T^2 \qquad (5.1)$$

$Zr_{0.40}Ce_{0.40}Nd_{0.20}O_{1.90}$:

$$a_T = 5.29162 + (5.65028 \times 10^{-5})\,T + (2.52072 \times 10^{-9})\,T^2 \qquad (5.2)$$

$Zr_{0.08}Ce_{0.72}Nd_{0.20}O_{1.90}$:

$$a_T = 5.40327 + (4.56725 \times 10^{-5})\,T + (1.3898 \times 10^{-8})\,T^2 \qquad (5.3)$$

The percentage lattice thermal expansion has been computed using the experimental data from the expression 2.2 and is plotted in Fig. 5.7 which shows that % lattice thermal expansion increases with increase in temperature up to 1273 K. The average lattice thermal expansion coefficient (α_a) has been computed using the equation 2.3. The average lattice thermal expansion coefficient (α_a) in $Nd_{0.20}[Zr_{1-x}Ce_x]_{0.80}O_{1.90}$ (x= 0.1, 0.5 and 0.9) samples are given in Table 5.3. It reveals that the coefficients of lattice thermal expansion of the samples increase with increasing content of CeO_2 in $Nd_{0.20}[Zr_{1-x}Ce_x]_{0.80}O_{1.90}$ ($0.0 \leq x \leq 1.0$) series.

Table 5.2: The coefficients of specific heat capacity equation for $Nd_{0.20}[Zr_{1-x}Ce_x]_{0.80}O_{1.90}$ ($0.0 \leq x \leq 1.0$) compositions

$Nd_{0.20}[Zr_{1-x}Ce_x]_{0.80}O_{1.90}$	**$C_P^0(Jg^{-1}K^{-1}) = A + BT + CT^{-2}$ (300–870 K)**		
x	A	B x 10^5	C
1.0	0.3879	7.6	- 6012
0.8	0.4096	11.0	- 5938
0.6	0.4377	9.0	- 8112
0.4	0.4703	8.1	- 8366
0.2	0.4841	9.3	- 9104

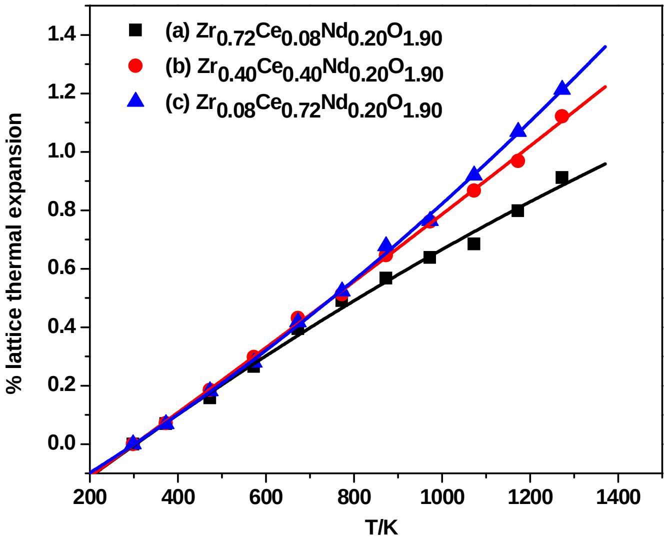

Fig. 5.7: Lattice thermal expansion (%) as a function of temperature in $Nd_{0.20}[Zr_{1-x}Ce_x]_{0.80}O_{1.90}$ samples: (a) x = 0.1, (b) x = 0.5 and (c) x = 0.9

Table 5.3: Lattice parameters at different temperatures and average lattice thermal expansion coefficient (α_a) in $Nd_{0.20}[Zr_{1-x}Ce_x]_{0.80}O_{1.90}$ (x = 0.1, 0.5 and 0.9) samples

Temp (K)	Lattice parameter(a/Å)		
	$Zr_{0.72}Ce_{0.08}Nd_{0.20}O_{1.90}$	$Zr_{0.40}Ce_{0.40}Nd_{0.20}O_{1.90}$	$Zr_{0.08}Ce_{0.72}Nd_{0.20}O_{1.90}$
RT	5.2006	5.3089	5.4183
373	5.2042	5.3127	5.4220
473	5.2088	5.3187	5.4281
573	5.2144	5.3247	5.4334
673	5.2211	5.3318	5.4409
773	5.2261	5.3361	5.4466
873	5.2301	5.3432	5.4550
973	5.2338	5.3493	5.4597
1073	5.2362	5.3549	5.4681
1173	5.2421	5.3603	5.4762
1273	5.2480	5.3684	5.4840
$\alpha_a \times 10^6$ (K^{-1}) (298–1273 K)	9.35	11.50	12.44

As discussed in chapter 4, in any system, the lattice thermal expansion is governed by two factors namely (a) the melting point of the constituents and (b) vacancies in the system. Hence, it can be stated that in this system, materials with lower melting point are expected to have higher thermal expansion. The incorporation of vacancies, on the other hand, is likely to mask thermal expansion. In the present study, the concentration of vacancies is same in the entire composition range due to constant amount of Nd^{3+} and it is expected that the melting points of the constituent oxides should govern the lattice thermal expansion. In other words, melting point of zirconia and ceria will decide the thermal expansion of these compositions as concentration of Nd_2O_3 is same in the entire composition range. Since the melting point of zirconia (2988 K) is more than the melting point of ceria (2673 K), it is expected that thermal expansion should increase with increasing concentration of CeO_2. The same has been observed experimentally in this work.

5.4. Conclusion

In view of relevance of $Nd_{0.20}[Zr_{1-x}Ce_x]_{0.80}O_{1.90}$ system to inert matrix fuel from the point of view of co-doping of Pu and Am, the phase relations in the $Nd_{0.20}[Zr_{1-x}Ce_x]_{0.80}O_{1.90}$ ($0.0 \leq x \leq 1.0$) system has been investigated. The system has been thoroughly characterized structurally by XRD and Raman spectroscopy. It is observed that substitution of a trivalent ion like Nd^{3+} could stabilize the otherwise multi-phasic CeO_2–ZrO_2 system and the entire phase relation is revealed to be single-phasic F-type throughout the composition range. The Raman studies corroborated the XRD results and revealed the evolution of defects on proceeding from Zr-rich to Ce-rich region. Heat capacity values have been reported for $Nd_{0.20}[Zr_{1-x}Ce_x]_{0.80}O_{1.90}$ ($0.0 \leq x \leq 1.0$) system in the temperature range of 300–870 K which are found to increase with Zr^{4+}-content. HT-XRD studies have been employed to determine the lattice thermal expansion coefficients which are observed to increase with increase in CeO_2 content in Nd^{3+}-stabilized cubic zirconia. The observed solubility of Nd^{3+} in CeO_2–ZrO_2 system in a single-phasic cubic structure is a significant result in context of potential candidates for minor actinide transmutation and inert matrix fuel.

CHAPTER 6

Phase relations in YSZ/ZrO_2–PuO_2 system

6.1. Introduction

The loading of minor actinides (MAs) and PuO_2 in zirconia based matrix and their thermal properties have been simulated using the non-radioactive surrogate materials Nd_2O_3 and CeO_2, respectively and discussed in the chapters 3-5. In this chapter, radioactive PuO_2 material instead of surrogate materials has been employed as the fissile element containing phase in the investigation of phase relations and thermo-physical properties in YSZ–PuO_2 and ZrO_2–PuO_2 system. The phase relations in $(YSZ)_{1-x}(PuO_2)_x$ $(0.0 \leq x \leq 0.5)$ system would mimic loading of PuO_2 in YSZ matrix while phase relation in ZrO_2–PuO_2 system could be important for PuO_2 loading in pure zirconia matrix. The present study aims at synthesis and characterization of $(YSZ)_{1-x}(PuO_2)_x$ $(0.0 \leq x \leq 0.5)$ system by vacuum heating at appropriate temperature. The phase evolution and their lattice parameter variation have been studied as a function of PuO_2 content in the series under same conditions. The modifications upon oxidation in terms of phases and lattice parameters for each composition have been discussed in this chapter. The shrinkage behaviour and thermal expansion on selected compositions in this series have also been presented. In ZrO_2–PuO_2 system, it is aimed to prepare two compositions (e.g. $Zr_{0.8}Pu_{0.2}O_{2-x}$ and $Zr_{0.5}Pu_{0.5}O_{2-x}$) under reducing conditions (Ar–8% H_2) and characterization of the products in terms of phase content. The structural transformation upon oxidation of the products has also been discussed. Finally, the evolution of phases of PuO_2 under different reaction conditions is also elaborated.

6.2. Experimental

The synthesis of various compositions has been carried out by conventional solid state route. AR grade powders of YSZ (8 mol% Y_2O_3 stabilized zirconia) and ZrO_2 have been used as the starting materials.

PuO_2 from plutonium oxalate route has been used for the present study. The stoichiometric amount of the reactants (viz. YSZ, ZrO_2 and PuO_2) required for various nominal compositions were weighed and mixed together to get a homogeneous mixture using mortar and pestle in alcohol medium. The mixed powder was then pressed into pellets (~ 8 mm diameter, ~ 2 mm and 5 mm height) at 350 MPa using hydraulic press. The weighing as well as pelletization was performed in the glove box. The synthesis has been carried out in a single step heat treatment at 1773 K (12 h) under dynamic vacuum conditions (10^{-3} mbar). Similarly, two compositions in ZrO_2–PuO_2 system have been prepared in reducing atmosphere (Ar–8% H_2) following the same procedure. Pure PuO_2 has been subjected to heat treatment at 1773 K (12 h) under vacuum as well as in reducing atmosphere. Also PuO_2 admixed with stoichiometric amount of graphite required for conversion of PuO_2 to Pu_2O_3 has been subjected to same heat treatment in vacuum. The heating and cooling rates were maintained at 5 K/min. Oxidation of all samples has been carried out in an induction furnace at ~ 1373 K for 10 minutes in presence of oxygen. The products have been thoroughly characterized by X-ray diffraction (XRD). The shrinkage behaviour on green pellets of few selected compositions has been studied using a high temperature vertical dilatometer. The thermal expansion behaviour on two sintered samples has been studied using the same dilatometer under similar experimental conditions up to 1673 K.

6.3. Results and discussion

6.3.1. Structural characterization

6.3.1.1. $(YSZ)_{1-x}(PuO_2)_x$ ($0.0 \leq x \leq 0.5$) system

The XRD patterns for various nominal compositions in $(YSZ)_{1-x}(PuO_2)_x$ ($0.0 \leq x \leq 0.5$) series after heating under dynamic vacuum conditions at 1773 K are shown in Fig. 6.1. The XRD for pure YSZ (x = 0.0) shows the presence of Fluorite-type cubic phase. The diffraction pattern remains same with increasing the x value from x = 0.0 to x = 0.2 implying the retention of fluorite type phase till the composition with x = 0.2. The diffraction peaks corresponding to F-type lattice along with emergence of few very weak superstructure peaks are observed in XRD pattern for the composition x = 0.3. These weak (superstructure) reflections which appear due to long-range ordering of the cations and anions are the characteristics of the pyrochlore phase. Thus, the composition with x = 0.3 crystallizes in pyrochlore phase (space group Fd-3m). It must be mentioned that typical pyrochlore structure $A_2B_2O_7$ (where A and B are trivalent and tetravalent cations, respectively) is an ordered derivative of the fluorite structure (AO_2) possessing double lattice parameter. Moreover, A and B cations occupy two crystallographically distinct lattice sites (A and B are 8 and 6-fold coordinated, respectively) and one-eighth of the anions are absent. The $A_{0.5}B_{0.5}O_{1.75}$ type compounds with cations of relatively closer ionic radii ($r_A/r_B < 1.46$) crystallize in disordered fluorite-type structure while pyrochlore structure is favoured when r_A/r_B typically falls in the range 1.46 to 1.80 [101]. In the present case, under the influence of dynamic vacuum condition and very high reaction temperature (1773 K) some fraction of Pu^{4+} in PuO_2 is converted to Pu^{3+} (larger in size as compared to Pu^{4+}) which increases average cationic size. Also, conversion of Pu^{4+} to Pu^{3+} leads to creation of oxygen vacancies in the lattice. Thus both the factors i.e. increase in average cationic size and change in oxidation state (resulting oxygen vacancies) favour the formation of pyrochlore phase for the composition x = 0.3 and beyond. Apparently, relatively lower concentration of Pu^{3+} ions for the composition x = 0.2 is not enough to cause cation ordering in the structure and hence only defect fluorite phase is observed. The diffraction pattern further remains same with increasing x value from 0.3 to 0.5 suggesting the existence of pyrochlore phase up to the composition x = 0.5. In fact, under same experimental condition a biphasic mixture of PuO_2 and bcc α-Pu_2O_3 was observed for pure PuO_2 sample confirming conversion of Pu^{4+} to Pu^{3+}.

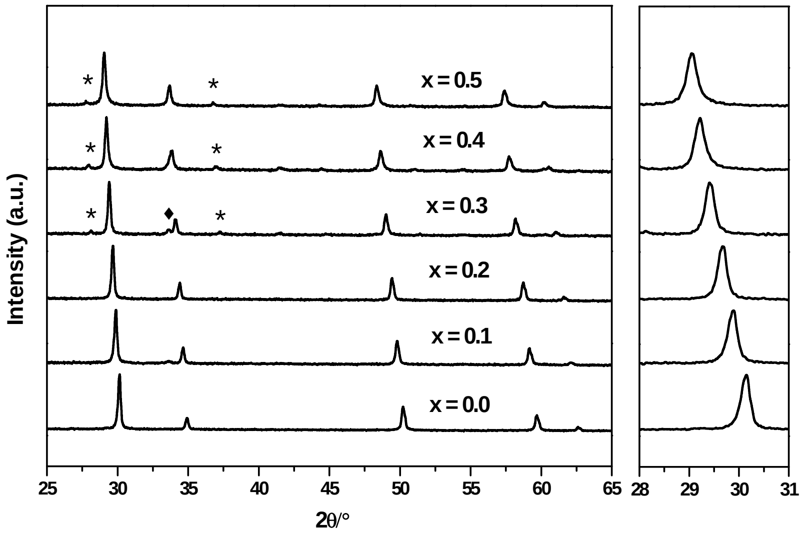

Fig. 6.1: XRD patterns of $(YSZ)_{1-x}(PuO_2)_x$ ($0.0 \leq x \leq 0.5$) system prepared in vacuum. (* represents superstructure reflection of pyrochlore phase and ♦ represents unidentified peak)

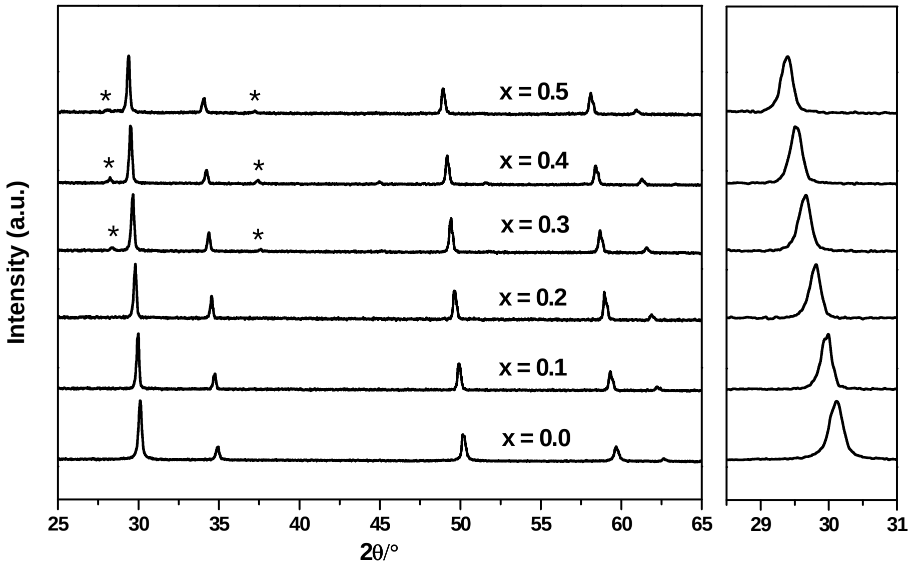

Fig. 6.2: XRD patterns of $(YSZ)_{1-x}(PuO_2)_x$ ($0.0 \leq x \leq 0.5$) system oxidised in oxygen. (* represents superstructure reflection of pyrochlore phase)

This will also be discussed later in this chapter. It must be mentioned that Yamashita et al. [143] did not observe any pyrochlore phase in YSZ–PuO_2 system under vacuum heating condition. However, they have showed that samples with $x < 0.3$ exhibit the fluorite structure and those $x > 0.3$ show the pyrochlore structure when the samples are heated in Ar–8% H_2.

A shift in the XRD pattern towards lower angle is observed with increase in PuO_2 content. This indicates the dilation of fluorite-type cubic phase upon PuO_2 addition. The increase in lattice parameter can be explained on the basis of the relative ionic radii of guest and host ions. The ionic radii of Zr^{4+}, $Y^{3+}$and Pu^{4+}, in eight-fold coordination, are 0.84, 1.02 and 0.96 Å, respectively [64]. The calculated effective cationic size in YSZ may be approximately 0.87 Å in eight coordination based on cationic sizes of Zr^{4+} and Y^{3+}. Thus the substitution of smaller-sized Zr^{4+}/Y^{3+} in YSZ by relatively larger Pu^{4+}, increases effective cationic size leading to increase in lattice parameter. Moreover, the experimental condition favours the formation of some fraction of Pu^{3+} which is still larger in size compared to Pu^{4+}. This further increases the lattice parameter in the product.

In order to investigate the effect of variable oxidation state of plutonium (under different atmosphere) on phase relation in this system, the nominal compositions have been heated in oxidising atmosphere (oxygen) and characterized by XRD. The XRD pattern of oxidised material for all the composition is shown in Fig. 6.2. The fluorite-type phase (synthesized in vacuum) for the composition $x = 0.0$ to 0.2 does not change upon oxidation, however, a shift in the diffraction pattern towards higher angle is observed for each composition. A representative XRD pattern for the composition $x = 0.2$ prepared in vacuum condition and after oxidation in oxygen is depicted in Fig. 6.3.

Similarly, the pyrochlore phase (synthesized in vacuum) for the composition $x = 0.3$ to 0.5 does not change upon oxidation but a shift is observed towards higher angle for each composition.

The noticeable difference is the decrease in intensity of the superstructure reflection after oxidation. This clearly indicates that the ordering is getting decreased and pyrochlore phase is tending towards fluorite phase. The reason is attributed to conversion of larger size Pu^{3+} to smaller size Pu^{4+} upon oxidation which effectively reduces trivalent to tetravalent cation ratio as well as r_A/r_B ratio thereby lowering the ordering in the system proceeding towards fluorite type phase.

Table 6.1: Phases present in the $(YSZ)_{1-x}(PuO_2)_x$ ($0.0 \leq x \leq 0.5$) compositions heated in vacuum and after oxidation with lattice parameter; F: Fluorite; P: Pyrochlore

Composition	Sample history	Phases identified by XRD	Lattice parameter (Å)
YSZ	Heated in vacuum	F	5.138
	Oxidised	F	5.137
0.9 YSZ–0.1 PuO_2	Heated in vacuum	F	5.174
	Oxidised	F	5.168
0.8 YSZ–0.2 PuO_2	Heated in vacuum	F	5.212
	Oxidised	F	5.193
0.7 YSZ–0.3 PuO_2	Heated in vacuum	P	10.510
	Oxidised	P	10.430
0.6 YSZ–0.4 PuO_2	Heated in vacuum	P	10.590
	Oxidised	P	10.474
0.5 YSZ–0.5 PuO_2	Heated in vacuum	P	10.637
	Oxidised	P	10.525

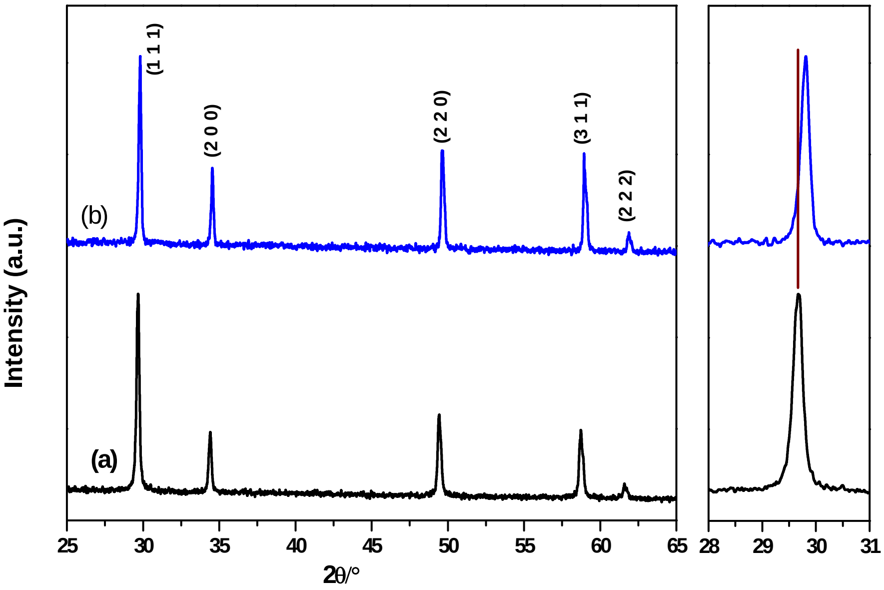

Fig. 6.3: Room temperature powder X-ray diffraction patterns of 0.8 YSZ–0.2 PuO_2 sample: (a) prepared in vacuum (b) after oxidation in oxygen

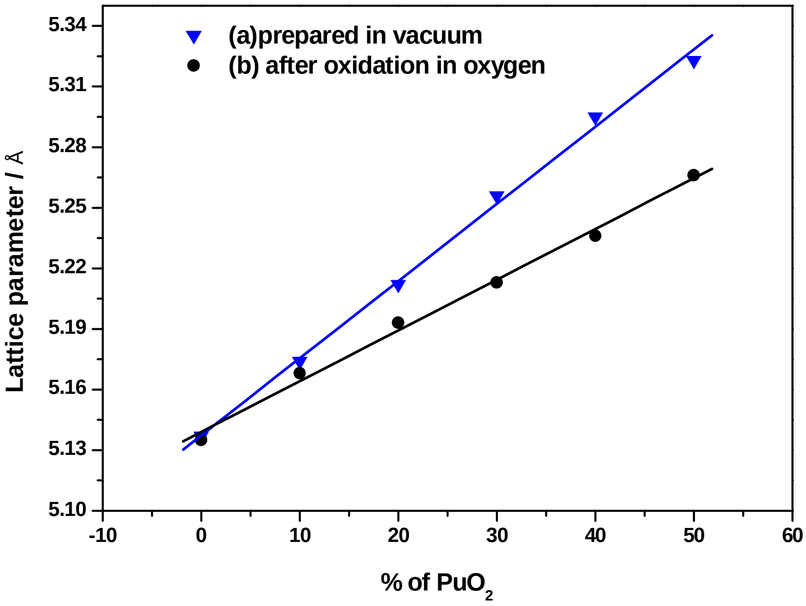

Fig. 6.4: Variation of lattice parameter as a function of PuO_2 mole fraction in $(YSZ)_{1-x}(PuO_2)_x$ $(0.0 \leq x \leq 0.5)$ system (a) prepared in vacuum and (b) after oxidation in oxygen

The biphasic mixture of PuO_2 and bcc α-Pu_2O_3 obtained from pure PuO_2 composition under vacuum also gets converted to single phasic F-type PuO_2 upon oxidation demonstrating that all Pu^{3+} has been converted to Pu^{4+}. The conversion of larger size Pu^{3+} to smaller size Pu^{4+} reduces the lattice parameter which reflects in the shift of diffraction pattern towards higher angle as observed. This change in phase relation observed under oxidising condition is the direct evidence of existence of Pu^{3+} in vacuum heated samples. However, Yamashita et al. [143] observed only F-type phase in YSZ–PuO_2 system under oxidising heating condition.

The XRD patterns for all the phases and their oxidation products have been refined using DICVOL06 program associated with Full Prof-2011 [144] and their lattice parameters have been determined. Table 6.1 lists the phases observed for different nominal compositions along with the lattice parameter values. Fig. 6.4 shows that the variation of lattice parameter with composition follows an ideal Vegard's law type behaviour indicating that the lattice parameters are governed primarily by relative ionic radii of the host and guest cations. It must be noted that the lattice parameters of pyrochlore-type solid solutions have been halved to compare with the fluorite-type phases. Pyrochlore structure is an ordered derivative of the fluorite structure possessing double the lattice parameter (of corresponding fluorite structure) and dividing their lattice parameters by two provides ready reference for comparison.

6.3.1.2. ZrO_2–PuO_2 system

Only two compositions $Zr_{0.8}Pu_{0.2}O_2$ and $Zr_{0.5}Pu_{0.5}O_2$ in ZrO_2–PuO_2 system have been studied in the present investigation. The XRD pattern for the composition $Zr_{0.8}Pu_{0.2}O_{2-x}$ and $Zr_{0.5}Pu_{0.5}O_{2-x}$ synthesized under reduced condition followed by heating under oxidising condition is presented in Fig. 6.5 and 6.6, respectively. The Fig. 6.5(a) shows the presence of primarily F-type cubic phase for the reduced $Zr_{0.8}Pu_{0.2}O_{2-x}$ which on oxidation transformed to tetragonal phase (Fig. 6.5(b)). Similarly, Fig. 6.6(a) shows the presence of pyrochlore phase along with minor amount of plutonium rich F-type phase for the reduced $Zr_{0.5}Pu_{0.5}O_{2-x}$.

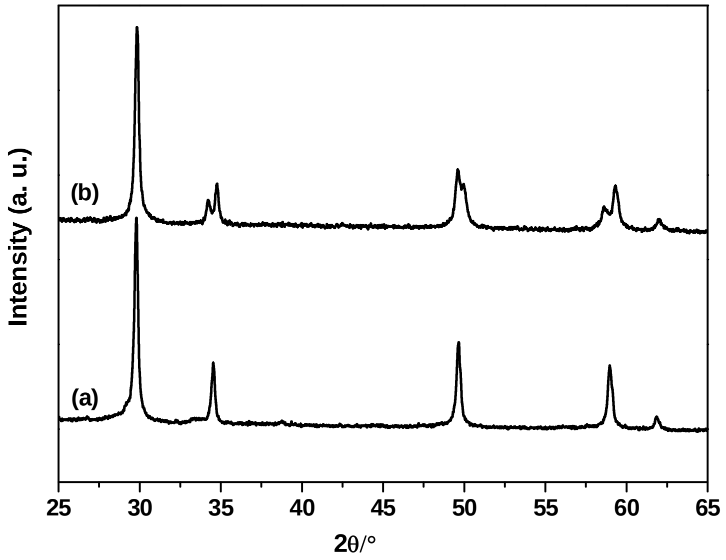

Fig. 6.5: XRD patterns of $Zr_{0.8}Pu_{0.2}O_2$ composition: (a) heated in Ar–8% H_2 and (b) after oxidation in oxygen

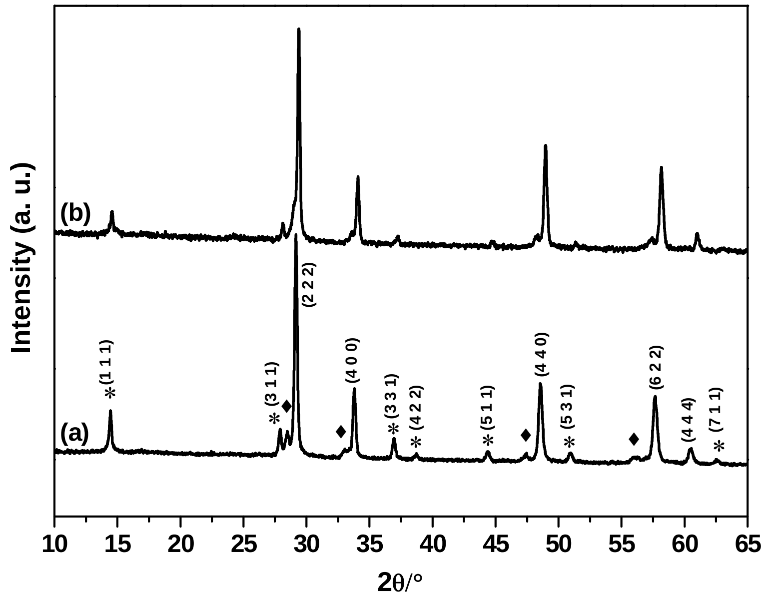

Fig. 6.6: XRD patterns of $Zr_{0.5}Pu_{0.5}O_2$ composition: (a) heated in Ar–8% H_2 and (b) after oxidation in oxygen. (*: superstructure reflection of pyrochlore phase and ♦: F-type phase containing PuO_{2-x})

The peaks marked as asterisk (*) represent the superstructure reflection of the pyrochlore phase. The peaks marked as (♦) represent plutonium rich F-type oxide phase. Upon oxidation, though the superstructure peaks still exist, the intensity decreases significantly and the diffraction pattern shifts towards higher angle as shown in Fig. 6.6(a) and (b). The F-type (minor amount) phase also shows a shift towards higher angle. The results are discussed here with reference to phase relation in ZrO_2–CeO_2 [130] (CeO_2 is surrogate of PuO_2) and ZrO_2–PuO_2 [145-147] systems. There is discrepancy in the available literature on ZrO_2–PuO_2 system. According to Carroll et al. [146], the composition $Zr_{0.8}Pu_{0.2}O_2$ should correspond to biphasic mixture of monoclinic ZrO_2 & cubic solid solution of $(Zr,Pu)O_2$ whereas the composition $Zr_{0.5}Pu_{0.5}O_2$ should exhibit cubic solid solution. Mardon et al. [147] have reported tetragonal phase for $Zr_{0.8}Pu_{0.2}O_2$ and a biphasic mixture of tetragonal and cubic phase for $Zr_{0.5}Pu_{0.5}O_2$. According to Albiol et al. [145], both the composition should exhibit a biphasic mixture of cubic and monoclinic phase. Grover et al. [130] have studied phase relation in ZrO_2–CeO_2 system under slow cooling conditions of the samples from 1673 K in static air. They have observed tetragonal phase for the composition $Zr_{0.8}Ce_{0.2}O_2$ and a biphasic mixture of cubic and tetragonal phase for the composition $Zr_{0.5}Ce_{0.5}O_2$. In the present case, the sample corresponding to the composition $Zr_{0.8}Pu_{0.2}O_2$ was heated at 1773 K in Ar–8% H_2 and hence there is very high probability of conversion of Pu^{4+} to Pu^{3+} resulting in creation of oxygen vacancies in the system to maintain electro-neutrality. The situation is very similar to system of ZrO_2 doped with 20 mol% trivalent cations like (Y^{3+}, Nd^{3+} etc.). Moreover, Pu^{3+} is larger in size compared to Y^{3+} [64]. This results in stabilization of monoclinic zirconia in F-type cubic phase due to the presence of Pu(III) oxide. Stabilization of monoclinic zirconia in cubic phase by trivalent cations like (Y^{3+}, Nd^{3+} etc.) is no surprise and has been discussed extensively in chapter 3. The oxidation of the product converts Pu^{3+} to Pu^{4+} and associated oxygen uptake takes place. The XRD pattern indicates tetragonal phase for the oxidised product. This is in conformity with the results obtained by Grover et al. [130] who have observed tetragonal phase for the composition $Zr_{0.8}Ce_{0.2}O_2$ for the sample heated in static air. These results also provide validity to the use of CeO_2 as a surrogate for phase studies in PuO_2-based systems. This structural modification is the manifestation of the fact that larger tetravalent cation (as compared to Zr^{4+}) cannot bring cubic stabilization in zirconia because in addition to size requirement, substitution by an aliovalent ion (Y^{3+}, Nd^{3+}, any trivalent lanthanides or Pu^{3+} leading to oxygen vacancies) is also required for this stabilization. The entropy associated with oxygen vacancies is an aid to obtain cubic stabilized zirconia. It must be noted that the lattice parameter for the reduced cubic $Zr_{0.8}Pu_{0.2}O_{2-x}$ is 5.191 Å and for oxidised tetragonal $Zr_{0.8}Pu_{0.2}O_2$ phase it is found to be a = 3.645 Å & c = 5.23 Å. The composition of oxidised product has been confirmed by chemical analysis of plutonium in the sample following the procedure given by Drummond and Grant [148]. The experimental result is found to be 31.86 wt. %, which corresponds to the nominal composition $Zr_{0.8}Pu_{0.2}O_2$. Similarly, when the sample corresponding to the composition $Zr_{0.5}Pu_{0.5}O_2$ is heated at 1773 K in Ar–8% H_2, reduction of Pu^{4+} to Pu^{3+} takes place which leads to oxygen vacancies in the lattice. The resulting phase is pyrochlore characterized by superstructure reflections (marked as * in Fig 6.6(a)) along with diffraction lines corresponding to minor F-type phase. The superstructure peaks are the result of ordering of cations and anions in the lattice. This can be explained by invoking the concept of r_A/r_B ratio in $A_2B_2O_7$ type pyrochlore as discussed in the previous section. In the present case, r_A/r_B ratio will be approximately 1.53-1.57 (radius of Pu^{3+} in eight coordination is unavailable and was estimated to be 1.10-1.13 Å by Perriot et al. [149]). This justifies formation of pyrochlore phase for the composition $Zr_{0.5}Pu_{0.5}O_{2-x}$. The relatively lower concentration of Pu for the composition $Zr_{0.8}Pu_{0.2}O_{2-x}$ is responsible for not observing ordering in the diffraction pattern and only stabilized fluorite phase is observed. A small fraction of F-type phase containing

PuO_{2-x} could also be ascribed to inhomogeneities caused by absence of intermittent grinding in a solid state synthesis. Upon oxidation, though the pyrochlore phase is retained, the intensity of the superstructure peaks decreases significantly indicating an ensuing structural transformation from pyrochlore to F-type phase. Also, the diffraction pattern shifts towards higher angle due to conversion of larger size Pu^{3+} to smaller size Pu^{4+}. The F-type (minor amount) phase also shows a shift towards higher angle due to the same reason. Kulkarni et al. [150] obtained pyrochlore phase for the composition $Zr_{0.5}Pu_{0.5}O_{1.75}$ after carbothermic reduction of ZrO_2, PuO_2 and graphite mixture in flowing gas. They have reported a lattice parameter of 10.592 Å for the pyrochlore ($Pu_2Zr_2O_7$) phase. Vaudez et al. [151] have predicted lattice parameter of 10.69 Å for $Pu_2Zr_2O_7$ phase theoretically while they obtained a value of 10.62 Å experimentally for the same phase. They explained this difference on the basis of slight oxygen uptake in pyrochlore phase i.e. formation of $Pu_2Zr_2O_{7+x}$. In the present case, the lattice parameter is found to be 10.639 Å immediately after reduction and 10.587 Å after several days of preparation. This decrease could be attributed to possible aerial oxidation in the sample. The lattice parameter for the oxidised sample is 10.514 Å. Kulkarni et al. [150] reported a lattice parameter of 10.54 Å for the oxidised pyrochlore $Pu_2Zr_2O_8$. The results clearly indicate any trivalent actinide or any actinide which can be reduced to trivalent state can form cubic phase (F-type or pyrochlore) with ZrO_2 if present in 20–50 mol% range.

6.3.1.3. Behaviour of PuO_2 under different environment:

In order to understand the redox response of plutonium and its implication on phase relation in plutonium based oxide systems, pure PuO_2 was also subjected to heat treatments under different atmosphere as depicted in Fig. 6.7 and discussed here. PuO_2 when heated under dynamic vacuum at 1773 K, a biphasic mixture of PuO_2 and bcc α-Pu_2O_3 is observed. This is due to partial reduction of Pu^{4+} to Pu^{3+} at high temperature in presence of vacuum. Observation of a biphasic phase field consisting of F-type PuO_2 and bcc α-Pu_2O_3 upon heat treatment of PuO_2 in non-oxidizing atmospheres has been reported earlier as well [152]. The reduction of PuO_2 at high temperature in presence of Ar–8% H_2 leads to the formation of hexagonal Pu_2O_3 along with minor amount of bcc α-Pu_2O_3 phase as detected by XRD. This indicates that while vacuum promotes partial reduction of Pu(IV) in PuO_2, complete reduction of Pu(IV) to Pu(III) is observed with Ar–8% H_2 at the same reaction temperature (1773 K) and for same time duration (12 hrs). It was also observed that complete reduction of PuO_2 could be achieved by carbon at the same temperature in vacuum. Here also, hexagonal phase of Pu_2O_3 along with minor amount of bcc α-Pu_2O_3 phase was detected by XRD. All the reduced products upon oxidation lead to F-type cubic phase of PuO_2.

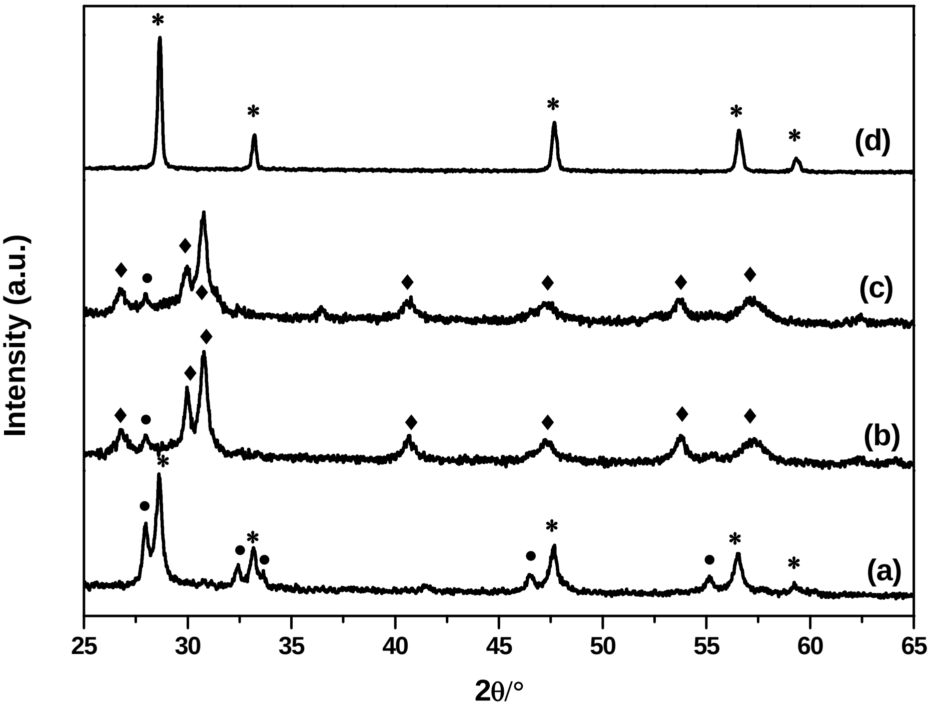

Fig. 6.7: Room temperature powder X-ray diffraction patterns of PuO_2 sample heated in (a) vacuum, (b) Ar-8% H_2 (c) PuO_2+C heated in vacuum and (d) oxidation product of reduced PuO_2; (*: F- type PuO_2, ●: bcc Pu_2O_3 and ♦: hexagonal Pu_2O_3)

6.3.2. Thermo-physical property studies

Thermo-physical properties, such as sintering behaviour and thermal expansion on selected compositions in $(YSZ)_{1-x}(PuO_2)_x$ ($0.0 \leq x \leq 0.5$) series have been carried out. The sintering studies have been carried out on green compact and expansion studies have been carried out on samples sintered at 1773 K in vacuum followed by oxidation in oxygen at 1173 K to reach oxygen to metal ratio in PuO_2 close to 2.00. The relative densities of the green compacts and sintered samples in YSZ–PuO_2 samples are given in Table 6.2.

6.3.2.1. Sintering studies

The results of the sintering studies on YSZ–PuO_2 samples are presented in this section. The % length change of the green compacts as a function of temperature is shown in Fig. 6.8. The following observations could be noted from these results: (a) onset of sintering temperature decreases with increasing amount of PuO_2, (b) percentage shrinkage decreases with increasing PuO_2 content (c) rate of shrinkage decreases with increasing PuO_2 content. In all the cases, it was observed that there is a small change in the length of green compacts beyond 1773 K. Hence, the studies indicate 1773 K may be the sintering temperature in YSZ–PuO_2 system.

6.3.2.1. Thermal expansion studies

The percentage linear expansion of $(YSZ)_{1-x}(PuO_2)_x$ samples (x = 0.0 and 0.4) measured in a vertical dilatometer in the temperature range 450–1673 K are presented in Fig. 6.9. The length at room temperature of the pellet corresponding to the composition x = 0.0 and 0.4 is 3.73 mm and 4.06 mm respectively. The observed linear thermal expansions (%) have been fitted to the function of temperature using a polynomial regression. The results are as follows (T in K, in the range 450–1673 K).

YSZ

$$100 \text{ x } \frac{\Delta L}{L} = - 0.416 + 0.00111 \text{ T} + 4.0044 \text{ x } 10^{-8} \text{ T}^2 \qquad (6.1)$$

Table 6.2: Typical values of green pellet density, density after shrinkage study and sintered density of various $(YSZ)_{1-x}(PuO_2)_x$ (x = 0.0, 0.2 and 0.4) samples

Sample	**Type of pellet**	**Measured density (g/cc)**	**Theoretical density (g/cc)**	**% TD**
YSZ	Green pellet	2.81	5.96	47
	Pellet after shrinkage study	5.29	5.96	89
	Sintered pellet	5.62	5.96	94
0.8 YSZ - 0.2 PuO_2	Green pellet	3.70	7.11	52
	Pellet after shrinkage study	5.94	7.11	84
	Sintered pellet	6.19	7.11	87
0.6 YSZ - 0.4 PuO_2	Green pellet	4.30	8.12	53
	Pellet after shrinkage study	6.52	8.12	80
	Sintered pellet	6.71	8.12	83

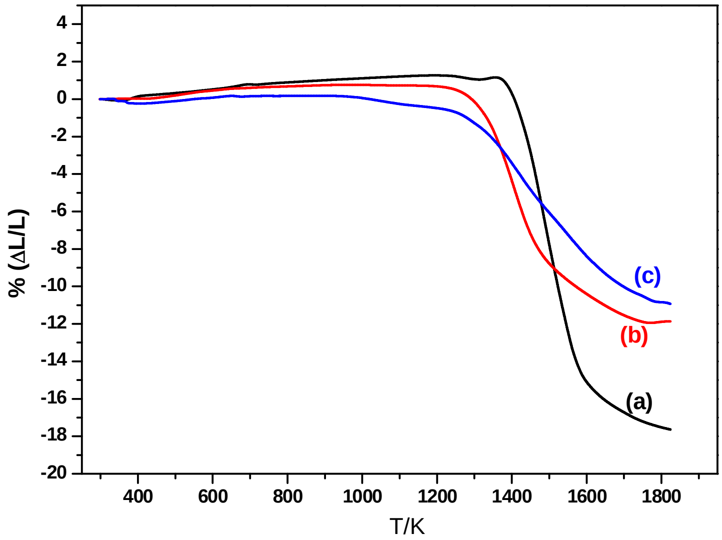

Fig. 6.8: Shrinkage curves for the $(YSZ)_{1-x}(PuO_2)_x$ pellets: (a) x = 0.0, (b) x = 0.2 and (c) x = 0.4 in Ar atmosphere

0.6YSZ–0.4PuO$_2$

$$100 \times \frac{\Delta L}{L} = -\,0.34526 + 9.36549 \times 10^{-4}\,T - 1.27085 \times 10^{-7}\,T^2 \qquad (6.2)$$

The calculated average linear thermal expansion coefficient using equation 2.4 for the two compositions as a function of temperature is plotted in Fig. 6.10 which shows that the thermal expansion coefficients of YSZ (x = 0.0) and 40 mol% PuO$_2$ doped YSZ (x = 0.4) increase with increase in temperature. The figure also reveals that the coefficients of linear thermal expansion of 0.6YSZ–0.4PuO$_2$ (x = 0.4) is lower as compared to YSZ below 1473 K and it becomes higher beyond 1473 K. The higher thermal expansion coefficient of 0.6YSZ–0.4PuO$_2$ (x = 0.4) compared to pure YSZ beyond 1473 K can be explained on the basis of formation of sub-stoichiometric PuO$_2$ due to oxygen loss upon heating in Ar atmosphere during the experiment beyond this temperature. The oxygen loss is associated with the formation of Pu^{3+} from Pu^{4+} which weakens Pu–O bond strength. The obvious result is increase in thermal expansion. Kato et al. [153] have showed that thermal expansion of hypo stoichiometric PuO$_2$ is higher than that of stoichiometric PuO$_2$. In the present investigation, the thermal expansion coefficient of pure YSZ is found to be 10.94 x 10^{-6} K^{-1} in the temperature range RT–1273 K. Yamashita et al. [143] have reported a lattice thermal expansion coefficient of 11.75 x 10^{-6} K^{-1} in the same temperature range. Generally, lattice thermal expansion coefficient is somewhat higher compared to bulk thermal expansion when the sample used for bulk thermal expansion contains porosity and hence both the results are in good agreement with each other. Kato et al. [153] and Tokar et al. [154] have reported thermal expansion coefficient of 10.65 x 10^{-6} K^{-1} and 10.56 x 10^{-6} K^{-1} for PuO$_2$ sample in the temperature range RT–1273 K. Based on these data, it is expected that the thermal expansion coefficient of 0.6YSZ–0.4PuO$_2$ (x = 0.4) sample will be somewhat lower as compared to pure YSZ. The present study also confirms the same.

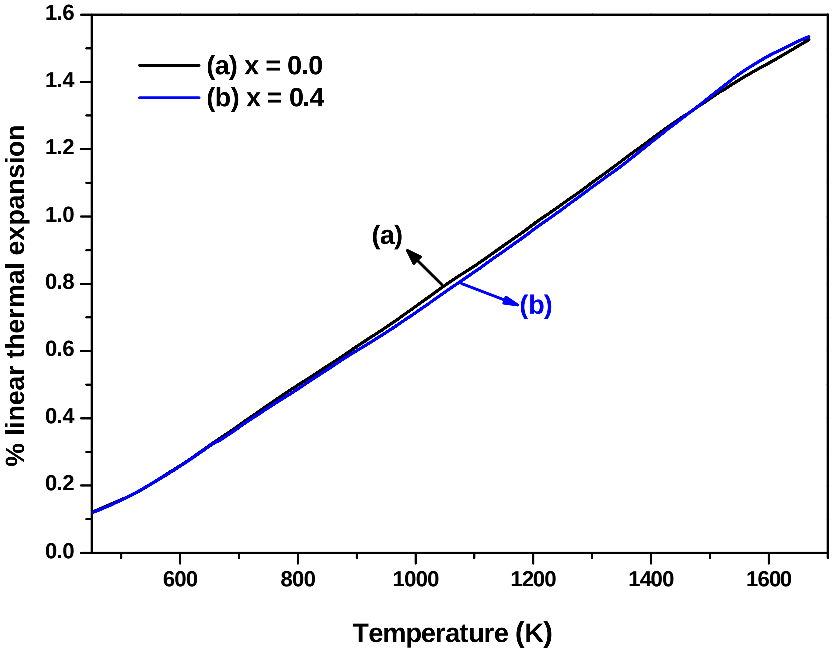

Fig. 6.9: Bulk thermal expansion (%) as a function of temperature for the composition $(YSZ)_{1-x}(PuO_2)_x$ ($0.0 \leq x \leq 0.5$): (a) x = 0.0 and (b) x = 0.4

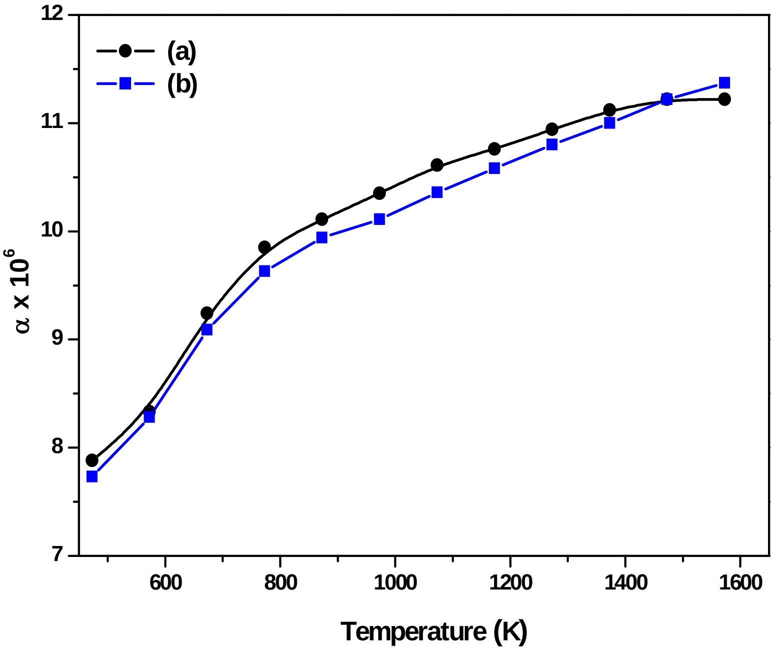

Fig. 6.10: Bulk thermal expansion coefficient as a function of temperature for the composition $(YSZ)_{1-x}(PuO_2)_x$ ($0.0 \leq x \leq 0.5$): (a) x = 0.0 and (b) x = 0.4

The thermal expansion coefficient of 0.6YSZ–0.4PuO_2 ($x = 0.4$) sample is found to be 10.80 x 10^{-6} K^{-1} in the temperature range RT−1273 K.

6.4. Conclusion

Phase relations in YSZ–PuO_2 under vacuum heating condition show existence of fluorite type and pyrochlore type phase field. Formation of pyrochlore phase field is attributed to partial reduction of Pu (IV) to Pu (III) which is also confirmed by conversion of PuO_2 to bcc Pu_2O_3 phase when it is heated under vacuum conditions. Though vacuum heating conditions partially reduce PuO_2, complete reduction of PuO_2 to Pu_2O_3 is possible with Ar–8% H_2. Though the phase relation remains same upon oxidation, the intensity of the superstructure reflection of pyrochlore phase decreases indicating pyrochlore to fluorite type phase transformation attributed to oxidation of Pu (III) back to Pu (IV). 20 and 50 mol% Pu substituted ZrO_2 under reduced condition (Ar–8 % H_2) exhibit fluorite and pyrochlore phase, respectively. The F-type phase upon oxidation transformed to tetragonal phase while the pyrochlore phase retains its identity. Transformation of F-type phase to tetragonal phase highlights role of vacancies (created due to reduction of Pu(IV) to Pu(III)) in stabilizing F-type phase. The sintering studies revealed that 1773 K may be used as the sintering temperature for YSZ–PuO_2 compacts. The thermal expansion studies show that though the coefficients of linear thermal expansion of 0.6YSZ–0.4PuO_2 (40 mol% PuO_2 containing YSZ) is lower compared to that of YSZ ($x = 0.0$) at lower temperature, the trend reverses beyond 1473 K.

CHAPTER 7

Investigation of radiation tolerance of stabilized zirconia and its composite under swift heavy ion irradiation

7.1. Introduction

As discussed in the introduction chapter, response of transmutation targets to radiation is an important property for its qualification as nuclear fuel. During the in pile performance of the fuel, the fuel matrix is expected to be exposed to neutrons, fission fragments (FF), α-particles and α-recoils produced in the reactor environment. All these components deposit energy into the fuel matrix by the mechanisms which depend not only on the particles but also their energies and the atomic number (Z) of the target among other parameters. The FFs, for example, on passing through the solids interact with the target electrons and lose energy either by ionization or excitation of target atoms and get slowed down [155]. They deposit a high density of energy within narrow cylindrical volumes around the ion path (called tracks), causing large pressure and temperature rise transiently, which may result in structural transformations in the track region [155, 156]. The track regions may contain various lattice defects [157, 158] and may also undergo a transition to a different crystalline phase [155] or could even suffer amorphization [156, 159]. These structural changes are important to study from the point of view of structural stability of the fuel matrix. The effect of FF on the matrices can be simulated by irradiating them with swift heavy ions (SHI) with masses and energies similar to that of FF. The FFs generally are the ions having mass number 70-160 with energies in the range of 70-110 MeV [156]. The swift heavy ions thus provide valuable means to simulate the accelerated damage on the proposed inert matrices imparted due to fission fragments. The present study employs 120 MeV Au ions as swift heavy ions (SHI) produced in accelerator to simulate radiation damage effects in zirconia based oxides. This chapter describes synthesis and characterization of

$Zr_{0.80}Nd_{0.20}O_{1.90}$, $Zr_{0.80}Nd_{0.20}O_{1.90}$–MgO (50 wt.%) composite and $Zr_{0.80}Nd_{0.10}Y_{0.10}O_{1.90}$ nominal compositions as well as the structural evolution (deterioration) of these compositions when irradiated with 120 MeV Au ions as a function of fluence. The reasons for choosing these matrices are justified as follows. The composition $Zr_{0.80}Nd_{0.20}O_{1.90}$ represents 20 mol% minor actinide doped zirconia (Nd_2O_3 as surrogate for Am_2O_3 and Cm_2O_3). The Nd substituted zirconium oxides possess relatively lower thermal conductivity which has to be overcome because the proposed fuel matrix should have good thermal conductivity. In order to circumvent this problem, research has been directed to composites of these matrices with another compound with better thermal conductivity such as MgO [41, 160]. Thus, in order to investigate the effect of fission fragments on composites, $Zr_{0.80}Nd_{0.20}O_{1.90}$–MgO (50 wt.%) composite has also been subjected to similar irradiation experiments. In addition, the effect of co-doping of two trivalent ions (Nd^{3+} and Y^{3+}) in ZrO_2 on its radiation tolerance is also investigated in order to mimic doping of minor actinides in Y^{3+} doped zirconia matrix (Nd as surrogate for Am and Cm) in order to extend cubic phase field as discussed in chapter 4.

7.2. Experimental

The nominal composition $Zr_{0.80}Nd_{0.20}O_{1.90}$ and $Zr_{0.80}Nd_{0.10}Y_{0.10}O_{1.90}$ have been prepared by gel combustion route. The powders so obtained after combustion synthesis have been pelletized and sintered at 1723 K. The $Zr_{0.80}Nd_{0.20}O_{1.90}$–MgO composite has been prepared by conventional solid state route employing MgO (AR Grade) powder and phase pure $Zr_{0.80}Nd_{0.20}O_{1.90}$ powder prepared by gel combustion. The sintering has been carried out at 1723 K in static air to produce pellets of 10 mm diameter and 2 mm thickness in all cases. The samples have been thoroughly characterized by XRD, SEM, EDS and XANES spectroscopy. The as-sintered pellets have been irradiated at ambient temperature with 120

MeV Au^{9+} ions at various fluences ranging from 1 x 10^{12} to 1 x 10^{14} ions/cm^2 using the 15UD Pelletron accelerator facility at the Inter-University Accelerator Centre (IUAC), New Delhi. The structural modification of the samples upon irradiation has been monitored using *in situ* X-ray diffraction (XRD). The X-ray absorption near edge spectroscopic (XANES) study has been carried out to probe the local structure surrounding the Zr and Nd ions in the materials under investigation. The measurements were carried out at the Energy Scanning EXAFS beamline (BL-09) in the fluorescence mode at the INDUS-2 Synchrotron Source (2.5 GeV, 120 mA) at the Raja Ramanna Centre for Advanced Technology (RRCAT), Indore, India.

7.3. Results and discussion

7.3.1. Characterization of un-irradiated samples

The XRD patterns for the compositions $Zr_{0.80}Nd_{0.20}O_{1.90}$, $Zr_{0.80}Nd_{0.20}O_{1.90}$–MgO (50 wt.%) and $Zr_{0.80}Nd_{0.10}Y_{0.10}O_{1.90}$ are shown in Fig. 7.1. $Zr_{0.80}Nd_{0.20}O_{1.90}$ is found to form fluorite type cubic phase. For the composition $Zr_{0.80}Nd_{0.20}O_{1.90}$–MgO (50 wt.%), a biphasic mixture of cubic MgO and fluorite type cubic $Zr_{0.80}Nd_{0.20}O_{1.90}$ phase is observed. Interestingly, a shift towards higher angle is observed for the corresponding peaks of $Zr_{0.80}Nd_{0.20}O_{1.90}$ phase in the composite (relative to single-phasic $Zr_{0.80}Nd_{0.20}O_{1.90}$) indicating the shrinkage of the lattice. This can be attributed to possible incorporation of some Mg^{2+} ion and associated vacancies in the lattice of cubic $Zr_{0.80}Nd_{0.20}O_{1.90}$. The ionic radii of Zr^{4+}, Nd^{3+} and Mg^{2+} in eight-fold coordination are 0.84, 1.109 and 0.89 Å, respectively [64]. The average cationic radii in $Zr_{0.80}Nd_{0.20}O_{1.90}$ lattice is calculated based on these data and found to be 0.89 Å in eight-fold coordination. The incorporation of same size Mg^{2+} in lattice, thus, does not lead to change in cell parameter but the associated introduction of vacancies would lead to contraction of lattice. The diffraction lines of MgO phase match well with the JCPDS card no. 87-0653. $Zr_{0.80}Nd_{0.10}Y_{0.10}O_{1.90}$ is also found to crystallize in fluorite-type cubic phase like $Zr_{0.80}Nd_{0.20}O_{1.90}$ with a concomitant shift in XRD patterns to higher 2θ values.

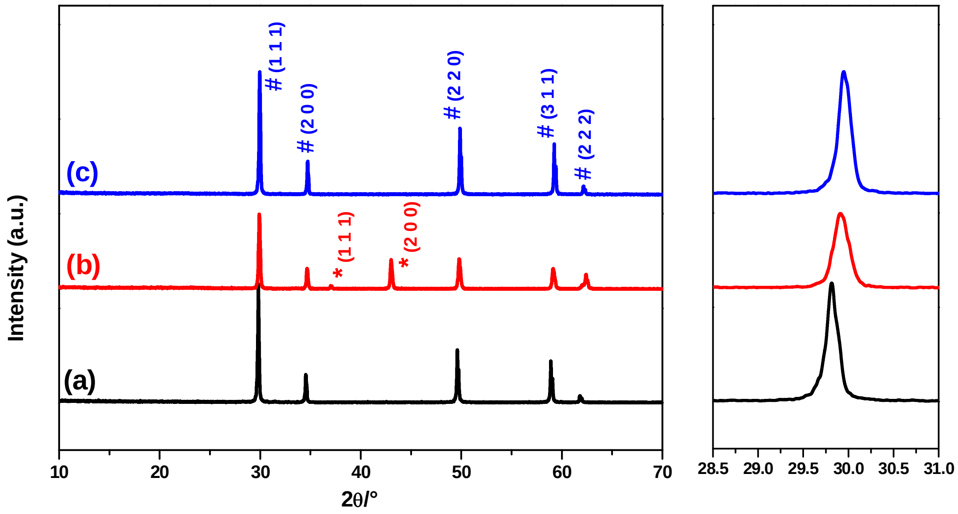

Fig. 7.1: XRD patterns of unirradiated samples: (a) $Zr_{0.80}Nd_{0.20}O_{1.90}$, (b) $Zr_{0.80}Nd_{0.20}O_{1.90}$–MgO (50 wt.%) composite and (c) $Zr_{0.80}Nd_{0.10}Y_{0.10}O_{1.90}$ (# represents F type peak for $Zr_{0.80}Nd_{0.20}O_{1.90}$ and $Zr_{0.80}Nd_{0.10}Y_{0.10}O_{1.90}$ and * represents peak for cubic MgO)

Table 7.1: Phases present in the samples and their lattice parameters; #: Lattice parameter not refined

Composition	**Phases**	**Lattice parameter (Å)**
$Zr_{0.80}Nd_{0.20}O_{1.90}$	Fluorite	5.193(3)
$Zr_{0.80}Nd_{0.20}O_{1.9}$–MgO (50 wt.%)	Fluorite ($Zr_{0.8}Nd_{0.2}O_{1.9}$)	5.175(3)
	Rock salt (MgO)	#
$Zr_{0.80}Nd_{0.10}Y_{0.10}O_{1.9}$	Fluorite	5.167(2)

This indicates the shrinkage of fluorite-type cubic phase upon substitution of Nd^{3+} by Y^{3+}. The decrease in lattice parameter can again be explained on the basis of the relative ionic radii of guest and host ions [64]. The XRD patterns for all the three compositions have been refined using POWDERX software and their cell parameters have been determined. The phases present and the corresponding lattice parameters are listed in Table 7.1. The FWHM for (111) peak for the compositions $Zr_{0.80}Nd_{0.20}O_{1.90}$, $Zr_{0.80}Nd_{0.20}O_{1.9}$–MgO (50 wt.%) and $Zr_{0.80}Nd_{0.10}Y_{0.10}O_{1.9}$ are 0.15°, 0.20°, 0.16°, respectively. These results clearly indicate relatively higher broadening of (111) peak for the composite $Zr_{0.80}Nd_{0.20}O_{1.90}$–MgO (50 wt.%). This could be due to lattice strain introduced by the incorporation of aliovalent Mg^{2+} in the lattice. It may be noted that substitution of Nd^{3+} by Y^{3+} does not lead to any appreciable broadening as they have similar charge and are expected to form simple substitutional solid solution. The present experimental XRD data is not adequate to determine the solubility of Mg^{2+} in $Zr_{0.80}Nd_{0.20}O_{1.90}$.

In order to carry out compositional analysis, to determine the true compositions of the products, SEM analysis coupled with EDS has been performed on the unirradiated samples. The BSE micrographs of all the three compositions are shown in Fig. 7.2. From the micrographs, it is evident that $Zr_{0.80}Nd_{0.20}O_{1.90}$ (Fig. 7.2(a)) and $Zr_{0.80}Nd_{0.10}Y_{0.10}O_{1.90}$ (Fig. 7.2(c)) show single-phasic microstructures, whereas bi-phasic microstructure is observed in the case of $Zr_{0.80}Nd_{0.20}O_{1.90}$–MgO (50 wt.%) composite (Fig. 7.2(b)). Reasonable open porosity could also be observed in these micrographs. The overall compositions of the product grains, as obtained by EDS analysis, for $Zr_{0.80}Nd_{0.20}O_{1.90}$ and $Zr_{0.80}Nd_{0.10}Y_{0.10}O_{1.90}$ are in excellent agreement with the assigned nominal compositions. It may be noted that in each case the overall composition is measured over a sample surface of ~1 mm^2 area in different positions and hence the obtained values reflect bulk average (overall) compositions.

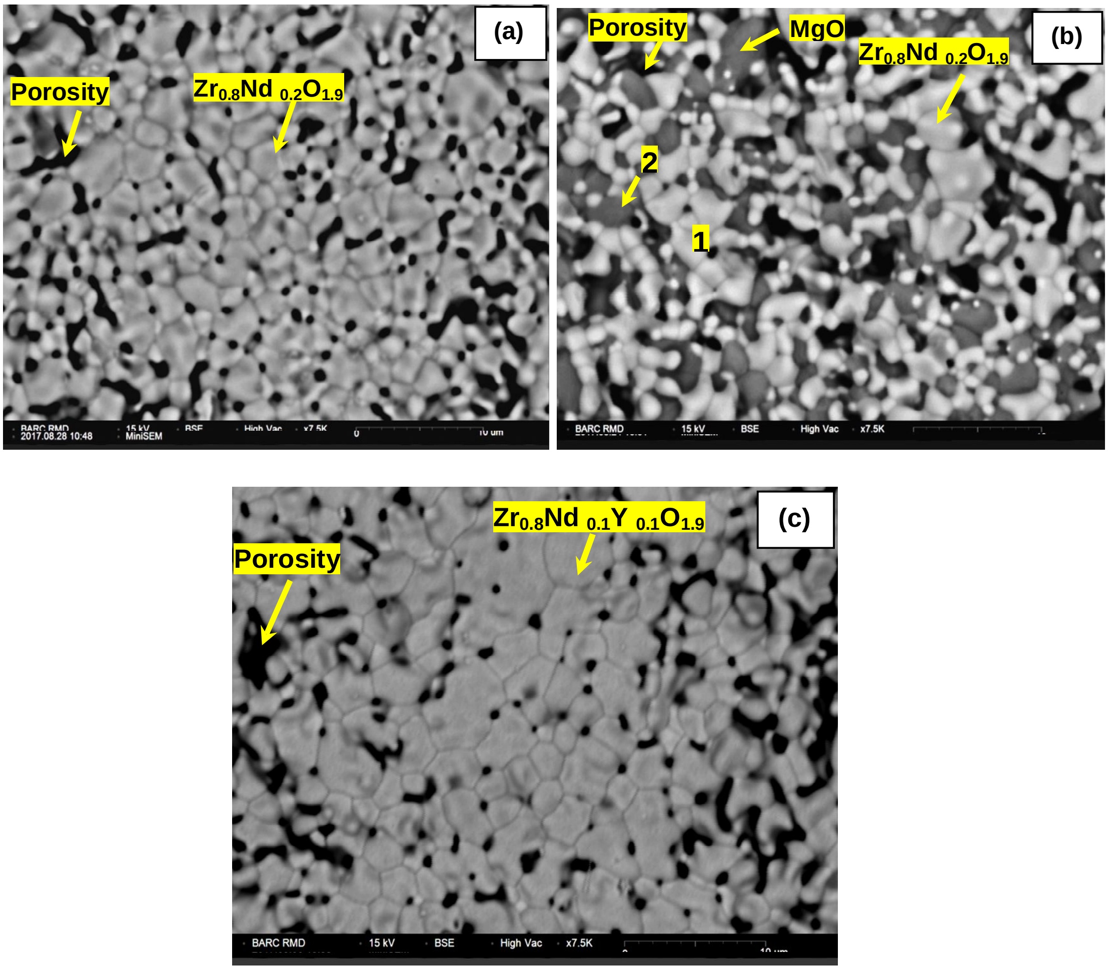

Fig. 7.2: BSE images of unirradiated samples: (a) $Zr_{0.80}Nd_{0.20}O_{1.90}$ (b) $Zr_{0.80}Nd_{0.20}O_{1.90}$ –MgO (50 wt.%) composite and (c) $Zr_{0.80}Nd_{0.10}Y_{0.10}O_{1.90}$

Table 7.2: Composition analysis of unirradiated samples by EDS

Composition	Zr (at. %)	Nd (at.%)	Y (at.%)	Mg (at.%)
$Zr_{0.80}Nd_{0.20}O_{1.90}$	79 (overall)	21 (overall)	-	-
$Zr_{0.80}Nd_{0.20}O_{1.90}$–MgO (50 wt.%)	74 (spot-1) 3 (spot-2)	17 (spot 1) 1 (spot 2)	-	9 (spot-1) 96 (spot-2)
$Zr_{0.80}Nd_{0.10}Y_{0.10}O_{1.90}$	79 (overall)	11 (overall)	10 (overall)	-

The EDS analysis is also performed on $Zr_{0.80}Nd_{0.20}O_{1.90}$ phase and MgO phase in the bi-phasic $Zr_{0.80}Nd_{0.20}O_{1.90}$–MgO (50 wt.%) composite (Fig. 7.2(d)). The analysis shows 9 mol % incorporation of Mg^{2+} in $Zr_{0.80}Nd_{0.20}O_{1.90}$ phase (Zr:Nd:Mg = 0.74:0.17:0.09 in $Zr_{0.80}Nd_{0.20}O_{1.90}$ phase as per EDS data). MgO oxide phase is found to contain 3 atom% Zr^{4+} and 1 atom% Nd^{3+}. The EDS analysis results are tabulated in Table 7.2.

The XANES spectra of Nd L_{III} edge corresponding to the three samples are shown in Fig. 7.3. All the samples show white line peak, which arises from L core to bound state transition (2p → 5d i.e. $^2P_{3/2} \rightarrow {}^2D_{5/2}$) of Nd^{3+} ions having electronic configuration as $1s^2 2s^2 2p^6 3s^2 3p^6 3d^{10} 4s^2 4p^6 4d^{10} 4f^3 5s^2 5p^6$ [161, 162]. This white line peak is observed at 6207.6 eV for all the three unirradiated samples and for Nd_2O_3 as well. The results suggest that the bonding nature of Nd^{3+} ions in the samples is essentially same as in Nd_2O_3 [161]. The observed value of Nd L_{III} edge for Nd_2O_3 is in accordance with literature data [161].

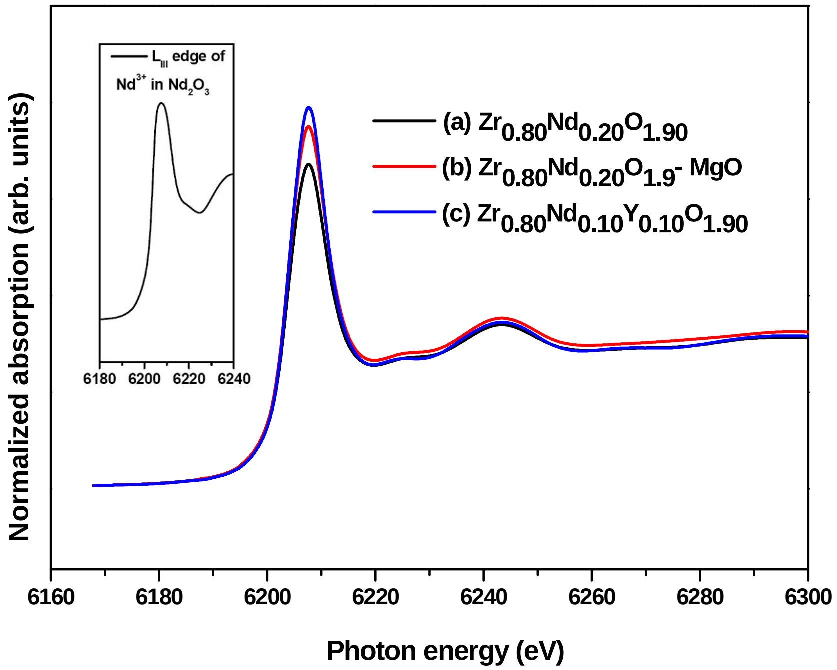

Fig. 7.3: Normalised XANES spectra for unirradiated samples at Nd L_{III} edge; (a) $Zr_{0.80}Nd_{0.20}O_{1.90}$ (b) $Zr_{0.80}Nd_{0.20}O_{1.90}$–MgO (50 wt.%) and (c) $Zr_{0.80}Nd_{0.10}Y_{0.10}O_{1.90}$; Nd L_{III} edge of Nd_2O_3 is shown as inset

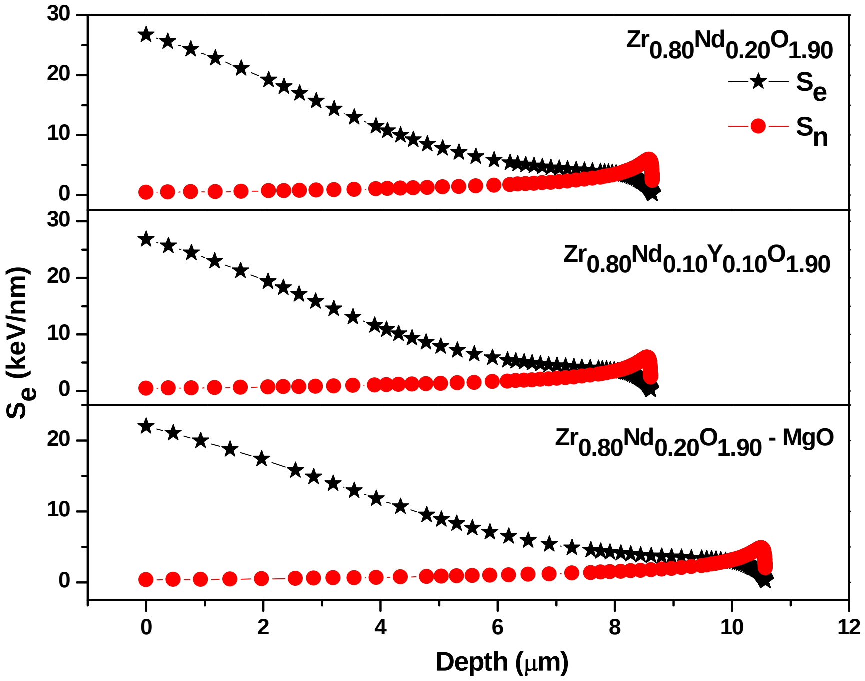

Fig. 7.4: Depth profile of electronic stopping power (S_e) and nuclear stopping power (S_n) of 120 MeV Au ions in (a) $Zr_{0.80}Nd_{0.20}O_{1.90}$ (b) $Zr_{0.80}Nd_{0.20}O_{1.90}$–MgO (50 wt.%) composite and (c) $Zr_{0.80}Nd_{0.10}Y_{0.10}O_{1.90}$ calculated by SRIM code [163]

Table 7.3: Ion projected range (R_p), nuclear (S_n) and electronic (S_e) stopping power calculated with the SRIM-2013 code [163] for 120 MeV Au^{+9} ions

Irradiated material	Ion range (R_p) μm	Electronic stopping power (S_e) in keV/nm	Nuclear stopping power (S_n) in keV/nm
$Zr_{0.80}Nd_{0.20}O_{1.90}$	8.65	26.7	0.45
$Zr_{0.80}Nd_{0.20}O_{1.90}$–MgO Composite (50 wt.%)	9.47	24.7	0.37
$Zr_{0.80}Nd_{0.10}Y_{0.10}O_{1.9}$	8.62	26.8	0.44

7.3.2. Radiation stability studies

The irradiation induced structural changes in the materials under investigation is discussed in this section. The electronic stopping powers (S_e) of the ion beams in all the three materials have been estimated using SRIM 2013 [163] and are tabulated in Table 7.3. A graphical representation of the same is shown in Fig. 7.4. The projected range of the 120 MeV Au^{9+} ions in these materials was found to be ~ 8.5 μm which is higher than probing depth of the X-ray and hence it can be inferred that XRD pattern is recorded from the irradiated region only. The structural modification of the samples upon irradiation has been monitored using *in situ* X-ray diffraction (XRD) [164]. It involves XRD characterization of the samples after each irradiation. *In situ* XRD patterns have been recorded in θ–θ geometry in the 2θ range of 20–65° using monochromatic Cu K_α radiation.

The *in situ* XRD patterns of $Zr_{0.80}Nd_{0.20}O_{1.90}$ as a function of fluence are shown in Fig. 7.5(a). No additional peaks with respect to unirradiated samples are found to appear with increasing the fluence (upto maximum fluence of 1 x 10^{14} ions/cm^2) employed in the experiments. These results confirm that the fluorite structure is retained under swift heavy irradiation which indicates excellent radiation stability of 20 mol % Nd^{3+} stabilized zirconia matrix. Even though the crystallinity is retained, several changes in diffraction patterns could be observed after irradiation at different fluences (Fig. 7.5(a) and (b)). These are (a) shift in diffraction maxima of fluorite-type structure to lower 2θ angle (b) peak broadening and (c) significant reduction in the intensity of the diffraction maxima with increasing fluence. The above mentioned observations are presented in Fig. 7.5(b). A plot of normalized I_{max} for (111) plane as a function of fluence is shown in Fig. 7.6. The peak shift towards lower 2θ angle indicates an increase in the average unit cell parameter. The intensity reduction suggests a decrease in the number of scattering atoms occupying the ideal fluorite structure atomic positions, resulting in a partial loss of coherent Bragg X-ray scattering. Both these effects are attributed to irradiation-induced defect accumulation and the accompanying structural distortions over long and short-range length scales, respectively [158]. It must be mentioned that though the maximum intensity decreases sharply with increasing ion fluences, the integrated intensity decreases marginally. This is a consequence of broadening of the diffraction peaks. The broadening may be ascribed to strain induced in the lattice due to irradiation displacement or particle size reduction. The existence of fluorite type diffraction peaks even at highest fluence (1 x 10^{14} ions/cm^2) for this compound is indicative of the fact that complete amorphization has not taken place even at this fluence. However, the accompanying morphological changes and formation of defect clusters (if occurring) could not be commented upon. Sickafus et al. [165] did not observe any amorphization in cubic-stabilized zirconia single crystals when irradiated using 72 MeV I^+ ion by TEM observations. To the best of our knowledge, there is no report in the literature on effect of 120 MeV Au^{9+} ions irradiation on $Zr_{0.80}Nd_{0.20}O_{1.90}$. Hence, the results have been compared with that of Patel et al. [156] and Sattonnay et al. [166] who have reported radiation stability of $Zr_{0.50}Nd_{0.50}O_{1.75}$ (pyrocholore structure) under 120 MeV Au^{9+} ions and 120 MeV U ions, respectively. Pyrochlore structure, $A_2B_2O_7$ (or $A_{0.5}B_{0.5}O_{1.75}$) is the superstructure of fluorite-type structure which involves ordering of A and B ions as well as oxygen anions and vacancies. Patel et al. have observed that the compound $Zr_{0.50}Nd_{0.50}O_{1.75}$ having pyrochlore structure undergoes phase transformation, when irradiated with 120 MeV Au^{9+} ions, from pyrochlore to defect fluorite and then complete amorphization at the fluence of 5 x 10^{13} ions/cm^2 [156]. Sattonnay et al. reported that in $Nd_2Zr_2O_7$, the diffraction peaks related to the supercell of the pyrochlore structure disappear at the ion fluence of 5 x 10^{12} ions/cm^2, upon irradiation with 120 MeV U ions, and only the peaks corresponding to the fluorite structure are observed indicating transformation from pyrochlore to defect fluorite phase. They observed complete amorphization of $Nd_2Zr_2O_7$ at the fluence of 4 x 10^{13} ions/cm^2.

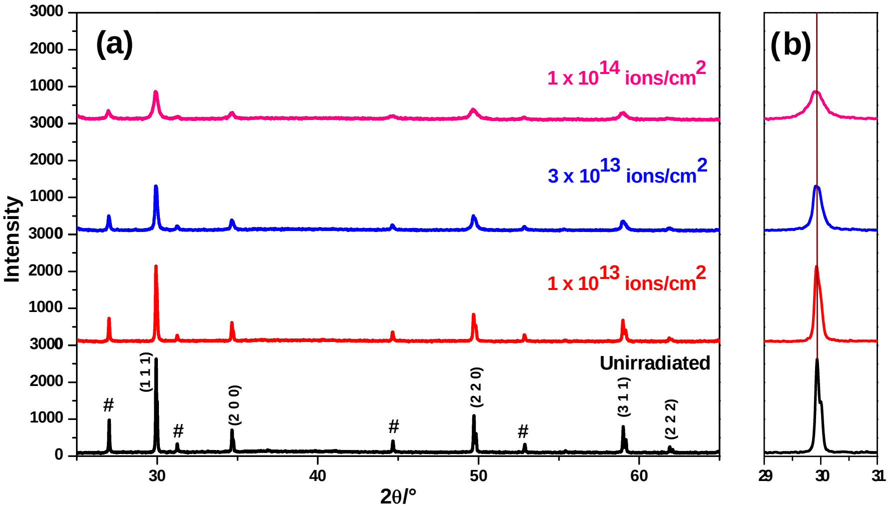

Fig. 7.5: (a) *In situ* XRD patterns of $Zr_{0.80}Nd_{0.20}O_{1.90}$ before and after irradiation with 120 MeV Au ions at different fluences, and (b) expanded view of (111) peak of $Zr_{0.80}Nd_{0.20}O_{1.90}$ with varying ion fluence. (#: peaks from sample support)

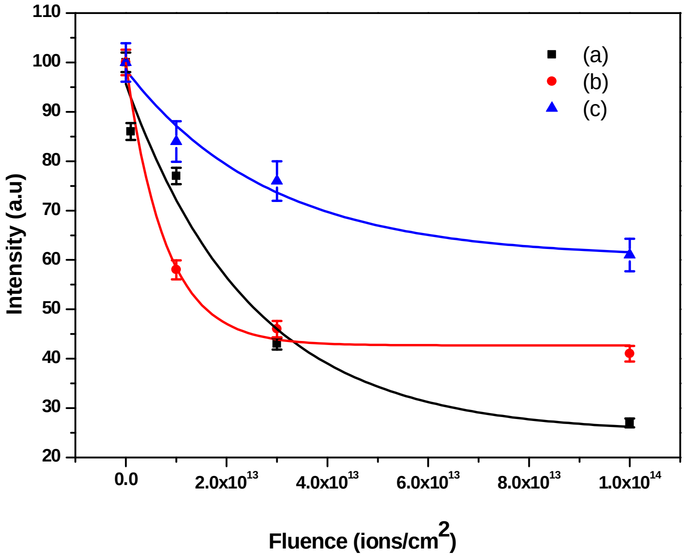

Fig. 7.6: Normalized intensity of the diffraction peak versus ion fluence for (a) (111) reflection of $Zr_{0.80}Nd_{0.20}O_{1.90}$ (b) (111) reflection of $Zr_{0.80}Nd_{0.20}O_{1.90}$ in $Zr_{0.80}Nd_{0.20}O_{1.90}$–MgO composite and (c) (200) reflection of MgO in $Zr_{0.80}Nd_{0.20}O_{1.90}$–MgO composite. The solid line represents fitting of the experimental data following eq. (7.1)

The present results point towards the retention of fluorite-type phase of $Zr_{0.80}Nd_{0.20}O_{1.90}$ upto the fluence 1 x 10^{14} ions/cm^2 indicating better irradiation behaviour of $Zr_{0.8}Nd_{0.2}O_{1.9}$ (defect fluorite) over $Zr_{0.50}Nd_{0.50}O_{1.75}$ (pyrochlore). It is known that Nd-Zr-O system proceeds from defect fluorite to pyrochlore upon subsequent incremental substitution of Nd^{3+} in ZrO_2. Initial substitution leads to stabilization of monoclinic zirconia into cubic modification and further increase leads to formation of pyrochlore-type micro-domains in a largely fluorite structure. This then gives way to an ordered pyrochlore structure. The reason for pyrochlore-type ordering is the relative radii of Nd^{3+} and Zr^{4+} ions. A stoichiometric composition containing 50 mol% of each of them favours Nd^{3+} and Zr^{4+} occupying distinct sites resulting in pyrochlore structure. 20 mol% Nd^{3+} is not sufficient to bring about three dimensional ordering and hence Nd^{3+} and Zr^{4+} randomise to yield disordered fluorite structure. Upon irradiation, a 50 mol% Nd^{3+} containing nominal composition i.e. $Nd_{0.50}Zr_{0.50}O_{1.75}$ initially utilises the energy deposited by ion beam to form cation and anion anti-site defects leading to formation of a disordered fluorite structure. However, this conglomerate of ions (equal atom% of Nd^{3+} and Zr^{4+}) is not stable as disordered fluorite due to the radius ratio and hence further energy deposited by ion beams leads to its amorphisation. This has been observed by various researchers including Patel et al. and Sattonay et al. as mentioned earlier. However, the composition employed in present investigations has 20 mol% Nd^{3+} in ZrO_2 which is a stable disordered fluorite structure. The energy deposited by swift heavy ions is utilised for further randomisation of cations which again yields fluorite-type structure and does not amorphise. Thus, it clearly shows that for a particular set of ions, the radiation damage effect depends enormously on composition and structure. These results might have implications on the minor actinide loading in zirconia in context of their radiation tolerance.

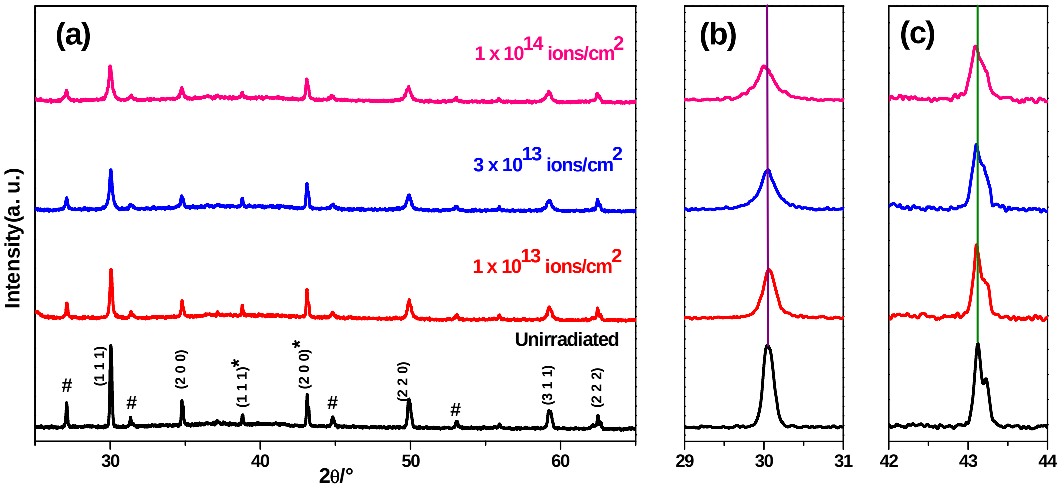

Fig. 7.7: (a) In-situ XRD patterns of $Zr_{0.80}Nd_{0.20}O_{1.90}$–MgO before and after irradiation with 120 MeVAu ions at different fluences, (b) expanded view of (111) peak of $Zr_{0.80}Nd_{0.20}O_{1.90}$ with varying ion fluence, and (c) expanded view of (200) peak of MgO with varying ion fluence; (#: peaks from sample support)

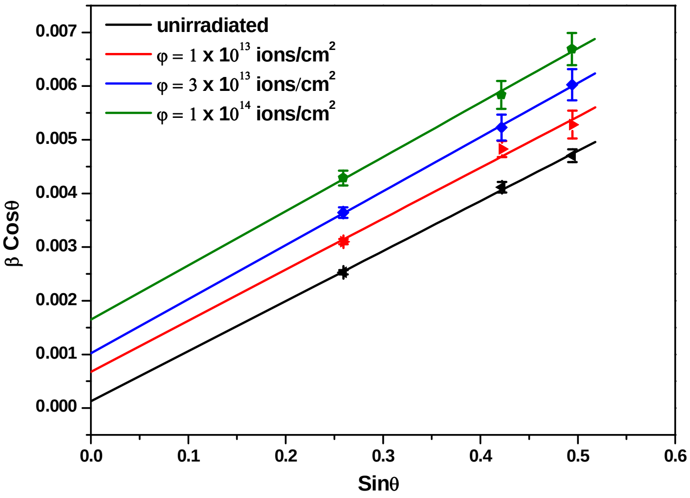

Fig. 7.8: Williamson–Hall plots of $Zr_{0.80}Nd_{0.20}O_{1.90}$ phase in $Zr_{0.80}Nd_{0.20}O_{1.90}$–MgO (50 wt.%) composite at different ion fluencies

The *in situ* XRD pattern of $Zr_{0.80}Nd_{0.20}O_{1.90}$–MgO (50 wt.%) as a function of fluence is shown in Fig. 7.7(a). The expanded view of the most intense diffraction line (111) of $Zr_{0.80}Nd_{0.20}O_{1.90}$ and (200) of MgO at different ion fluences is depicted in Fig. 7.7(b) and 7.7(c), respectively. As is obvious from the figure, the cubic structures of both $Zr_{0.80}Nd_{0.20}O_{1.90}$ and MgO are retained under irradiation at fluences employed in present experiments. As in the case of bare $Zr_{0.80}Nd_{0.20}O_{1.90}$, peak broadening, reduction in the intensity of the diffraction maxima and shift of diffraction lines to lower 2θ angle are observed for fluorite phase of $Zr_{0.80}Nd_{0.20}O_{1.90}$ in composite as well. As discussed in case of bare $Zr_{0.80}Nd_{0.20}O_{1.90}$, the broadening may be due to strain induced in the lattice due to irradiation displacement or particle size reduction. In order to confirm the source of the peak broadening, Williamson–Hall plot [167] has been constructed from the XRD patterns obtained at each irradiation fluence for the $Zr_{0.80}Nd_{0.20}O_{1.9}$ phase in $Zr_{0.80}Nd_{0.20}O_{1.90}$–MgO (50 wt.%) composite and is shown in Fig. 7.8. The size broadening shows 1/cosθ dependence while the strain broadening shows tanθ dependence. The plot of βcosθ as a function of sinθ yields a straight line in which the slope represents strain component and the intercept is signature of size broadening component. The intercept is inversely proportional to particle size. In the present case, systematic evolution of intercept is observed which suggest particle size decreases with increasing fluence. The slope also increases marginally with increasing ion fluence which suggests increasing strain in the lattice. Thus the broadening is mainly due to fragmentation of particles. Many researchers [168-170] have observed broadening of XRD peaks upon swift heavy ion irradiation on materials which has been explained on the basis of coulomb explosion and the inelastic thermal spike models [168]. Generally, according to these models, irradiation induces strain in the materials with larger grain sizes. This accumulated strain is relaxed by fragmentation of the larger grains into smaller ones.

Concerning the intensity of the diffraction maxima, it is amply clear from Fig. 7.6 that intensity for (111) plane of $Zr_{0.80}Nd_{0.20}O_{1.90}$ phase in the composite, post-irradiation, is greater than the intensity of the same in pure $Zr_{0.80}Nd_{0.20}O_{1.90}$, which explains higher radiation stability of $Zr_{0.80}Nd_{0.20}O_{1.90}$ in composite form. The intensity for (111) plane of bare $Zr_{0.80}Nd_{0.20}O_{1.90}$ phase at the highest fluence (1 x 10^{14} ions/cm^{2}) is 27% of unirradiated sample, whereas the corresponding value for the same in $Zr_{0.80}Nd_{0.20}O_{1.90}$–MgO composite is 41%. In case of the composite, the relative intensity reduction for the MgO phase is much less than that for the $Zr_{0.80}Nd_{0.20}O_{1.90}$ phase, as a function of fluence (the intensity for (200) plane of MgO phase at the highest fluence (1 x 10^{14} ions/cm^{2}) is 61% of unirradiated sample). This proves that out of two phases in the composite, MgO phase shows better radiation tolerance. It is plausibly due to the fact that the composite will have higher thermal conductivity which will lead to better dissipation of the energy deposited by radiation. This would manifest in better radiation stability.

The reduction in the relative intensity of the diffraction maxima I (φ) with increasing ion fluence (φ) have also been fitted in Fig. 7.6 using the following equation [171-174]:

$$I(\varphi) = a + b\, e^{-\sigma \varphi} \qquad (7.1)$$

where σ (= $\pi d^2/4$) the damage cross-section of a single ion track of diameter ‘d’ and a and b are constants. The track diameter is found to be 4.05 nm for $Zr_{0.80}Nd_{0.20}O_{1.90}$ phase and 2.12 nm for MgO phase in the composite composition.

The *in situ* XRD patterns of $Zr_{0.80}Nd_{0.10}Y_{0.10}O_{1.90}$ as a function of fluence are shown in Fig. 7.9(a). The expanded view of the most intense diffraction line (111) of $Zr_{0.80}Nd_{0.10}Y_{0.10}O_{1.90}$ at different ion fluences is depicted in Fig. 7.9(b). In this case also, fluorite structure of $Zr_{0.80}Nd_{0.10}Y_{0.10}O_{1.90}$ is retained under irradiation but there is relatively much higher decrease in intensity of peaks in irradiated samples suggesting massive damage in the lattice.

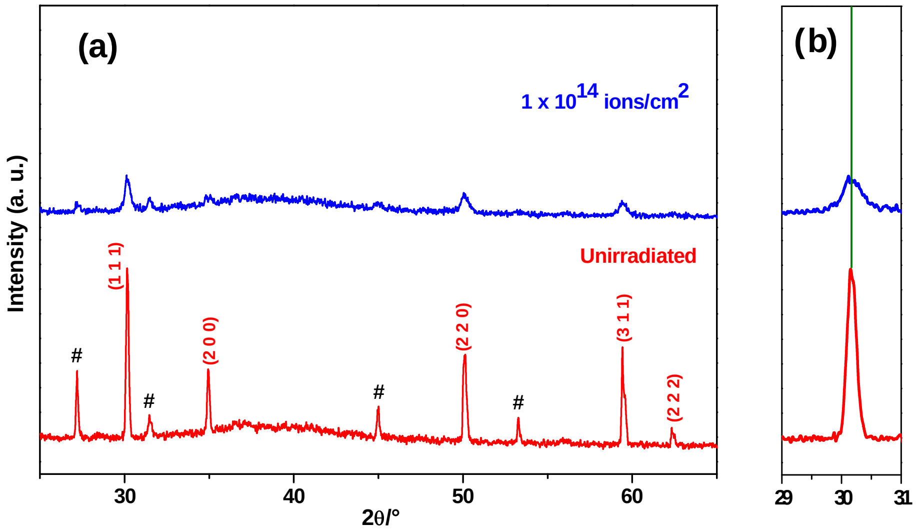

Fig. 7.9: (a) In-situ XRD patterns of $Zr_{0.80}Nd_{0.10}Y_{0.10}O_{1.90}$ before and after irradiation with 120 MeV Au ions at different fluences, and (b) expanded view of (111) peak of $Zr_{0.80}Nd_{0.10}Y_{0.10}O_{1.90}$ with varying ion fluence (#: peaks from sample support)

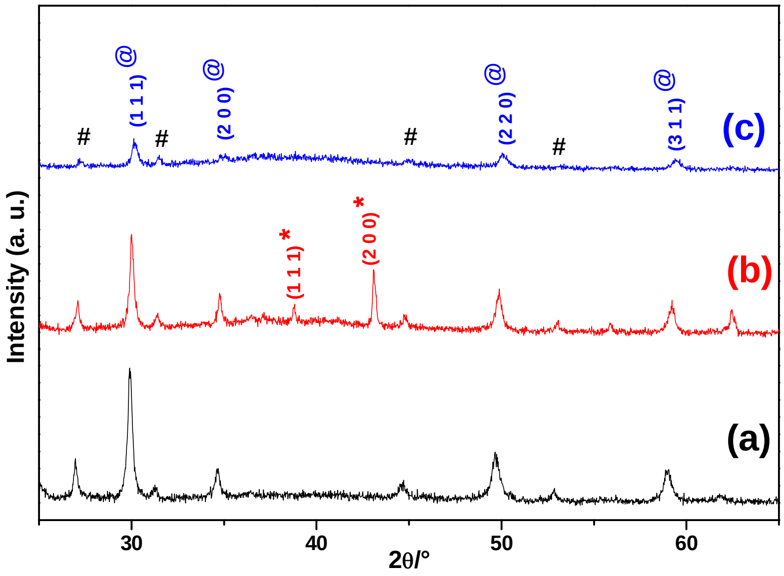

Fig. 7.10: XRD patterns of the samples irradiated with 120 MeV Au ions at the fluence 1 x 10^{14} ions/cm^2 (a) $Zr_{0.80}Nd_{0.20}O_{1.90}$ (b) $Zr_{0.80}Nd_{0.20}O_{1.90}$–MgO (50 wt.%) composite and (c) $Zr_{0.80}Nd_{0.10}Y_{0.10}O_{1.90}$. (@: F type peak for $Zr_{0.80}Nd_{0.20}O_{1.90}$ and $Zr_{0.80}Nd_{0.10}Y_{0.10}O_{1.90}$, *: peaks for cubic MgO and #: peaks from sample support)

It has been suggested that covalency of the bonds in the compounds are related to its radiation tolerance [175]. Higher the covalency lower is the radiation stability. This has been attributed to the fact that the recombination of displaced ions is much higher in ionic compounds as compared to covalent compound due to charge neutrality consideration. In simpler words, after irradiation, there is a formation of pool of interstitials and vacancies and the radiation tolerance would be determined by the capability of the material to recombine those interstitials and vacancies thereby regenerating the original undamaged zones. In materials with ionic character, there will be higher tendency to recombine as compared to more covalent materials like SiO_2

In the present case, the electronegativities of Nd, Y and O are 1.14, 1.22 and 3.44 on Pauling scale. Thus, Nd-O bond is more ionic than Y-O bond. Substituting 10 mol% Y in the composition $Zr_{0.80}Nd_{0.20}O_{1.90}$ to get $Zr_{0.80}Nd_{0.10}Y_{0.10}O_{1.90}$ increases the covalent character. This may plausibly be the reason for decreased radiation tolerance observed in $Zr_{0.80}Nd_{0.10}Y_{0.10}O_{1.90}$ as compared to $Zr_{0.80}Nd_{0.20}O_{1.90}$. Infact, the covalency factor also supports the enhanced radiation stability of MgO observed in $Zr_{0.80}Nd_{0.20}O_{1.90}$–MgO composite as compared to $Zr_{0.80}Nd_{0.20}O_{1.90}$ phase. MgO (electronegativity for Mg = 1.31) is much more ionic than $Zr_{0.80}Nd_{0.20}O_{1.90}$. Therefore, MgO exhibits highest radiation stability among all phases present in these systems. Also, presence of 50 wt.% of MgO renders better stability to $Zr_{0.80}Nd_{0.20}O_{1.90}$ phases present in the composite as compared to bare $Zr_{0.80}Nd_{0.20}O_{1.90}$.

Fig. 7.10 depicts the XRD patterns of all the three compositions at the same fluence (1×10^{14} ions/cm^2) clearly explaining the relative stability of the three nominal compositions as discussed above.

The SEM image before and after irradiation for the representative sample, $Zr_{0.80}Nd_{0.20}O_{1.90}$, have been shown in Fig. 7.11(a) and (b). Any microstructural change could not be detected by scanning electron microscope upon irradiation with 120 MeV Au ions.

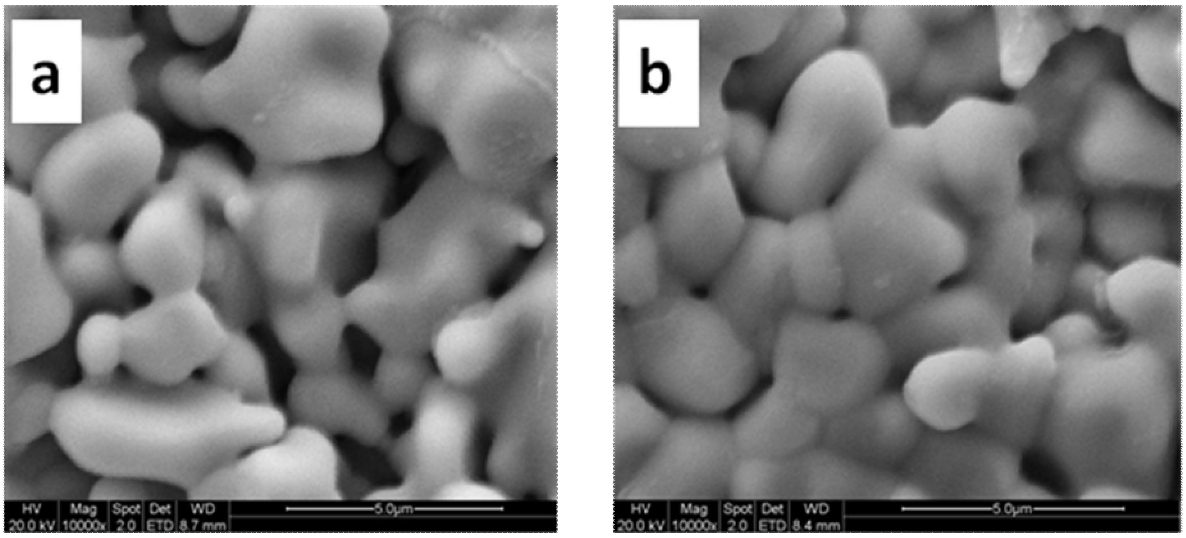

Fig. 7.11: SEM image of $Zr_{0.80}Nd_{0.20}O_{1.90}$ (a) unirradiated sample and (b) after irradiation with 120 MeV Au ions at the fluence 1 x 10^{14} ions/cm^2

The XANES spectra of Zr K edge, Nd L_{III} edge corresponding to samples $Zr_{0.80}Nd_{0.20}O_{1.90}$, $Zr_{0.80}Nd_{0.20}O_{1.90}$–MgO composite and $Zr_{0.80}Nd_{0.10}Y_{0.10}O_{1.90}$ before and after irradiation are shown in Fig. 7.12 and Fig. 7.13. The XANES results confirm that no systematic change in electronic structure of the material or in the local bonding environment of the Zr and Nd cations occurs after ion irradiation. This technique is sensitive to the valence state of the cation and its electronic configuration. The lack of modification to the Zr K-edge and Nd L_{III}-edge in the form of either energy shifts or a change in the edge shape indicates that its chemical state is maintained despite the production of defects. Tracy et al. also reported high radiation tolerance in the actinide materials which does not exhibit redox response on the ion irradiation [176]. Thus, observation of high radiation tolerance of present systems might be due to retention of their chemical states along with structural factors.

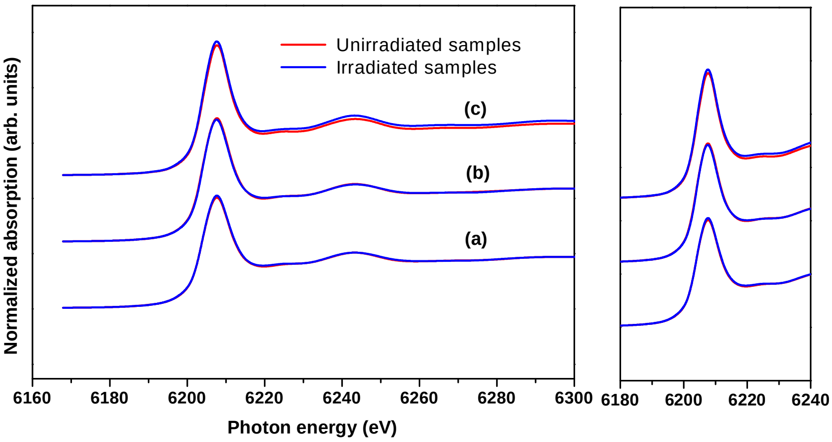

Fig. 7.12: Normalised XANES spectra for irradiated and unirradiated samples at Nd L_{III} edge; (a) $Zr_{0.80}Nd_{0.20}O_{1.90}$ (b) $Zr_{0.80}Nd_{0.20}O_{1.90}$–MgO (50 wt.%) and (c) $Zr_{0.80}Nd_{0.10}Y_{0.10}O_{1.9}$. Red coloured line represents spectra for unirradiated samples and blue coloured line represents spectra for irradiated samples

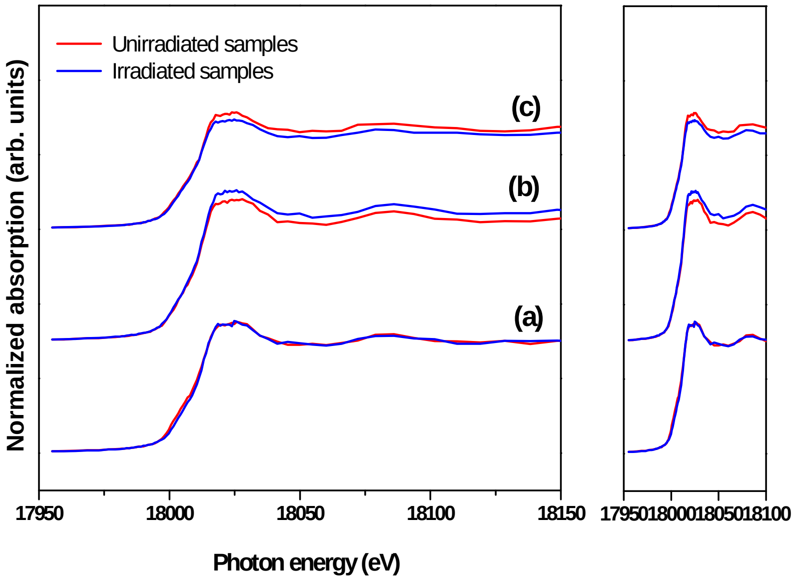

Fig. 7.13: Normalised XANES spectra for irradiated and unirradiated samples at Zr K edge; (a) $Zr_{0.80}Nd_{0.20}O_{1.90}$ (b) $Zr_{0.80}Nd_{0.20}O_{1.90}$–MgO (50 wt.%) and (c) $Zr_{0.80}Nd_{0.10}Y_{0.10}O_{1.90}$. Red coloured line represents spectra for unirradiated samples and blue coloured line represents spectra for irradiated samples

7.4. Conclusion

The XRD results confirm that the fluorite structure is retained under swift heavy ion irradiation for all the compositions explaining their exceptional radiation stability. The results also indicate better irradiation behaviour of $Zr_{0.80}Nd_{0.20}O_{1.90}$ (defect fluorite structure) over $Zr_{0.50}Nd_{0.50}O_{1.75}$ (pyrocholore) explaining that the radiation damage effect depends enormously on composition and structure. These results might have implications on the minor actinide loading in zirconia in context of their radiation tolerance. Formation of a CERCER (ceramic-ceramic) composite of Nd-stabilised zirconia with MgO enhanced the radiation tolerance behaviour of $Zr_{0.80}Nd_{0.20}O_{1.90}$ against swift heavy ion irradiation. Also, it is observed that out of two phases in the composite, MgO phase shows better radiation tolerance as compared to Nd-stabilised zirconia phase. Substitution of 10 mol% Y in the composition $Zr_{0.80}Nd_{0.20}O_{1.90}$ to get $Zr_{0.80}Nd_{0.10}Y_{0.10}O_{1.90}$ increases the covalent character thereby leading to decrease in radiation stability of the lattice. Investigating these compositions by XANES spectroscopy before and after irradiation do not show any change in local electronic structure of constituent ions.

CHAPTER 8

Summary and future scope

The thesis presents synthesis, characterization, thermo-physical properties and radiation stability of zirconia based materials for their application as a host matrix for transmutation of plutonium and minor actinides (MAs) in order to circumvent their long term radio-toxicity, heat load issues and proliferation concerns. The literature survey indicated that zirconia based materials could be the better choice among the oxide based materials as host matrix for this purpose. Non-radioactive surrogates (CeO_2 for PuO_2 and Nd_2O_3 for Am_2O_3 & Cm_2O_3) have been employed in place of these highly radioactive materials (Pu and MAs) in these studies to avoid radiological hazards. The resemblances of chemical and physical properties of the actinides and their respective surrogates, as discussed in chapter 1, provide us a platform to investigate the structural feasibility of loading of plutonium and minor actinides in zirconia based materials using their surrogates. In fact, the present study on phase relation in ZrO_2–PuO_2 system yields similar results as compared to well studied ZrO_2–CeO_2 system thereby providing the validity to the use of CeO_2 as a surrogate for phase relation (structural) studies in PuO_2-based systems. This is also a value addition to the literature for the applicability of CeO_2 as a surrogate for PuO_2.

A summary of the results obtained from the thesis is presented in the following section. Investigation of phase relation in $Zr_{1-x}Nd_xO_{2-x/2}$ ($0.0 \leq x \leq 1.0$) system (ZrO_2 as matrix component and Nd_2O_3 as MA surrogate) states that approximately 20 mol% $NdO_{1.5}$ substitution is required for stabilizing monoclinic ZrO_2 in fluorite-type cubic phase. A maximum of 50 mol% $NdO_{1.5}$ can be incorporated in monoclinic ZrO_2 maintaining single phase pyrochlore type cubic structure. However, a hybrid region consisting of fluorite-type and pyrochlore-type domains is found to exist in this cubic phase field.

The nominal composition with x = 0.3 is largely fluorite-type with very weak pyrochlore ordering in contrast to the nominal composition with x = 0.4 which is largely pyrochlore. The effect of structure on radiation stability of these compositions is noteworthy. 120 MeV Au ions as swift heavy ions (SHI) produced in ion accelerator have been used to simulate radiation damage effects in these materials. The XRD results confirm that the fluorite structure is retained under swift heavy ion irradiation (fluence: 1 x 10^{14} ions/cm^2) for the composition $Zr_{0.80}Nd_{0.20}O_{1.90}$ (x = 0.2) explaining their exceptional radiation stability. However, Patel et al. [155] observed that the composition $Zr_{0.50}Nd_{0.50}O_{1.75}$ (x = 0.5) having pyrochlore structure undergoes phase transformation, from pyrochlore to defect fluorite and then complete amorphization occurs at the fluence of 5 x 10^{13} ions/cm^2. Thus, these results directly pose restriction on the extent of minor actinide loading in ZrO_2 in context of their radiation tolerance. The lower thermal conductivity of cubic stabilized zirconia ($Zr_{0.80}Nd_{0.20}O_{1.90}$) as compared to standard UO_2 fuel highlights the need for improvement in matrix design for nuclear fuel application. The phase relation in $Zr_{1-x}Nd_xO_{2-x/2}$ ($0.0 \leq x \leq 1.0$) system also states that the incorporation of 10 mol% $NdO_{1.5}$ in ZrO_2 leads to a biphasic mixture consisting of monoclinic zirconia (m-ZrO_2) and Nd-stabilized cubic zirconia. The extension of cubic phase field to lower Nd^{3+} (< 20 mol %) incorporation level has been made possible by co-doping of Y^{3+} along with Nd^{3+} in appropriate mole fraction. This has been confirmed by establishing the phase relation in $Zr_{0.70}[Y_{1-x}Nd_x]_{0.30}O_{1.85}$ ($0.0 \leq x \leq 1.0$) system. The studies imply that the entire series exists as single-phasic F-type lattice. Investigation also shows that substitution of Nd^{3+} by Y^{3+} in $Zr_{0.70}[Y_{1-x}Nd_x]_{0.30}O_{1.85}$ ($0.0 \leq x \leq 1.0$) system leads to higher thermal conductivity which is attributed to the large difference of mass and ionic size between Zr^{4+} and Nd^{3+} relative to Zr^{4+} and Y^{3+}. These results seem to appear encouraging from thermal conductivity point of view of nuclear fuels at least in case of lower Nd^{3+} (< 20 mol %) incorporation level in ZrO_2. However, the introduction of Y^{3+} along with

Nd^{3+} to stabilize zirconia in cubic phase imparted poorer radiation stability as is observed for the composition $Zr_{0.80}Nd_{0.10}Y_{0.10}O_{1.90}$ as compared to $Zr_{0.80}Nd_{0.20}O_{1.90}$. It must be mentioned that formation of a CER-CER composite of MgO with $Zr_{0.80}Nd_{0.20}O_{1.90}$ enhanced the radiation tolerance behaviour of $Zr_{0.80}Nd_{0.20}O_{1.90}$ against swift heavy ion irradiation. This study also proves that out of two phases in the composite, MgO phase shows better radiation tolerance. MgO is used to form the composite in this context to enhance the thermal conductivity of the system. The structural feasibility of co-loading of Am^{3+} and Pu^{4+} in ZrO_2 for MA transmutation is demonstrated by investigating $Nd_{0.20}[Zr_{1-x}Ce_x]_{0.80}O_{1.90}$ $(0.0 \leq x \leq 1.0)$ system. The results imply that substitution of a trivalent ion like Nd^{3+} could stabilize the otherwise multi-phasic CeO_2–ZrO_2 system and the entire phase relation is revealed to be single-phasic F-type throughout the composition range. The significant implication of this result is that the loading of CeO_2 (surrogate for plutonia) in ZrO_2 will not yield a single-phasic product but when substituted along with Nd^{3+} (surrogate for Am^{3+}), a single-phasic composition is attainable. The results are encouraging considering that single-phasic compositions are expected to possess superior and homogeneous properties. Thus, all the above mentioned studies show the structural feasibility of loading of only Am^{3+}, Am^{3+} & Y^{3+} as well as Am^{3+} & Pu^{4+} in ZrO_2 in context of MA transmutation using respective surrogates. For the sake of completeness, radioactive PuO_2 material itself instead of surrogate material has been employed as the fissile phase in the investigation of phase relation and thermo-physical properties in YSZ–PuO_2 and ZrO_2–PuO_2 system. The phase relations are found to depend tremendously on synthetic atmosphere attributed to redox response of plutonium in different atmosphere. The investigations in ZrO_2–PuO_2 system clearly indicate that any trivalent actinide or any actinide which can be reduced to trivalent state can form cubic phase (F-type or pyrochlore) with ZrO_2 if present in 20–50 mol% range. The results obtained on these PuO_2-based systems are of significant relevance to Inert matrix fuel concept for Pu and MA transmuation.

The future scope of present thesis is provided in the following section. As already indicated, zirconia based ceramics possess lower thermal conductivity. Hence, composite of these materials with MgO (possess high thermal conductivity) may be studied in terms of phase relation and thermo-physical properties. Moreover, phase relation and thermo-physical properties in ZrO_2–PuO_2 system can be studied in more detail. Lastly, investigation in phase relation and thermo-physical properties in ZrO_2–$AmO_{1.5}$ may be carried out as future scope of present thesis.

References:

[1] N. Panwar, S. Kaushik, S. Kothari, Role of renewable energy sources in environmental protection: a review, Renew. Sust. Energ. Rev. 15 (2011) 1513-1524.

[2] D. Timmons, J.M. Harris, B. Roach, The economics of renewable energy, Global Development and Environment Institute, Tufts University, 2014, http://www.ase.tufts.edu/gdae/education_materials/modules/renewableenergyecon.pdf.

[3] B. Comby, The benefits of nuclear energy, http://ecolo.org/documents/documents_in_english/benefits-of-nuclear.pdf.

[4] International Atomic Energy Agency’s Power Reactor Information Systems Database.

[5] Central Electricity Authority (CEA), http://powermin.nic.in/en/content/power-sector-glance-all-india.

[6] B.W. Brook, A. Alonso, D.A. Meneley, J. Misak, T. Blees, J.B. van Erp, Why nuclear energy is sustainable and has to be part of the energy mix, Sustain. Mater. Technol. 1 (2014) 8-16.

[7] S. Hall, Uranium 2014: Resources, Production and Demand (the “Red Book”) supply and demand projections to 2035, 2014.

[8] P. Hania, F. Klaassen, 3.04-Thorium oxide fuel: R.J.M. Konings (Ed.), Compr. Nucl. Mater, Elsevier, Oxford, 2012, 87–108.

[9] P. Vijayan, V. Shivakumar, S. Basu, R. Sinha, Role of thorium in the Indian nuclear power programme, Prog. Nucl. Energy 101 (2017) 43-52.

[10] M.P. Cottrell, Confronting the nuclear paradox, Energy Res. Soc. Sci. 24 (2017) 6-11.

[11] D. Westlén, Why Faster is Better: On minor actinide transmutation in hard neutron, Doctoral Thesis, KTH School of Engineering Sciences, Stockholm, Sweden, 2007.

[12] IAEA Technical Reports Series No.435 Implications of Partitioning and Transmutation in Radioactive Waste Management.

[13] J. Magill, V. Berthou, D. Haas, J. Galy, R. Schenkel, J. Wiese, G. Heusener, J. Tommasi, G. Youinou, Impact limits of partitioning and transmutation scenarios on the radiotoxicity of actinides in radioactive waste, Nucl. Energy 42 (2003) 263-278.

[14] Physics and Safety of Transmutation Systems: A Status Report, NEA report 6090, Paris, France, 2006.

[15] S. Pillon, 3.05-Actinide-bearing fuels and transmutation targets, R.J.M. Konings (Ed.), Compr. Nucl. Mater. Elsevier, Oxford, (2012) 109-141

[16] E.-M. Gonzalez-Romero, Impact of partitioning and transmutation on the high level waste management, Nucl. Eng. Des. 241 (2011) 3436-3444.

[17] A. Stanculescu, Accelerator driven systems (ADSs) for nuclear transmutation, Ann. Nucl. Energy 62 (2013) 607-612.

[18] T. Mukaiyama, H. Takano, T. Ogawa, T. Takizuka, M. Mizumoto, Partitioning and transmutation studies at JAERI both under OMEGA program and high-intensity proton accelerator project, Prog. Nucl. Energy 40 (2002) 403-413.

[19] A. Stanculescu, IAEA activities in the area of partitioning and transmutation, Nucl. Instrum. Methods Phys. Res. A 562 (2006) 614-617.

[20] M. Salvatores, Nuclear fuel cycle strategies including partitioning and transmutation, Nucl. Eng. Des. 235 (2005) 805-816.

[21] H. Wang, H. Otsu, H. Sakurai, D. Ahn, M. Aikawa, P. Doornenbal, N. Fukuda, T. Isobe, S. Kawakami, S. Koyama, Spallation reaction study for fission products in nuclear waste: Cross section measurements for ^{137}Cs and ^{90}Sr on proton and deuteron, Phys. Lett. B 754 (2016) 104-108.

[22] M. Mizumoto, Accelerators for Nuclear Waste Transmutation, Proc. Linac Conf., Tsukuba, 1994 pp. 317.

[23] S. Leray, Nuclear waste transmutation, Nucl. Instrum. Methods Phys. Res. B, 113 (1996) 495-500.

[24] P. Darnowski, N. Uzunow, Minor actinides impact on basic safety parameters of medium-sized sodium-cooled fast reactor, Nukleonika 60 (2015) 171-179.

[25] C. Degueldre, J. Paratte, Concepts for an inert matrix fuel, an overview, J. Nucl. Mater. 274 (1999) 1-6.

[26] C. Degueldre, T. Yamashita, Inert matrix fuel strategies in the nuclear fuel cycle: the status of the initiative efforts at the 8th Inert Matrix Fuel Workshop, J. Nucl. Mater. 319 (2003) 1-5.

[27] J. Porta, S. Baldi, B. Guigon, Some neutronic properties of inert matrix in order to define a 100% IMF core, Proc. of Advanced Reactors with Innovative Fuels,(ARWIF'98) Villigen, Switzerland (1998) 21-23.

[28] I.A.E. Agency, Viability of Inert matrix fuel in reducing plutonium amounts in reactors, Vienna, 2006.

[29] R. Schram, K. Bakker, H. Hein, J. Boshoven, R. van der Laan, C. Sciolla, T. Yamashita, C. Hellwig, F. Ingold, R. Conrad, Design and fabrication aspects of a plutonium-incineration experiment using inert matrices in a "Once-Through-Then-Out" mode, Prog. Nucl. Energy 38 (2001) 259-262.

[30] H. Kleykamp, Selection of materials as diluents for burning of plutonium fuels in nuclear reactors, J. Nucl. Mater. 275 (1999) 1-11.

[31] R. Konings, K. Bakker, J. Boshoven, R. Conrad, H. Hein, The influence of neutron irradiation on the microstructure of Al_2O_3, $MgAl_2O_4$, $Y_3Al_5O_{12}$ and CeO_2, J. Nucl. Mater. 254 (1998) 135-142.

[32] E. Neeft, R. Konings, K. Bakker, J. Boshoven, H. Hein, R. Schram, A. van Veen, R. Conrad, Neutron irradiation of polycrystalline yttrium aluminate garnet, magnesium aluminate spinel and α-alumina, J. Nucl. Mater. 274 (1999) 78-83.

[33] E. Neeft, K. Bakker, R. Schram, R. Conrad, R. Konings, The EFTTRA-T3 irradiation experiment on inert matrix fuels, J. Nucl. Mater. 320 (2003) 106-116.

[34] E. Neeft, K. Bakker, H. Buurveld, J. Minkema, A. Paardekooper, R. Schram, C. Sciolla, O. Zwaagstra, B. Beemsterboer, J. Woittiez, Post irradiation examination of uranium inclusions in inert matrices, Prog. Nucl. Energy 38 (2001) 427-430.

[35] N. Chauvin, T. Albiol, R. Mazoyer, J. Noirot, D. Lespiaux, J. Dumas, C. Weinberg, J. Menard, J. Ottaviani, In-pile studies of inert matrices with emphasis on magnesia and magnesium aluminate spinel, J. Nucl. Mater. 274 (1999) 91-97.

[36] T. Wiss, H. Matzke, Heavy ion induced damage in $MgAl_2O_4$, an inert matrix candidate for the transmutation of minor actinides, Radiat. Meas. 31 (1999) 507-514.

[37] J. Noirot, L. Desgranges, N. Chauvin, V. Georgenthum, Post-irradiation examinations of THERMHET composite fuels for transmutation, J. Nucl. Mater. 320 (2003) 117-125.

[38] R. Konings, R. Conrad, G. Dassel, B. Pijlgroms, J. Somers, E. Toscano, The EFTTRA-T4 experiment on americium transmutation, J. Nucl. Mater. 282 (2000) 159-170.

[39] S. Miwa, M. Osaka, Oxidation and reduction behaviors of a prototypic MgO-PuO_{2-x} inert matrix fuel, J. Nucl. Mater. 487 (2017) 1-4.

[40] S. Yates, K. McClellan, J. Nino, The effect of processing on the thermal diffusivity of $MgO–Nd_2Zr_2O_7$ composites for inert matrix materials, J. Nucl. Mater. 393 (2009) 203-211.

[41] P. Medvedev, M. Lambregts, M. Meyer, Thermal conductivity and acid dissolution behavior of $MgO–ZrO_2$ ceramics for use in LWR inert matrix fuel, J. Nucl. Mater. 349 (2006) 167-177.

[42] P. Gotcu-Freis, J.-P. Hiernaut, J.-Y. Colle, C. Nästrén, A.F. Carretero, R. Konings, Vaporisation of candidate nuclear fuels and targets for transmutation of minor actinides, J. Nucl. Mater. 411 (2011) 119-125.

[43] F. Clinard, D. Rohr, W. Ranken, Neutron-Irradiation Damage in Stabilized ZrO_2, J. Am. Ceram. Soc. 60 (1977) 287-288.

[44] E. Vance, J. Boland, Fission fragment irradiation of single crystal monoclinic ZrO_2, Radiat. Eff. 37 (1978) 237-239.

[45] C. Degueldre, W. Wiesenack, Zirconia inert matrix fuel for plutonium and minor actinides management in reactors and as an ultimate waste form, Actinides 2008–Basic Science, Applications, and Technology, (Mater. Res. Soc. Symp. Proc. Warrendale, 2008), 1104-NN03-01.

[46] Q. Mistarihi, M.A. Umer, J.H. Kim, S.H. Hong, H.J. Ryu, Fabrication of ZrO_2-based nanocomposites for transuranic element-burning inert matrix fuel, Nucl. Eng. Technol. 47 (2015) 617-623.

[47] A.B. Corradi, F. Bondioli, A.M. Ferrari, Role of praseodymium on zirconia phases stabilization, Chem. Mater. 13 (2001) 4550-4554.

[48] S.-M. Ho, On the structural chemistry of zirconium oxide, Mater. Sci. Eng. 54 (1982) 23-29.

[49] S.I. Lopatin, S.M. Shugurov, Thermodynamic properties of the Lu_2O_3–ZrO_2 solid solutions by Knudsen effusion mass spectrometry at high temperature, J. Chem. Thermodyn. 72 (2014) 85-88.

[50] R. Schram, R. Van der Laan, F. Klaassen, K. Bakker, T. Yamashita, F. Ingold, The fabrication and irradiation of plutonium-containing inert matrix fuels for the 'Once Though Then Out'experiment, J. Nucl. Mater. 319 (2003) 118-125.

[51] C. Hellwig, U. Kasemeyer, Inert matrix fuel performance during the first two irradiation cycles in a test reactor: comparison with modelling results, J. Nucl. Mater. 319 (2003) 87-94.

[52] Y. Croixmarie, E. Abonneau, A. Fernandez, R. Konings, F. Desmoulière, L. Donnet, Fabrication of transmutation fuels and targets: the ECRIX and CAMIX-COCHIX experience, J. Nucl. Mater. 320 (2003) 11-17.

[53] R.J. Lemire, Chemical thermodynamics of neptunium and plutonium, (edited by OECD Nuclear Energy Agency), Amsterdam, Elsevier Science Publishers 2001.

[54] T. Chikalla, C. McNeilly, R. Skavdahl, The plutonium-oxygen system, J. Nucl. Mater. 12 (1964) 131-141.

[55] C. Guéneau, C. Chatillon, B. Sundman, Thermodynamic modelling of the plutonium–oxygen system, J. Nucl. Mater. 378 (2008) 257-272.

[56] H. Wriedt, The O-Pu (oxygen-plutonium) system, Bull. Alloy Phase Diagr. 11 (1990) 184-202.

[57] E. Epifano, C. Guéneau, R.C. Belin, R. Vauchy, F. Lebreton, J.-C. Richaud, A. Joly, C. Valot, P.M. Martin, Insight into the Am–O phase equilibria: a thermodynamic study coupling high-temperature XRD and CALPHAD modeling, Inorg. Chem. 56 (2017) 7416-7432.

[58] R.J. Silva, G. Bidoglio, P. Robouch, I. Puigdomènech, H. Wanner, M. Rand, Chemical thermodynamics of americium, Vol 2, Newnes 2012.

[59] C. Sari, E. Zamorani, An investigation in the americium oxide system, J. Nucl.Mater. 37 (1970) 324-330.

[60] R. Konings, Thermochemical and thermophysical properties of curium and its oxides, J. Nucl. Mater. 298 (2001) 255-268.

[61] W. Mosley, Phases and transformations in the curium-oxygen system, J. Inorg. Nucl. Chem. 34 (1972) 539-555.

[62] T. Chikalla, L. Eyring, The curium-oxygen system, J. Inorg. Nucl. Chem. 31 (1969) 85-93.

[63] A.K. Tyagi, B. Ambekar, M. Mathews, Simulation of lattice thermal expansion behaviour of $Th_{1-x}Pu_xO_2$ ($0.0 \leq x \leq 1.0$) using CeO_2 as a surrogate material for PuO_2, J. Alloys Compd. 337 (2002) 277-281.

[64] R.D. Shannon, Revised effective ionic radii and systematic studies of interatomic distances in halides and chalcogenides, Acta Crystallogr., Sect. A 32 (1976) 751-767.

[65] H.S. Kim, C.Y. Joung, B.H. Lee, J.Y. Oh, Y.H. Koo, P. Heimgartner, Applicability of CeO_2 as a surrogate for PuO_2 in a MOX fuel development, J. Nucl. Mater. 378 (2008) 98-104.

[66] K. Holliday, T. Hartmann, K. Czerwinski, Synthesis and characterization of zirconia–magnesia inert matrix fuel: Ce homolog studies, J. Nucl. Mater. 392 (2009) 487-493.

[67] Ö. Yildiz, G. Modolo, R. Telle, Compactibility and sintering behavior of nanocrystalline $(Th_{1-x}Ce_x)O_2$ powders synthesized by co-precipitation process, J. Nucl. Mater. 377 (2008) 396-400.

[68] A.T. Nelson, D.R. Rittman, J.T. White, J.T. Dunwoody, M. Kato, K.J. McClellan, An evaluation of the thermophysical properties of stoichiometric CeO_2 in comparison to UO_2 and PuO_2, J. Am. Ceram. Soc. 97 (2014) 3652-3659.

[69] H. Williams, H. Ning, M. Reece, R. Ambrosi, N. Bannister, K. Stephenson, Metal matrix composite fuel for space radioisotope energy sources, J. Nucl. Mater. 433 (2013) 116-123.

[70] T. Butler, E. Ketchen, J. DiStefano, Curium data sheets (No. ORNL-4910), Oak Ridge National Lab., Tenn. (USA), 1973.

[71] C. Rao, Chemical synthesis of solid inorganic materials, Mater. Sci. and Eng. B 18 (1993) 1-21.

[72] A.R. West, Solid state chemistry and its applications, John Wiley & Sons, 2007.

[73] K. Fujioka, A. Sugiyama, Y. Fujimoto, J. Kawanaka, N. Miyanaga, Ion diffusion at the bonding interface of undoped YAG/Yb: YAG composite ceramics, Optical Mater. 46 (2015) 542-547.

[74] P. Deb, Kinetics of heterogeneous solid state processes, Springer, 2014.

[75] I. Fábregas, D. Lamas, Parametric study of the gel-combustion synthesis of nanocrystalline ZrO_2-based powders, Powder Technol. 214 (2011) 218-228.

[76] R. Purohit, A.K. Tyagi, M. Mathews, S. Saha, Combustion synthesis and bulk thermal expansion studies of Ba and Sr thorates, J. Nucl. Mater. 280 (2000) 51-55.

[77] B.D. Cullity, Answers to Problems: Elements of X-ray Diffraction, Addison-Wesley Publishing Company, 1978.

[78] V.S. Jakkal, POWDERX: a FORTRAN software for refining the unit cell parameter for the powder diffraction pattern.

[79] M.M. Rahman, S.B. Khan, A. Jamal, M. Faisal, A.M. Aisiri, Iron oxide nanoparticles, Nanomaterials, InTech 2011.

http:www.intechopen.com/articles/show/title/iron-oxide-nanoparticles

[80] C.Y. Ho, R.E. Taylor, Thermal expansion of solids, ASM international, 1998.

[81] R.V. Krishnan, V. Mittal, R. Babu, A. Senapati, S. Bera, K. Nagarajan, Heat capacity measurements and XPS studies on uranium–lanthanum mixed oxides, J. Alloys Compd. 509 (2011) 3229-3237.

[82] R.V. Krishnan, K. Nagarajan, Heat capacity measurements on uranium–cerium mixed oxides by differential scanning calorimetry, Thermochim. Acta 440 (2006) 141-145.

[83] M. Sahu, K. Krishnan, M. Saxena, K. Ramakumar, Thermal expansion and heat capacity of Gd_6UO_{12} (s), J. Alloys Compd. 482 (2009) 141-146.

[84] D. Zhao, X. Qian, X. Gu, S.A. Jajja, R. Yang, Measurement techniques for thermal conductivity and interfacial thermal conductance of bulk and thin film materials, J. Electron. Packag. 138 (2016) 040802.

[85] Y. Takahashi, M. Murabayashi, Measurement of thermal properties of nuclear materials by laser flash method, J. Nucl. Sci. Technol. 12 (1975) 133-144.

[86] W. Parker, R. Jenkins, C. Butler, G. Abbott, Flash method of determining thermal diffusivity, heat capacity, and thermal conductivity, J. Appl. Phys. 32 (1961) 1679-1684.

[87] H.W. Deem, W. Wood, Flash Thermal-Diffusivity Measurements Using a Laser, Rev. Sci. Instrum. 33 (1962) 1107-1109.

[88] Z.-G. Liu, J.-H. Ouyang, B.-H. Wang, Y. Zhou, J. Li, Preparation and thermophysical properties of $Nd_xZr_{1-x}O_{2-x/2}$ (x = 0.1, 0.2, 0.3, 0.4, 0.5) ceramics, J. Alloys Compd. 466 (2008) 39-44.

[89] D. Kanjilal, S. Chopra, M. Narayanan, I.S. Iyer, V. Jha, R. Joshi, S. Datta, Testing and operation of the 15UD Pelletron at NSC, Nucl. Instrum. Methods Phys. Res. A 328 (1993) 97-100.

[90] G. Mehta, A. Patro, 15 UD pelletron of the nuclear science centre—status report, Nucl. Instrum. Methods Phys. Res. A 268 (1988) 334-336.

[91] A schematic figure showing the principle of acceleration of ions in pelletron. http://www.iuac.res.in/accel/pell/index.html.

[92] K. Kuramoto, H. Mitamura, T. Banba, S. Muraoka, Development of ceramic waste forms for actinide-rich waste—Radiation stability of perovskite and phase and chemical stabilities of Zr-and Al-based ceramics, Prog. Nucl. Energy 32 (1998) 509-516.

[93] H. Ohtani, S. Matsumoto, B. Sundman, T. Sakuma, M. Hasebe, Equilibrium between Fluorite and Pyrochlore Structures in the ZrO_2–Nd_2O_3 System, Mater. Trans. 46 (2005) 1167-1174.

[94] A. Shlyakhtina, D. Belov, A. Knotko, M. Avdeev, I. Kolbanev, G. Vorobieva, O. Karyagina, L. Shcherbakova, Oxide ion transport in $(Nd_{2-x}Zr_x)Zr_2O_{7+\delta}$ electrolytes by an interstitial mechanism, J. Alloys Compd. 603 (2014) 274-281.

[95] T. Van Dijk, R. Helmholdt, A. Burggraaf, Neutron powder diffraction studies of fluorite and pyrochlore $Nd_xZr_{1-x}O_{2-x/2}$ solid solutions with 0.25<x< 0.55, Phys. Status Solidi B, 101 (1980) 765-774.

[96] P. Anithakumari, V. Grover, C. Nandi, K. Bhattacharyya, A.K. Tyagi, Utilizing non-stoichiometry in $Nd_2Zr_2O_7$ pyrochlore: exploring superior ionic conductors, RSC Adv. 6 (2016) 97566-97579.

[97] D.A. Daramola, M. Muthuvel, G.G. Botte, Density functional theory analysis of Raman frequency modes of monoclinic zirconium oxide using Gaussian basis sets and isotopic substitution, J. Phys. chem. B, 114 (2010) 9323-9329.

[98] B.-K. Kim, J.-W. Hahn, K.R. Han, Quantitative phase analysis in tetragonal-rich tetragonal/monoclinic two phase zirconia by Raman spectroscopy, J. Mater. Sci. Lett. 16 (1997) 669-671.

[99] A.J. Semjonow, E. Anastassakis, Asymmetry of defect-induced Raman spectra in yttria-stabilized zirconia, Phys. A, 201 (1993) 416-420.

[100] B.E. Scheetz, W.B. White, Characterization of anion disorder in zirconate $A_2B_2O_7$ compounds by Raman spectroscopy, J. .Am. Ceram. Soc. 62 (1979) 468-470.

[101] M. Subramanian, G. Aravamudan, G.S. Rao, Oxide pyrochlores—a review, Prog. Solid State Chem. 15 (1983) 55-143.

[102] B. Mandal, P. Krishna, A.K. Tyagi, Order–disorder transition in the $Nd_{2-y}Y_yZr_2O_7$ system: Probed by X-ray diffraction and Raman spectroscopy, J. Solid State Chem. 183 (2010) 41-45.

[103] M. Glerup, O.F. Nielsen, F.W. Poulsen, The structural transformation from the pyrochlore structure, $A_2B_2O_7$, to the fluorite structure, AO_2, studied by Raman spectroscopy and defect chemistry modeling, J. Solid State Chem. 160 (2001) 25-32.

[104] A.M. Heyns, K.J. Range, Raman and infrared study of neodymium oxide peroxide, $Nd_2O_2(O_2)$, J. Raman Spectrosc. 25 (1994) 855-859.

[105] R. Belin, P. Valenza, P. Raison, M. Tillard, Synthesis and Rietveld structure refinement of americium pyrochlore $Am_2Zr_2O_7$, J. Alloys Compd. 448 (2008) 321-324.

[106] H. Otobe, M. Takano, H. Hayashi, Y. Arai, Oxygen potentials of pyrochlore-type $Am_2Zr_2O_{7+y}$, J. Am. Ceram. Soc. 94 (2011) 3596-3599.

[107] C. Nästren, R. Jardin, J. Somers, M. Walter, B. Brendebach, Actinide incorporation in a zirconia based pyrochlore $(Nd_{1.8}An_{0.2})Zr_2O_{7+x}$ (An= Th, U, Np, Pu, Am), J. Solid State Chem. 182 (2009) 1-7.

[108] L. Guo, Y. Zhang, C. Wang, X. Zhao, F. Ye, Phase structure evolution and thermal expansion variation of Sc_2O_3 doped $Nd_2Zr_2O_7$ ceramics, Mater. Des. 82 (2015) 114-118.

[109] L. Guo, Y. Zhang, F. Ye, Phase structure evolution and thermo-physical properties of nonstoichiometry $Nd_{2-x}Zr_{2+x}O_{7+x/2}$ pyrochlore ceramics, J. Am. Ceram. Soc. 98 (2015) 1013-1018.

[110] C. Wan, Z. Qu, A. Du, W. Pan, Influence of B site substituent Ti on the structure and thermophysical properties of $A_2B_2O_7$-type pyrochlore $Gd_2Zr_2O_7$, Acta Mater. 57 (2009) 4782-4789.

[111] L. Van Uitert, H. O'bryan, M. Lines, H. Guggenheim, G. Zydzik, Thermal expansion—An empirical correlation, Mater. Res. Bull. 12 (1977) 261-268.

[112] M. Mathews, B. Ambekar, A.K. Tyagi, Lattice thermal expansion studies of $Th_{1-x}Nd_xO_{2-x/2}$ solid solutions, Ceram. Int. 32 (2006) 609-612.

[113] S. Chavan, M. Mathews, A.K. Tyagi, Phase relations and thermal expansion studies in the CeO_2–$NdO_{1.5}$ system, Mater. Res. Bull. 40 (2005) 1558-1568.

[114] J.R. Hayes, A.P. Grosvenor, M. Saoudi, An investigation of the thermal stability of $Nd_xY_yZr_{1-x-y}O_{2-\delta}$ inert matrix fuel materials, J. Alloys Compd. 635 (2015) 245-255.

[115] C. Nandi, D. Jain, V. Grover, K. Krishnan, J. Banerjee, A. Prakash, K. Khan, A.K. Tyagi, ZrO_2-$NdO_{1.5}$ system: Investigations of phase relation and thermophysical properties, Mater. Des. 121 (2017) 101-108.

[116] D. Michel, R. Collongues, Study by Raman spectroscopy of order-disorder phenomena occurring in some binary oxides with fluorite-related structures, J. Raman Spectrosc. 5 (1976) 163-180.

[117] M. Yashima, K. Ohtake, H. Arashi, M. Kakihana, M. Yoshimura, Determination of cubic-tetragonal phase boundary in $Zr_{1-X}Y_XO_{2-X/2}$ solid solutions by Raman spectroscopy, J. App. Phys. 74 (1993) 7603-7605.

[118] M. Yashima, K. Ohtake, M. Kakihana, H. Arashi, M. Yoshimura, Determination of tetragonal-cubic phase boundary of $Zr_{1-X}R_XO_{2-X/2}$ (R = Nd, Sm, Y, Er and Yb) by Raman scattering, J. Phys. Chem. Solids 57 (1996) 17-24.

[119] T. Hirata, E. Asari, M. Kitajima, Infrared and Raman spectroscopic studies of ZrO_2 polymorphs doped with Y_2O_3 or CeO_2, J. Solid State Chem. 110 (1994) 201-207.

[120] M. Zhao, X. Ren, J. Yang, W. Pan, Thermo-mechanical properties of ThO_2 doped Y_2O_3 stabilized ZrO_2 for thermal barrier coatings, Ceram. Int. 42 (2016) 501-508.

[121] P. Mele, C. Artini, A. Ubaldini, G. Costa, M. Carnasciali, R. Masini, Synthesis, structure and magnetic properties in the Nd_2O_3–Gd_2O_3 mixed system synthesized at 1200°C, J. Phys. Chem. Solids 70 (2009) 276-280.

[122] I. Barin, G. Platzki, Thermochemical data of pure substances, Wiley Online Library, 1989.

[123] K. Schlichting, N. Padture, P. Klemens, Thermal conductivity of dense and porous yttria-stabilized zirconia, J. Mater. Sci. 36 (2001) 3003-3010.

[124] J.F. Bisson, D. Fournier, M. Poulain, O. Lavigne, R. Mévrel, Thermal conductivity of yttria–zirconia single crystals, determined with spatially resolved infrared thermography, J. Am. Ceram. Soc. 83 (2000) 1993-1998.

[125] J. Wu, X. Wei, N.P. Padture, P.G. Klemens, M. Gell, E. García, P. Miranzo, M.I. Osendi, Low thermal conductivity rare earth zirconates for potential thermal barrier coating Applications, J. Am. Ceram. Soc. 85 (2002) 3031-3035.

[126] L. Sun, H. Guo, H. Peng, S. Gong, H. Xu, Phase stability and thermal conductivity of ytterbia and yttria co-doped zirconia, Prog. Nat. Sci. : Mater. Int. 23 (2013) 440-445.

[127] D.R. Clarke, Materials selection guidelines for low thermal conductivity thermal barrier coatings, Surf. Coat. Technol. 163 (2003) 67-74.

[128] M. Osaka, H. Serizawa, M. Kato, K. Nakajima, Y. Tachi, R. Kitamura, S. Miwa, T. Iwai, K. Tanaka, M. Inoue, Research and development of minor actinide-containing fuel and target in a future integrated closed cycle system, J. Nucl. Sci. Technol. 44 (2007) 309-316.

[129] R. Shukla, A. Arya, A.K. Tyagi, Interconversion of Perovskite and Fluorite Structures in Ce−Sc−O System, Inorg. Chem. 49 (2009) 1152-1157.

[130] V. Grover, A.K. Tyagi, Sub-solidus phase equilibria in the CeO_2–ThO_2–ZrO_2 system, J. Nucl. Mater. 305 (2002) 83-89.

[131] F. Zhang, C.H. Chen, J.C. Hanson, R.D. Robinson, I.P. Herman, S.W. Chan, Phases in ceria–zirconia binary oxide $(1-x)CeO_2$–$xZrO_2$ nanoparticles: the effect of particle size, J. Am. Ceram. Soc. 89 (2006) 1028-1036.

[132] G. Stapper, M. Bernasconi, N. Nicoloso, M. Parrinello, Ab initio study of structural and electronic properties of yttria-stabilized cubic zirconia, Phys. Rev. B 59 (1999) 797.

[133] E. Paparazzo, G. Ingo, N. Zacchetti, X-ray induced reduction effects at CeO_2 surfaces: An x-ray photoelectron spectroscopy study, J. Vac. Sci. Technol. A 9 (1991) 1416-1420.

[134] N. Sakai, T. Hashimoto, T. Katsube, K. Yamaji, H. Negishi, T. Horita, H. Yokokawa, Y.P. Xiong, M. Nakagawa, Y. Takahashi, Miscibility gap in CeO_2–ZrO_2–$YO_{1.5}$ system as an electrode of solid oxide fuel cell, Solid State Ion. 143 (2001) 151-160.

[135] J.-P. Eufinger, M. Daniels, K. Schmale, S. Berendts, G. Ulbrich, M. Lerch, H.-D. Wiemhöfer, J. Janek, The model case of an oxygen storage catalyst–non-stoichiometry, point defects and electrical conductivity of single crystalline CeO_2–ZrO_2–Y_2O_3 solid solutions, Phys. Chem. Chem. Phys. 16 (2014) 25583-25600.

[136] A. Nakajima, A. Yoshihara, M. Ishigame, Defect-induced Raman spectra in doped CeO_2, Phys. Rev. B, 50 (1994) 13297.

[137] J. McBride, K. Hass, B. Poindexter, W. Weber, Raman and x-ray studies of $Ce_{1-x}RE_xO_{2-y}$, where RE = La, Pr, Nd, Eu, Gd, and Tb, J. Appl. Phys. 76 (1994) 2435-2441.

[138] W. Mista, T. Rayment, J. Hanuza, L. Macalik, Synthesis and characterization of metastable CeO_2-ZrO_2 solid solution obtained by polymerized complex method, Materials Science-Poland 22 (2004) 153-170.

[139] M. Sahu, K. Krishnan, B. Nagar, M. Saxena, S. Dash, Heat capacity and thermal expansion coefficient of $SrCeO_3$ (s) and Sr_2CeO_4 (s), Thermochim. Acta 525 (2011) 167-176.

[140] B. Fultz, Vibrational thermodynamics of materials, Prog. Mater. Sci. 55 (2010) 247-352.

[141] A. Benisek, E. Dachs, On the nature of the excess heat capacity of mixing, Phys. Chem. Miner. 38 (2011) 185-191.

[142] O. Vălu, O. Beneš, R. Konings, J.-C. Griveau, E. Colineau, The low-temperature heat capacity of the (Th,Pu)O_2 solid solution, J. Phys. Chem. Solids 86 (2015) 194-206.

[143] T. Yamashita, S. Yamazaki, T. Sato, T. Matsui, Phase study and thermal expansion of yttria stabilized zirconia doped with PuO_{2-x}, J. Nucl. Sci. Technol. 39 (2002) 656-659.

[144] A. Boultif, D. Louër, Powder pattern indexing with the dichotomy method, J. Appl. Crystallogr. 37 (2004) 724-731.

[145] T. Albiol, H. Serizawa, Y. Arai, Studies in the PuO_2–ZrO_2 Pseudo-binary Phase Diagram, J. Nucl. Sci. Technol. 39 (2002) 834-837.

[146] D. Carroll, The System PuO_2–ZrO_2, J. Am. Ceram. Soc. 46 (1963) 194-195.

[147] P. Mardon, D. Hodkin, J. Dalton, Some observations on the Pu–Zr–O system, J. Nucl. Mater. 32 (1969) 126-134.

[148] J. Drummond, R. Grant, Potentiometric determination of plutonium by argentic oxidation, ferrous reduction and dichromate titration, Talanta 13 (1966) 477-488.

[149] R. Perriot, P.P. Dholabhai, B.P. Uberuaga, The role of surfaces, chemical interfaces, and disorder on plutonium incorporation in pyrochlores, Phys. Chem. Chem. Phys. 18 (2016) 22852-22863.

[150] N. Kulkarni, S. Sampath, V. Venugopal, Preparation and characterisation of Pu-pyrochlore:$[La_{1-x}Pu_x]_2Zr_2O_7$ (x = 0–1), J. Nucl. Mater. 281 (2000) 248-250.

[151] S. Vaudez, J. Bonnerot, E. Abonneau, P. Matheron, L. Donnet, F. Desmouliere, Fabrication of a composite material:$(Ce_{1-x}Pu_x)_2Zr_2O_7$ pyrochlore inclusions in a porous magnesia matrix, Commissariat a l'Energie Atomique, 2004.

[152] T. Kutty, K. Khan, P. Hegde, A. Sengupta, S. Majumdar, D. Purushotham, Densification behaviour and sintering kinetics of PuO_2 pellets, J. Nucl. Mater. 297 (2001) 120-128.

[153] M. Kato, T. Uchida, T. Matsumoto, T. Sunaoshi, H. Nakamura, M. Machida, Thermal expansion measurement and heat capacity evaluation of hypo-stoichiometric $PuO_{2.00}$, J. Nucl. Mater. 451 (2014) 78-81.

[154] M. Tokar, A. Nutt, T. Keenan, Linear Thermal Expansion of Plutonium Dioxide, Nucl. Technol. 17 (1973) 147-152.

[155] B. Schuster, F. Fujara, B. Merk, R. Neumann, T. Seidl, C. Trautmann, Response behavior of ZrO_2 under swift heavy ion irradiation with and without external pressure, Nucl. Instrum. Methods Phys. Res. B 277 (2012) 45-52.

[156] M. Patel, V. Vijayakumar, S. Kailas, D. Avasthi, J. Pivin, A.K. Tyagi, Structural modifications in pyrochlores caused by ions in the electronic stopping regime, J. Nucl. Mater. 380 (2008) 93-98.

[157] C. Trautmann, M. Toulemonde, K. Schwartz, J. Costantini, A. Müller, Damage structure in the ionic crystal LiF irradiated with swift heavy ions, Nucl. Instrum. Methods Phys. Res. B 164 (2000) 365-376.

[158] C.L. Tracy, J.M. Pray, M. Lang, D. Popov, C. Park, C. Trautmann, R.C. Ewing, Defect accumulation in ThO_2 irradiated with swift heavy ions, Nucl. Instrum. Methods Phys. Res. B 326 (2014) 169-173.

[159] M. Lang, F. Zhang, W. Li, D. Severin, M. Bender, S. Klaumünzer, C. Trautmann, R.C. Ewing, Swift heavy ion-induced amorphization of $CaZrO_3$ perovskite, Nucl. Instrum. Methods Phys. Res. B 286 (2012) 271-276.

[160] S. Lutique, R. Konings, V. Rondinella, J. Somers, T. Wiss, The thermal conductivity of $Nd_2Zr_2O_7$ pyrochlore and the thermal behaviour of pyrochlore-based inert matrix fuel, J. Alloys Compd. 352 (2003) 1-5.

[161] K. Rao, J. Wong, M. Weber, Bonding and structure of Nd^{3+} in BeF_2 glass by XANES and EXAFS spectroscopy, J. Chem. Phys. 78 (1983) 6228-6237.

[162] V. Rai, P. Rajput, S. Jha, D. Bhattacharyya, X-ray absorption studies of gamma irradiated Nd doped phosphate glass, AIP Conf. Proc. 1665 (2015) 070015.

[163] J.F. Ziegler, J. Biersack, U. Littmark, The stopping and range of ions in matter, Vol. 1, 1, Pergamon Press, New York (1985).

[164] P. Kulriya, F. Singh, A. Tripathi, R. Ahuja, A. Kothari, R. Dutt, Y. Mishra, A. Kumar, D. Avasthi, Setup for in situ x-ray diffraction study of swift heavy ion irradiated materials, Rev. Sci. Instrum. 78 (2007) 113901.

[165] K.E. Sickafus, H. Matzke, K. Yasuda, P. Chodak III, R.A. Verrall, P.G. Lucuta, H.R. Andrews, A. Turos, R. Fromknecht, N.P. Baker, Radiation damage effects in cubic-stabilized zirconia irradiated with 72 MeV I^+ ions, Nucl. Instrum. Methods Phys. Res. B 141 (1998) 358-365.

[166] G. Sattonnay, L. Thomé, I. Monnet, C. Grygiel, C. Legros, Effects of electronic energy loss on the behavior of $Nd_2Zr_2O_7$ pyrochlore irradiated with swift heavy ions, Nucl. Instrum. Methods Phys. Res. B 286 (2012) 254-257.

[167] G. Williamson, W. Hall, X-ray line broadening from filed aluminium and wolfram, Acta Metall. 1 (1953) 22-31.

[168] M. Kumar, R.K. Pandey, P. Rajput, S. Khan, F. Singh, D. Avasthi, A.C. Pandey, Swift heavy ions induced nano-grain fragmentation in fluoride thin films, J. Alloys. Compd. 695 (2017) 83-90.

[169] H. Thomas, S. Thomas, R.V. Ramanujan, D. Avasthi, I. Al-Omari, S. Al-Harthi, M. Anantharaman, Swift heavy ion induced surface and microstructural evolution in metallic glass thin films, Nucl. Instr. Meth. Phys. Res. B 287 (2012) 85-90.

[170] S. Som, S. Dutta, V. Kumar, V. Kumar, H. Swart, S. Sharma, Swift heavy ion irradiation induced modification in structural, optical and luminescence properties of Y_2O_3: Tb^{3+} nanophosphor, J. Lumin. 146 (2014) 162-173.

[171] W. Weber, N. Hess, Ion beam modification of $Gd_2Ti_2O_7$, Nucl. Instrum. Methods Phys. Res. B 80 (1993) 1245-1248.

[172] P. Mallick, D. Agarwal, C. Rath, D. Behera, D. Avasthi, D. Kanjilal, N. Mishra, Evolution of microstructure and crack pattern in NiO thin films under 200MeV Au ion irradiation, Radiat. Phys. Chem. 81 (2012) 647-651.

[173] B. Dash, P. Mallick, P. Dash, R. Biswal, J. Prakash, A. Tripathi, D. Kanjilal, N. Mishra, Swift heavy ion irradiation induced modification of structure and surface morphology of $BiFeO_3$ thin film, Bull. Mater. Sci. 36 (2013) 813-818.

[174] L. Singh, K.S. Samra, Structural characterization of swift heavy ion irradiated polycarbonate, Nucl. Instr. Meth. Phys. Res. B 263 (2007) 458-462.

[175] K. Trachenko, M. Pruneda, E. Artacho, M.T. Dove, Radiation damage effects in the perovskite $CaTiO_3$ and resistance of materials to amorphization, Phys. Rev. B 70 (2004) 134112.

[176] C.L. Tracy, M. Lang, J.M. Pray, F. Zhang, D. Popov, C. Park, C. Trautmann, M. Bender, D. Severin, V.A. Skuratov, Redox response of actinide materials to highly ionizing radiation, Nat. Commun. 6 (2015) 6133.